Remote Sensing of Hydrocarbon-induced Rock Alterations at Cement Field, Oklahoma

---

A Thesis

Presented to

the Faculty of the Department of Earth and Atmospheric Sciences

University of Houston

In Partial Fulfillment

of the Requirements for the Degree

Master of Science

By

Lei Sun

August 2014

Remote Sensing of Hydrocarbon-Induced Rock Alterations at Cement Field, Oklahoma

---

Lei Sun

APPROVED:

Dr. Shuhab Khan

(Committee Chair)

Department of Earth and Atmospheric Sciences

University of Houston

Dr. Jonathan Snow

Department of Earth and Atmospheric Sciences

University of Houston

Dr. Ana Petrovic

Noble Energy

Dr. Dan Wells, Dean

College of Natural Sciences and Mathematics

University of Houston

ACKNOWLEDGEMENTS

My special thanks go to Dr. Shuhab D. Khan, Ph.D., for his guidance and support throughout this endeavor. I would like to thank Dr. Alexander Robinson and Dr. Jonathan Snow, for their help in petrographic photographing. I would also like to acknowledge Diana Krupnik, for her help in field work. Casey Synder, Unal Okyay, and Kivanc Biber offered valuable advices in data processing, and Laeiq Ahmed, and Ismail Ahmad helped me in lab spectroscopy; I would express my great appreciation to them.

Remote Sensing of Hydrocarbon-induced Rock Alterations at Cement Field, Oklahoma

---

A Thesis

Presented to

the Faculty of the Department of Earth and Atmospheric Sciences

University of Houston

In Partial Fulfillment

of the Requirements for the Degree

Master of Science

By

Lei Sun

August 2014

ABSTRACT:

This study uses satellite- and ground-based remote sensing techniques to detect hydrocarbon-induced rock alterations at the Cement oil field, Oklahoma. Hydrocarbon seepage is the escape of oil and gas from petroleum reservoirs and their upward-migration to the surface. These hydrocarbons at the surface can generate rock alterations, including mineralogical changes, bleaching of red beds, and clay mineral alterations. Surficial expressions of such alterations are distinct from adjacent rocks, and could be detected by remote sensing techniques.

The Cement field is a giant oil and gas field located in the southeastern Anadarko basin in Oklahoma. The surface structure is a northwest-trending, elongate and asymmetrical anticline. This field has been reported to have heavily altered surficial rocks. Loss of iron and impregnation of sandstone by carbonate cements, and replacement of gypsum by calcite, are the major alteration phenomena in this field.

Remote sensing data hold great potential to characterize rocks with great precision and fine detail. This study identified outcrops with surficial rock alterations from Landsat 8 and ASTER multispectral data, as well as Hyperion and Specim hyperspectral imagery. Published geologic maps and geochemical data were combined to show the geologic extent and various degrees of rock alterations. Petrographic analysis showed bleaching and cementation of sandstones, as well as crystallization gradient of gypsum samples. Laboratory spectroscopy was used to assist with image classification. Principal component analysis, minimum noise fraction, spectral angle

mapper, and band ratios are used in image processing. Remote sensing data detected bleaching and carbonate cementation. Combining lithological, remote sensing and geochemical data, this study built a model for petroleum seepage and related rock alterations, and provides a workflow for employing remote sensing techniques in resource exploration.

Table of Contents

List of Figures

List of Tables

1. Introduction

Modern hydrocarbon exploration requires the combination of geophysics, geology, and geochemistry, but the oldest way to find oil and gas relies on the usage of near-surface seepage (Jones and Drozd, 1983). Seepage is the escape of oil and gas from petroleum reservoirs and their upward-migration to the surface. As no petroleum seal rock is completely impermeable, every reservoir leaks in various degrees and amounts (Philp and Crisp, 1982). Macroseepages display oil and gas outflow, whereas microseepages are too subtle to directly observe but identifiable by geochemical means (Price, 1986). Hydrocarbon microseepages have been reported in many locations in the United States (Fig. 1-1); they are typically located above oil and gas fields.

Hydrocarbons have lower density than water and soil/rock, thus they have a potential to migrate upward. Saunders et al. (1999) proposed that buoyant hydrocarbon micro-bubbles can rise through the water-filled network of fractures, joints, and bedding planes, providing a logical mechanism for vertical migration of light hydrocarbons.

Schumacher (1996) summarized that hydrocarbons present at surface can generate various kinds of alterations of soil/rock: 1) microbiological anomalies; 2) mineralogical changes; 3) bleaching of red beds; 4) clay mineral alterations; 5) electrochemical changes; 6) radiation anomalies; and 7) biogeochemical and geobotanical anomalies. Surficial expressions of such alterations are distinct from adjacent soil/rock, thus they could be used to detect hydrocarbon microseepages.

Various methods including field lithological mapping, geochemistry, field spectroscopy, and carbon dioxide and methane monitoring, have been utilized to detect oil and gas seepages (Donovan, 1974; Yang et al., 1998; Etiope and Klusman, 2010; Klusman, 2011). Recently, the

applications of remote sensing techniques in detecting microseepages have gained more and more attention.

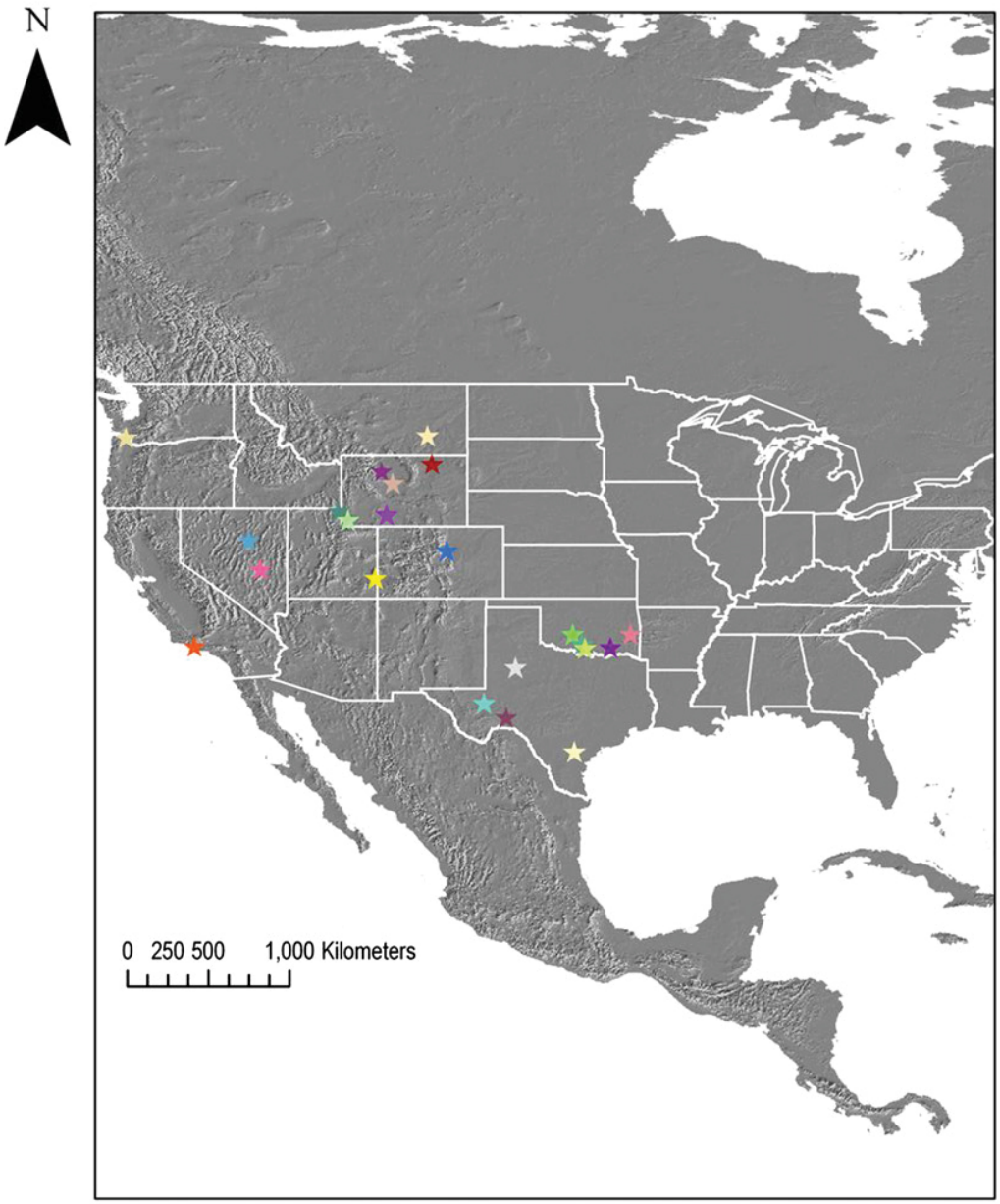

Figure 1-1, Locations of surficial rock and soil alterations related to petroleum reservoirs reported in the United States, legend on the next page, from Petrovic et al. (2008).

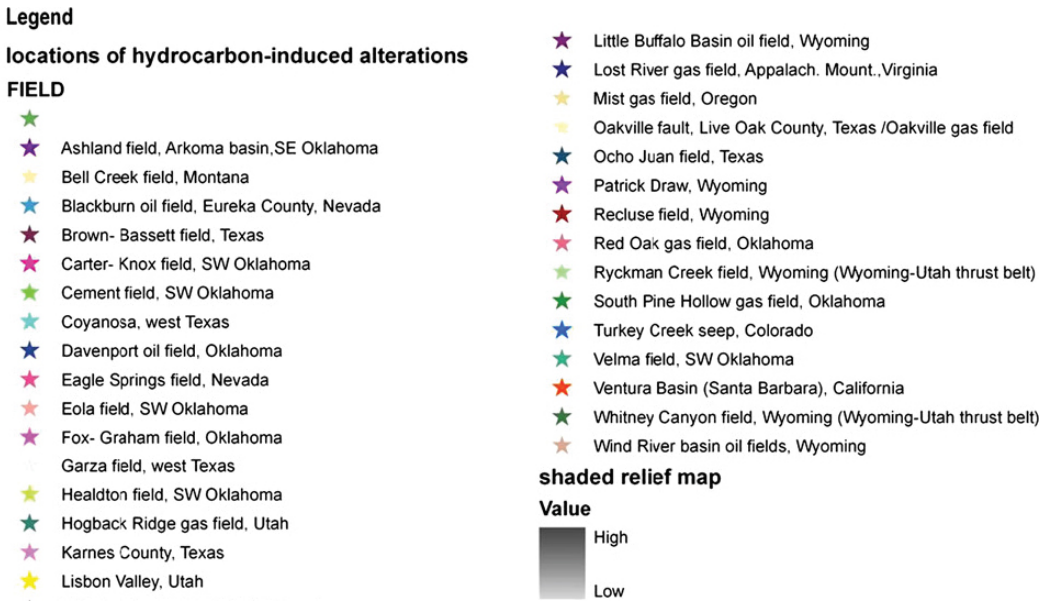

Remote sensing involves the measurement of radiation reflected and emitted from the earth's surface by a sensor at a distance from the object. Remote sensing spectra contain plenty of geologic information like topography and material chemistry. Various remote sensing techniques, including Landsat Multispectral Scanning System (MSS), the Landsat Thematic Mapper (TM), SPOT satellite, Advanced Spaceborne Thermal Emission and Reflection (ASTER) system, HyMap Imagery, Probe-1, and Hyperion, have been reported to image regional and local geologic features (Abrams et al., 1977; Berger et al., 1992; Van der Meer et al., 2002; Crósta et al., 2003; Khan and Jacobson, 2008; Petrovic et al., 2012).

In this study, Landsat 8 and ASTER multispectral remote sensing imagery, as well as Hyperion and Specim hyperspectral remote sensing imagery, are used to detect and map surficial alterations in Cement field, Oklahoma. The areal extents of the satellite datasets are shown in Fig. 1-2. The purpose of this thesis is to test the possibility of using remote sensing techniques to detect surficial rock alterations, and build a geologic model relating rock alterations with underlying

hydrocarbon reservoirs. This work proposes a prospective tool for further petroleum investigation and exploration, especially in areas where field work is difficult.

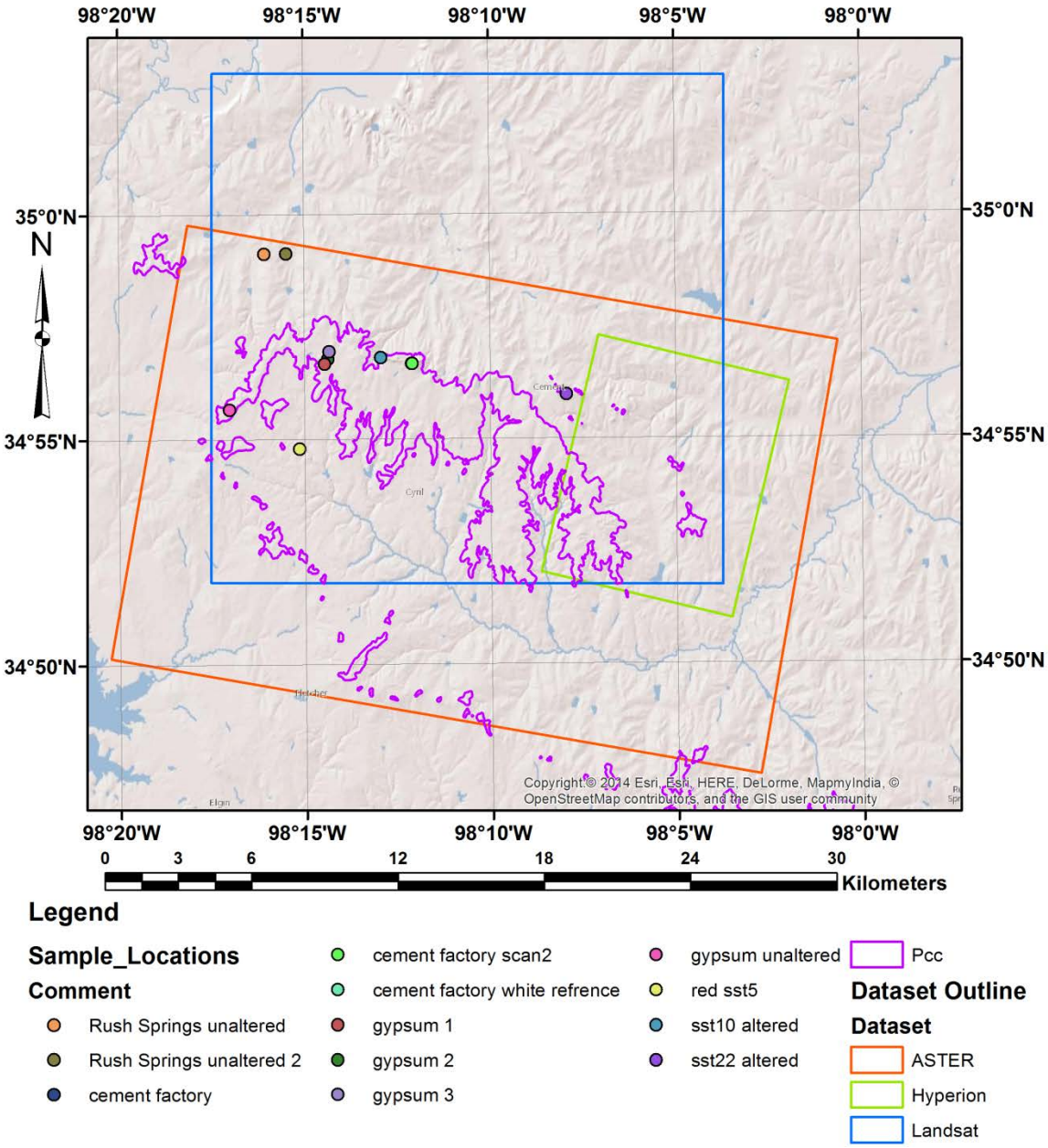

Figure 1-2, The areal extents of the satellite datasets. The dots show the sample locations. The magenta outlines show the areal extent of the Cloud Chief Formation, and the rest of the map outcrops the Rush Springs Formation.

2. Geologic Setting

The Cement field is a giant oil and gas field located in the southeastern Anakarko basin in Caddo and Grady Counties, Oklahoma (Fig. 2-1). It consists of two closely related fields, East Cement, and West Cement. The surface structure is a northwest-trending, doubly plunging, elongate, slightly asymmetric anticline (Donovan, 1974). The accumulations are generally restricted to the structural highs (Fig. 2-2).

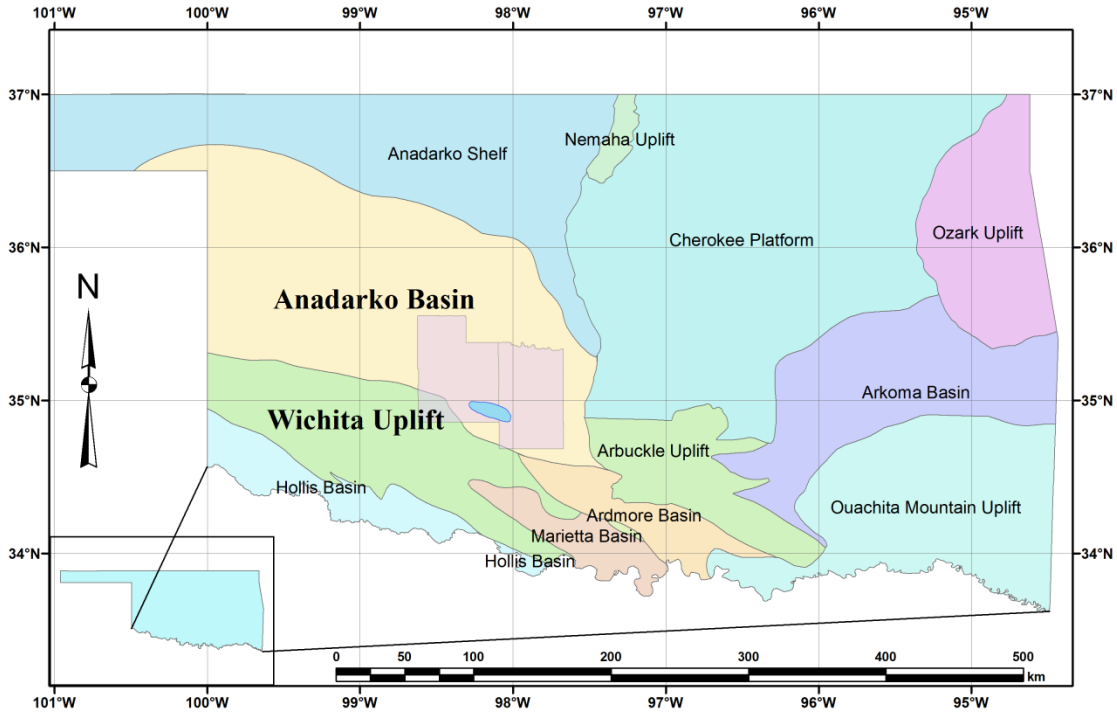

Figure 2-1, Location and regional background of the Cement field, Oklahoma, generalized from (Northcutt and Campbell, 1995).

A stratigraphic column of Cement field is shown in Fig. 2-3. Hoxbar Group rocks in Missourian Series are the most prolific reservoirs of Pennsylvanian age. Rocks exposed are composed of Whitehorse Group and Cloud Chief Formation of Guadalupian Series (Donovan, 1974). The Rush Springs, a predominantly reddish-brown, fine-grained clayey quartz sandstone,

is the uppermost formation of the Whitehorse, which is unconformably overlain by the Cloud Chief Formation, a basal gypsum member. Previous work showed that the south-dipping reverse fault parallel with the anticline, and a major normal fault follows the crest (Herrmann, 1961).

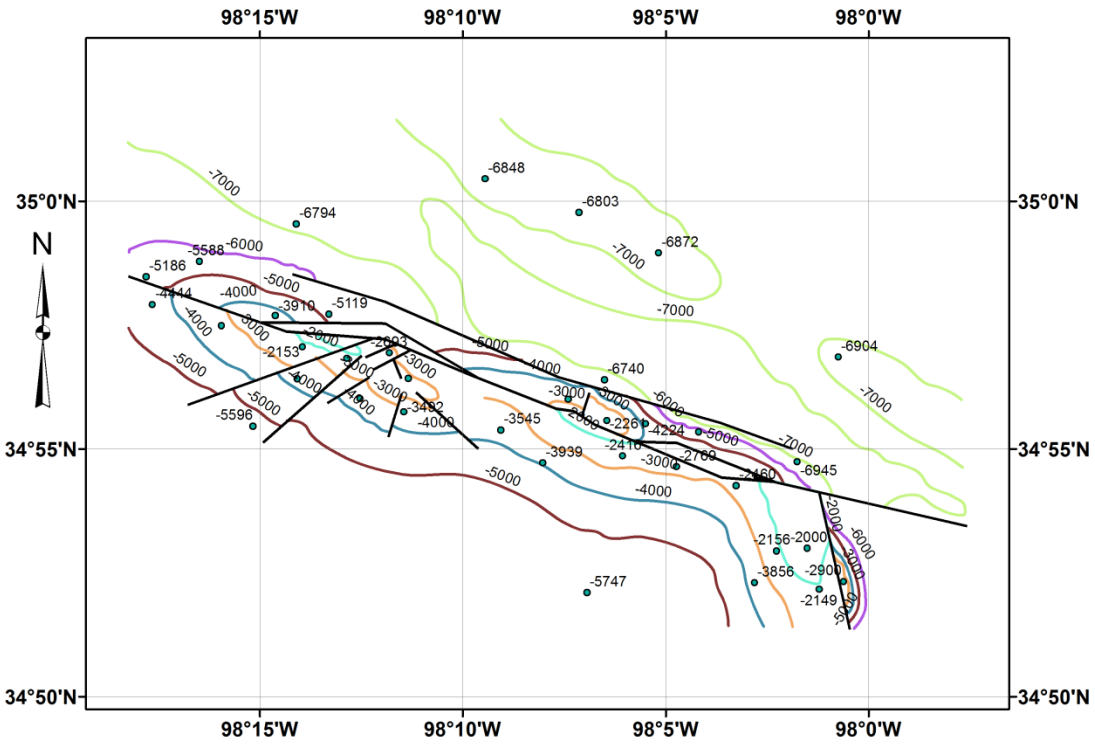

Figure 2-2, Structural contour map of the Hoxbar Group, Cement field, Oklahoma, redrawn after (Herrmann, 1961). The depths of well control points as well as contours of Hoxbar Group are labeled. Black lines show faults.

Hydrocarbon-induced alterations in the Cement field, Oklahoma were first reported by Reeves (1921). Donovan (1974) performed a comprehensive investigation including surface lithological mapping and isotopic work. He found striking mineralogical and chemical changes, and confirmed the presence of hydrocarbon microseepage at this site.

The red-brown sandstone of the Rush Springs Formation is heavily bleached along the anticlinal structure of the Cement field. The red-brown color changes progressively towards the

crest of the East and West Cement anticlines to pink, yellow, white and light gray (Reeves, 1921; Donovan, 1974). The Cyril Gypsum member grades from pure gypsum at flank locations to gypsum with admixed carbonate near the crest, and calcite with smaller amounts of dolomite on top of the structure (Donovan, 1974).

Donovan et al. (1979b) tried to use Landsat remote sensing tools to detect these surficial alterations, but concluded that the Landsat I and II images had a limited ability to detect microseepage, largely because of the mask by unaltered overlying rock, soil, and dense vegetation, and suggested further experiments with higher resolution.

Donovan et al. (1979a) reported that airborne magnetic survey detected high-wave-number magnetic anomaly in Cement field. They interpreted that as reflecting abundant near-surface diagenetic magnetite, and proposed further utility of this direct geophysical technique in oil exploration. A lot of research had been done to test the presence of diagenetic magnetite, however, the magnetic anomaly previously reported are mainly the result of the drilling contamination (Reynolds et al., 1990; Gay, 1992). Meanwhile, Reynolds et al. (1991) noted the presence of pyrite, marcasite and pyrrhotite, and suggested that the ferrimagnet is a possible natural source of magnetic anomaly. Gay (1992) concluded that magnetic anomalies in sedimentary rocks cannot be used as an exploration tool to find oil.

This work uses modern remote sensing techniques to detect rock alterations induced by hydrocarbons. A vertical outcrop in a mining quarry was scanned with ground-based remote sensing cameras. Several rock samples were collected and scanned from planned location within and outside the alteration zone. Combining lithological, remote sensing, and geochemical data, this study tries to build a model for petroleum seepage and related rock alterations, and provide a workflow for resource exploration.

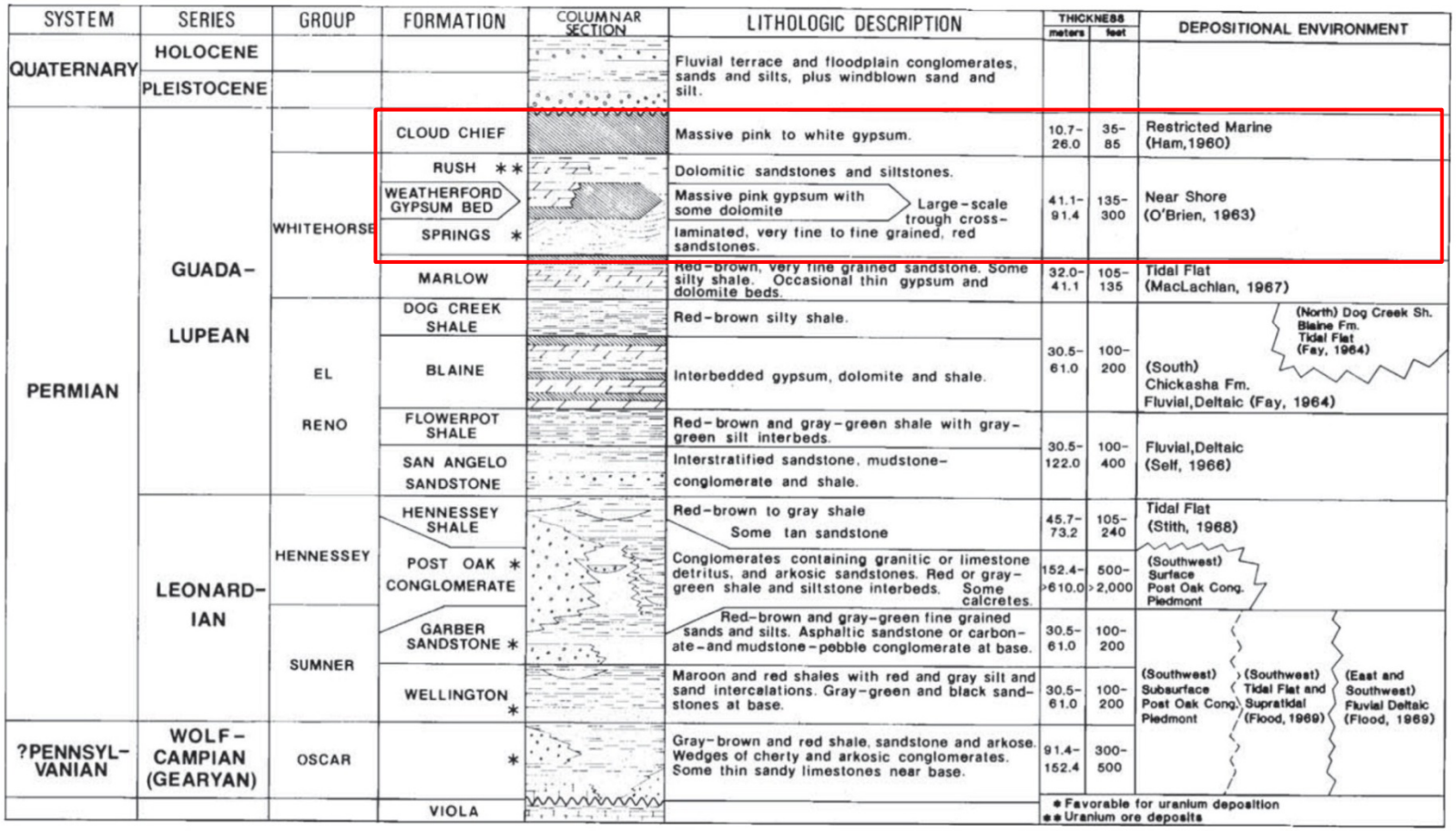

Figure 2-3, Stratigraphic column of Cement field, from (Allen and Thomas, 1984), Rush Springs and Cloud Chief, the major formations in this study, are marked by the red box.

3. Petrography

3.1 Introduction

Petrography is the study of composition, texture and small-scale structure of rocks (Hefferan and O'Brien, 2010). A lot of geologic information including mineralogy, grain sizes, grain shape and their relative abundances, and textures could be revealed under microscopes. This chapter presents petrographic analysis which was used to gain a better understanding of the chemistry of rock samples, thus providing a useful reference for spectroscopy and remote sensing imagery.

3.2 Methods

The rock samples were cut into small chips by rock-cutting facility, then polished and mounted onto glass slides, and finally ground to 30 micrometers thick. The thin sections are observed under a Nikon Eclipse LV100POL microscope located at the University of Houston. Photographs of 2560 * 1920 in resolution were also taken.

3.3 Results

Samples were collected from field work, the number of which was highly limited by accessibility; the locations are displayed in Fig. 3-1.

3.3.1 Sandstones

The unaltered sandstones are very fine-grained to fine-grained, reddish brown subarkose (Fig. 3-2). The rocks are soft and easy to break, indicating poor compaction and cementation. Thin sections (Fig. 3-3) show that the clastic grains are 80 – 200 micrometers in diameter, sub-angular, well sorted, mostly quartz with a small amount of K-feldspar. Some feldspar grains have been

altered into clay minerals. Besides some clastic grains being coated with hematite-limonite cement, no other cementation was observed, leaving about 15% – 20% pore space.

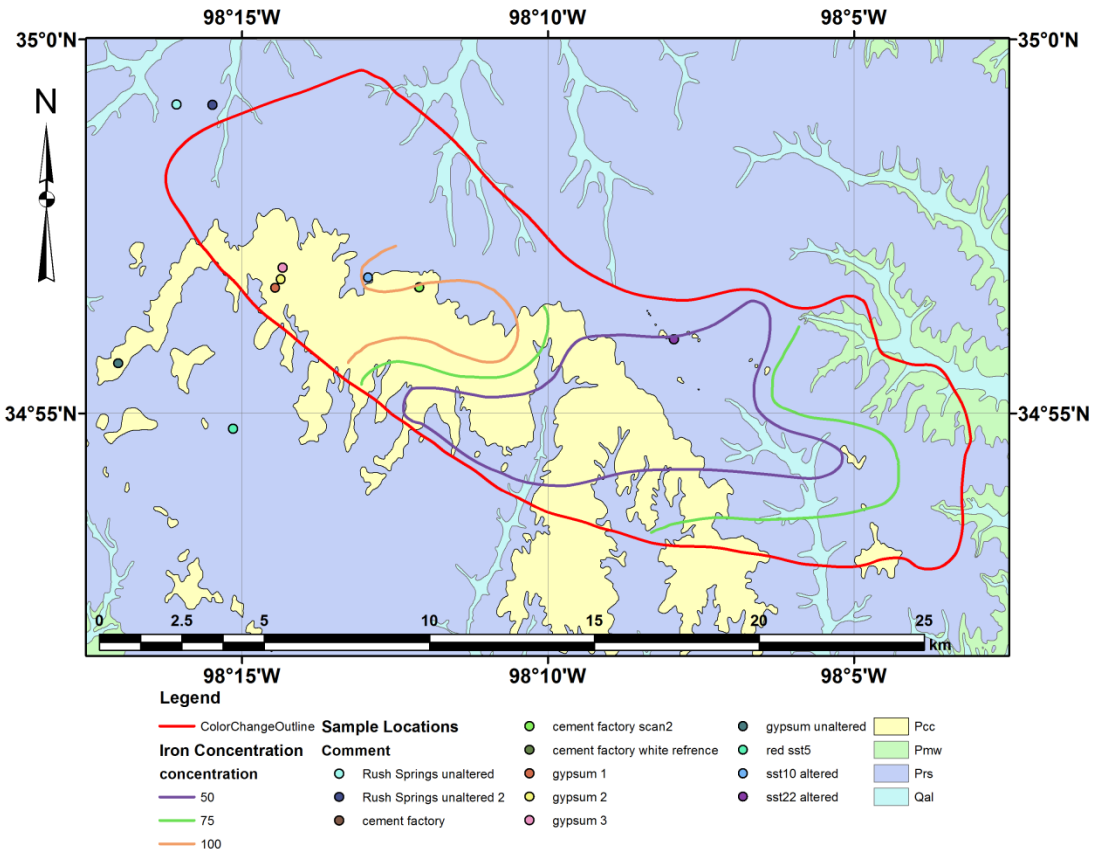

Figure 3-1, Field sample locations superimposed on the surface geologic map. The red line indicates the areal extent of rock alteration (color change); other lines indicate lower concentration of iron towards the center, with contours representing iron concentration at intervals of 25 ppm. Data from (Donovan, 1974; Stanley and Miller, 2005).

Eleven altered sandstone samples were collected from the field. These samples are compact and hard, very fine- to fine-grained, and have various colors including grey to dark grey, yellow, white, or a little bit of red (Fig. 3-4 & 3-5). Sample CF-9 has a significant color change from grey

to yellow, and the transition is almost a flat surface. Only samples CF-9 and sandstone-22 fizzed with dilute hydrochloric acid, indicating the presence of abundant calcite.

Figure 3-2, Hand samples of unaltered sandstones, A) sandstone-unaltered-1, B) sandstone-unaltered-3, C) sandstone-unaltered-4, and D) sandstone-unaltered-5. All unaltered sandstones are red in color, very fine to fine-grained, soft and easy to break because of poor compaction and cementation.

Some samples exhibited surface alterations. Numerous pyrite grains displaying pale brass yellow color, metallic luster and good crystal faces could be identified from sample CF-2 (Fig. 3-5). Pyrite is seen on exposed surfaces and is associated with rusty looking red surfaces. A similar red surface is present on an exposed surface of sample CF-4, but no pyrite is observed. Some bluish-green surface alterations are present on sample CF-3.

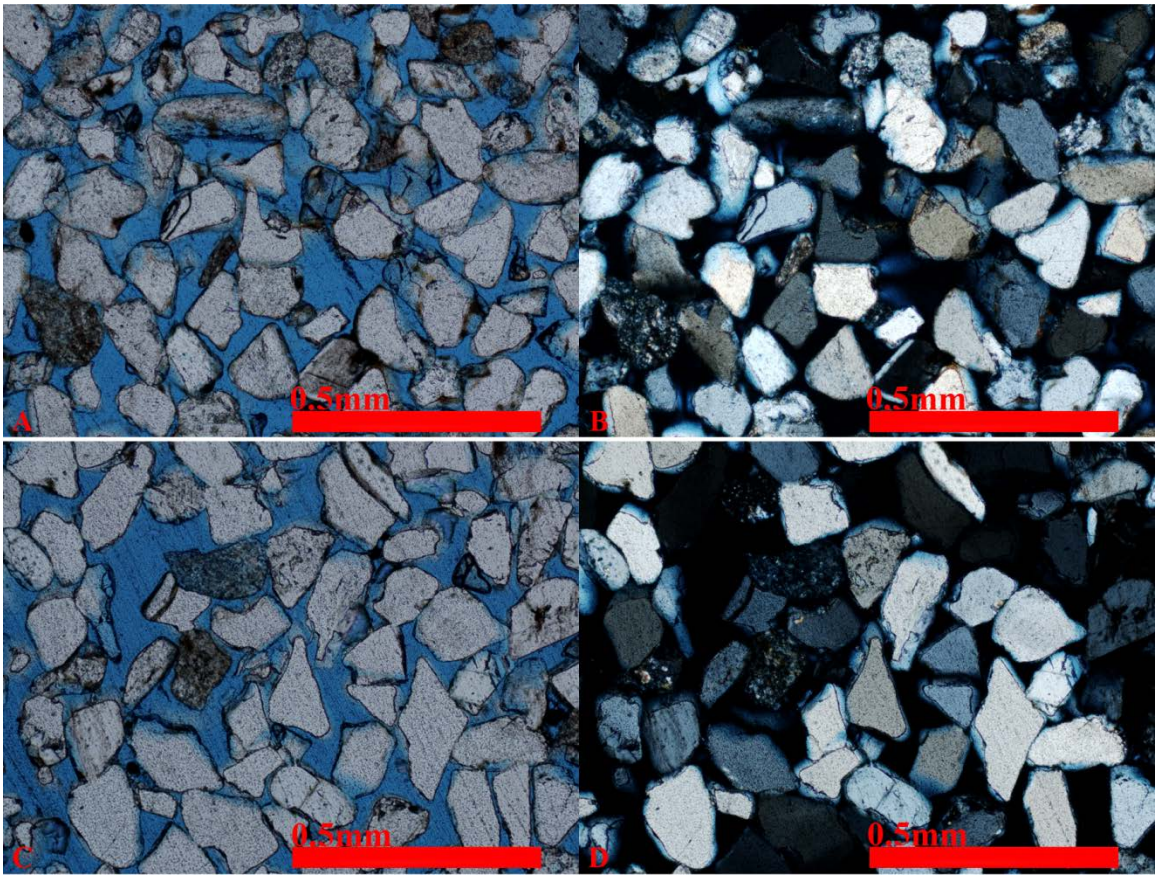

Figure 3-3, Photomicrographs of unaltered sandstone samples, A) and B) sandstone-unaltered-1, C) and D) sandstone-unaltered-4. The clastic grains are 80 – 200 micrometers in diameter, sub-angular, well sorted, mostly quartz with small amount of K-feldspar; some feldspar grains have been altered into clay minerals. Besides some clastic grains being coated with hematite-limonite cement, no other cementation was observed.

Thin sections (Fig. 3-6, 7, 8, 9) show that all altered samples have the same clastic grains as the unaltered ones: fine-grained to very fine-grained (80 – 200 micrometers in diameter), sub-angular, well-sorted, mostly quartz with some K-feldspars. Some feldspar grains have already been altered into clay minerals. However, all altered samples are well cemented by carbonates; hematite / limonite coating commonly observed in the unaltered samples are rare here. Hydrochloric acid tests show that the carbonate in samples CF-9 and sandstone-22 is calcite, and the rest is dolomite.

Differentiation of calcite versus dolomite in these thin sections is very hard due to unfavorable crystallization conditions. The color transition observed on hand sample CF-9 is unrecognizable under microscope.

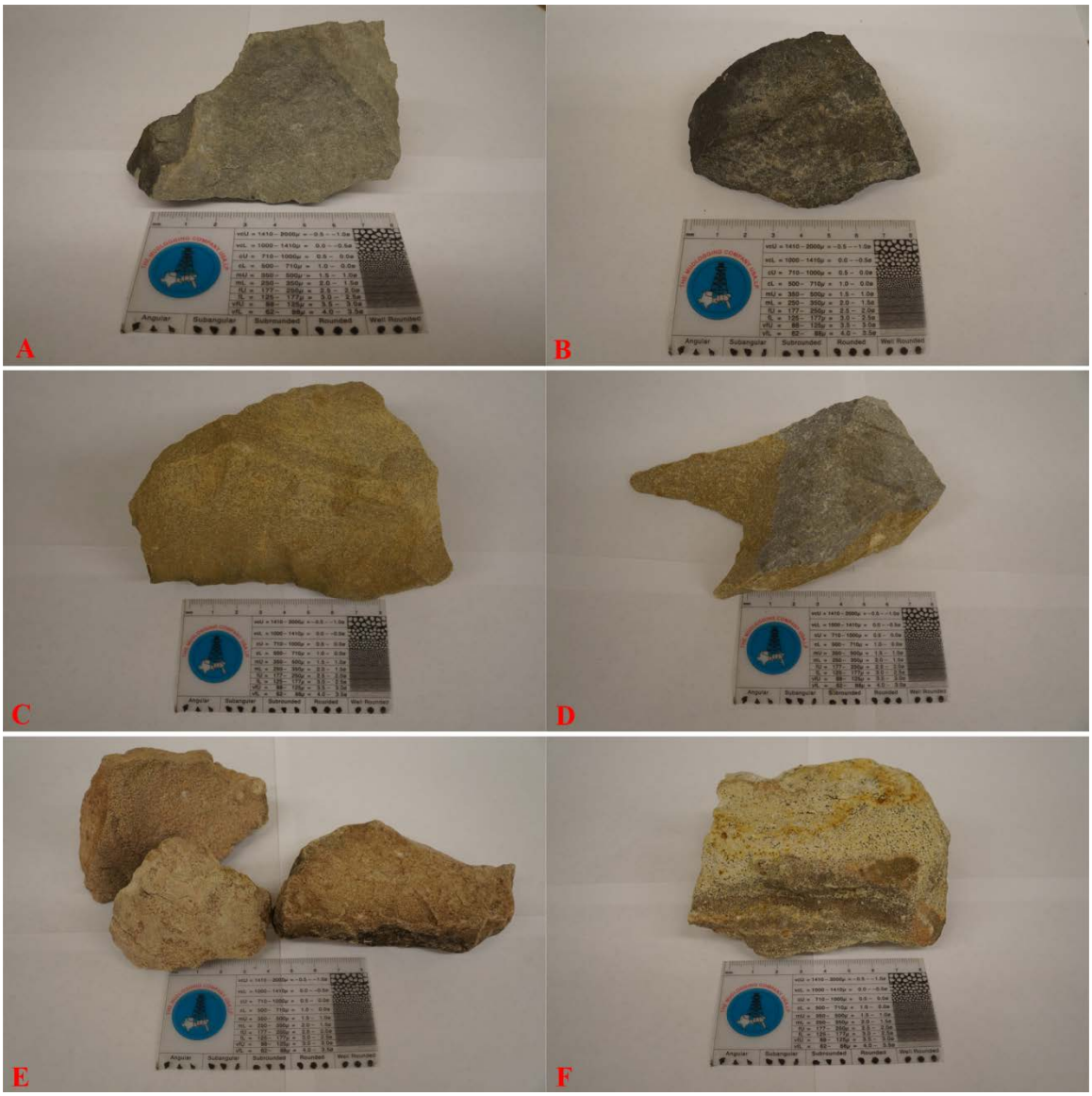

Figure 3-4, Hand samples of altered sandstones, A) CF-1, B) CF-5, C) CF-7, D) CF-9, E) sandstone-10, and F) sandstone-22. These samples are compact and hard, very fine- to fine-grained, and have various colors including grey to dark grey, yellow, white, or a little bit of red.

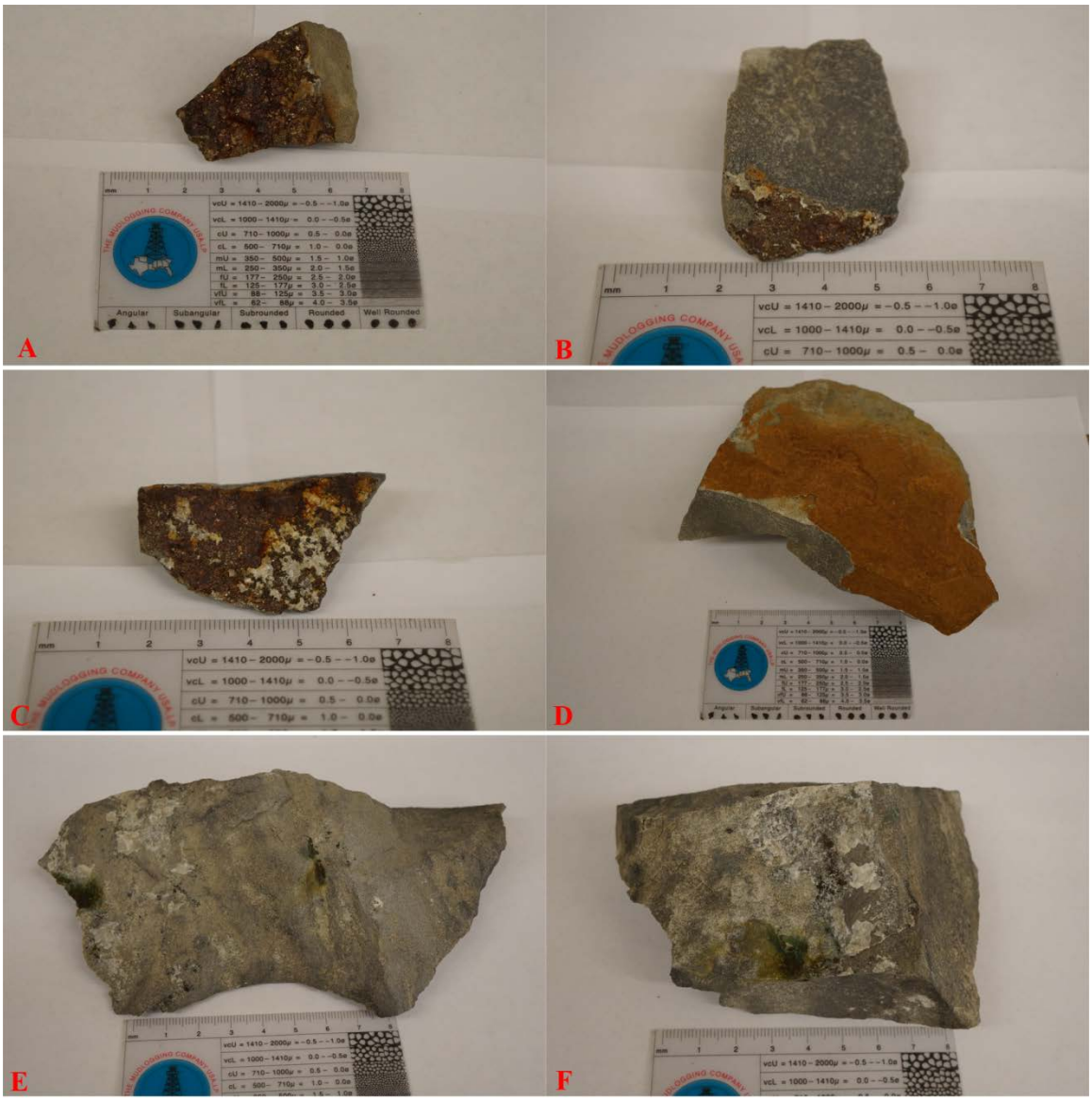

Figure 3-5, Hand samples of altered sandstones with surface alterations, A) B) and C) CF-2, D) CF-4, E) and F) CF-3. All of these samples are very fine to fine-grained. Sample CF-2 has pyrite and red rust on surface; CF-4 has similar rust but no pyrite; CF-3 has bluish-green surface alterations.

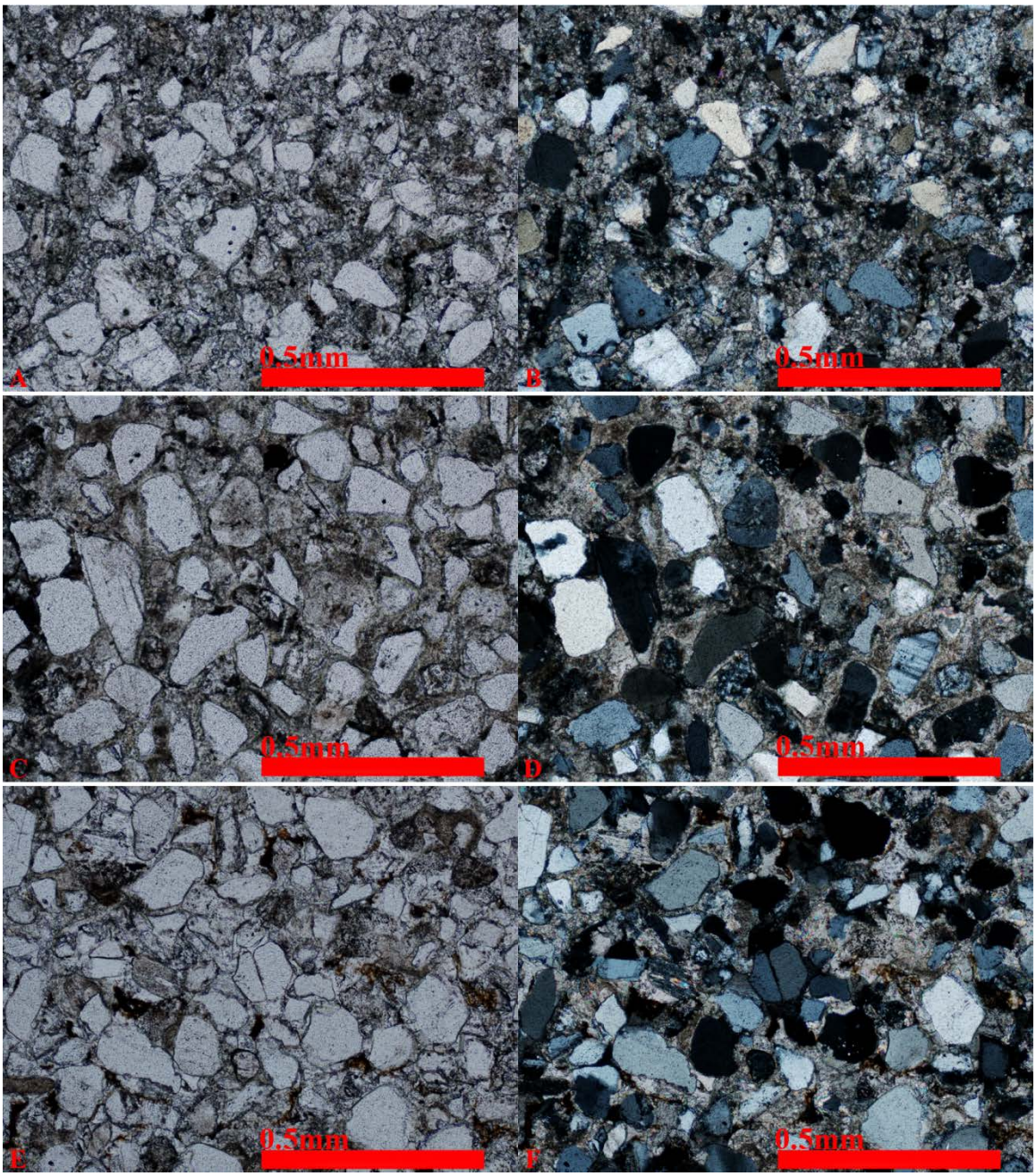

Figure 3-6, Photomicrographs of altered sandstone samples, A) and B) CF-1, C) and D) CF-2, E) and F) CF-3. These samples are well cemented by carbonates.

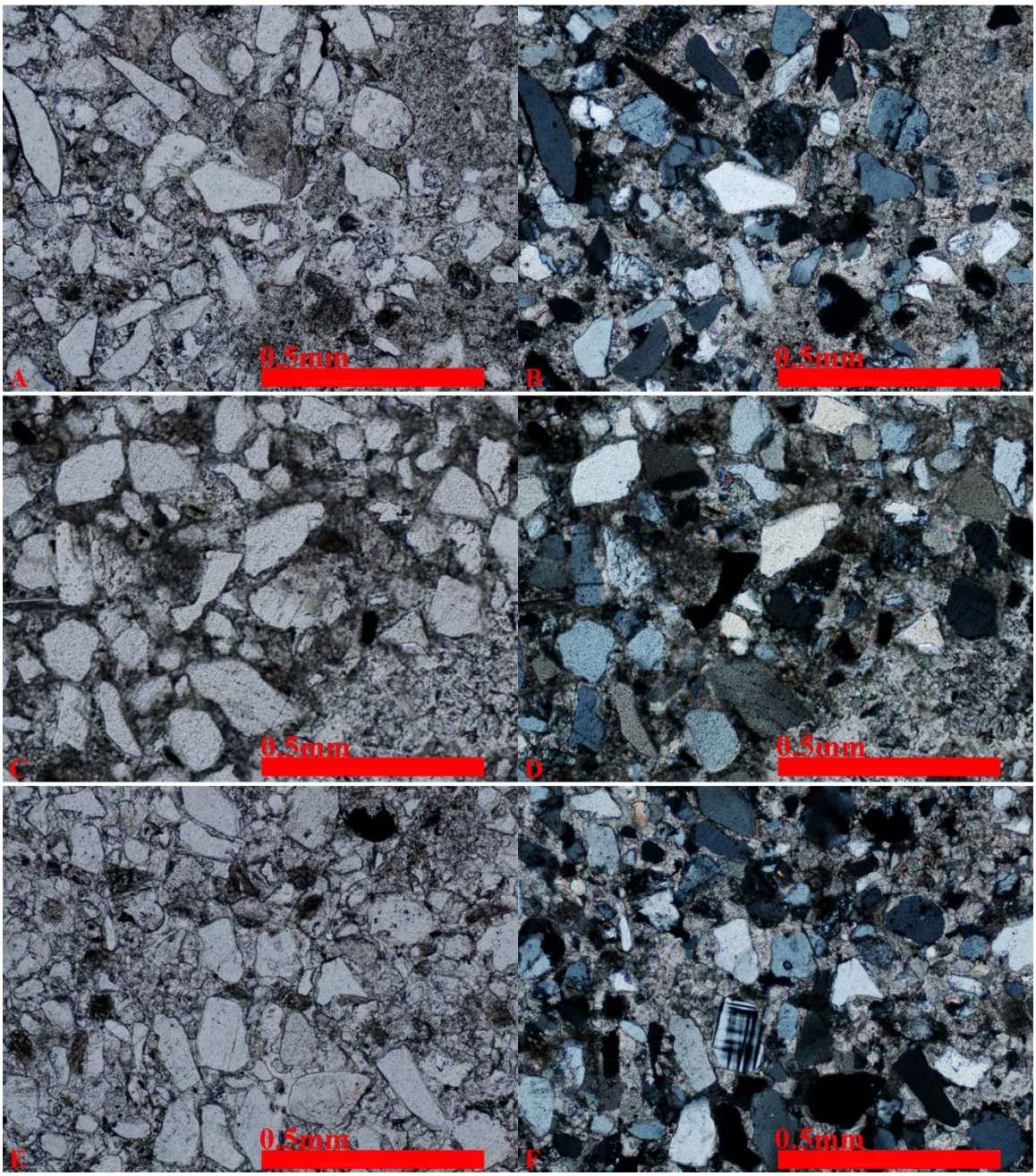

Figure 3-7, Photomicrographs of altered sandstone samples, A) and B) CF-4, C) and D) CF-5, E) and F) CF-6. These samples are well cemented by carbonates.

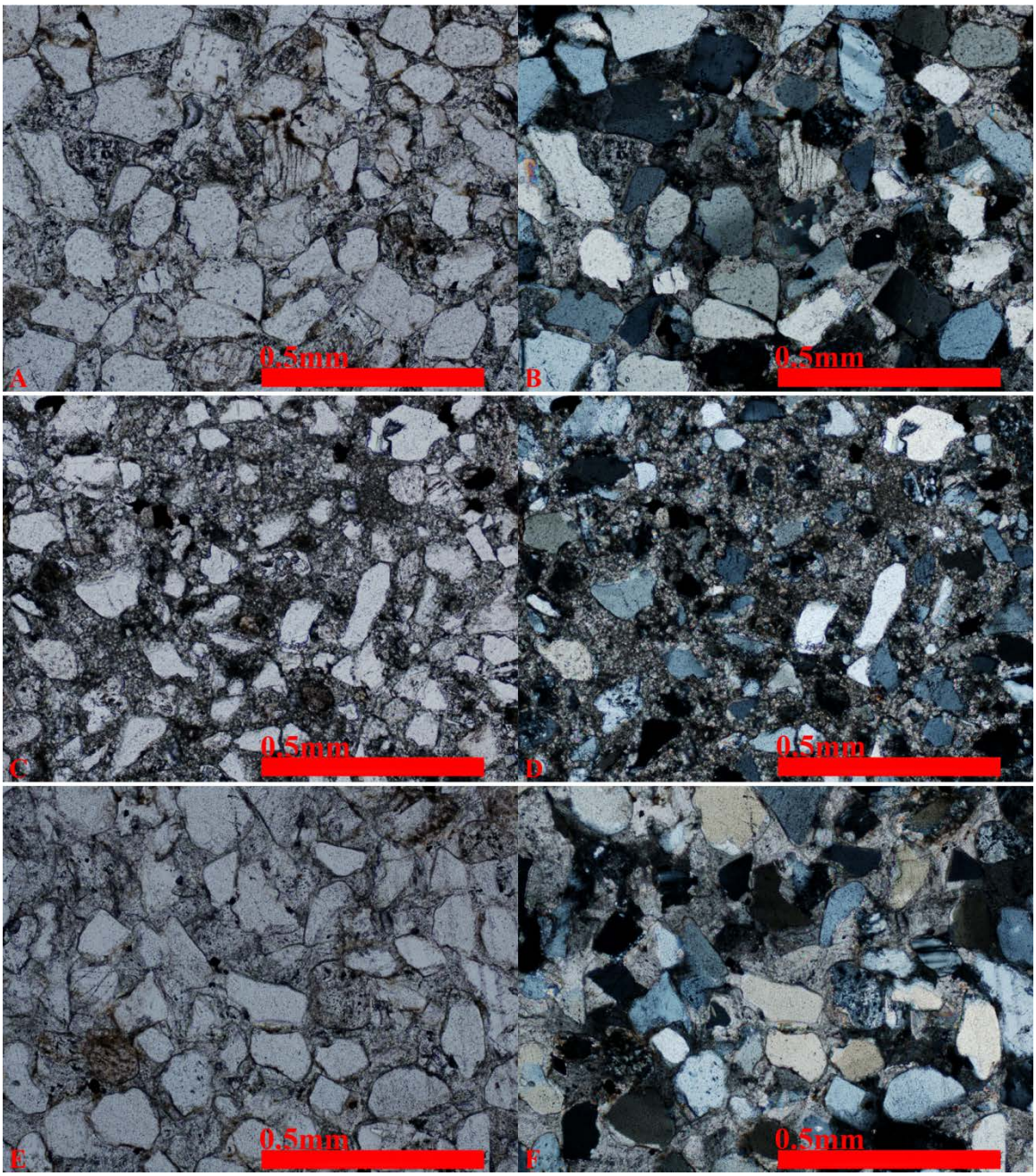

Figure 3-8, Photomicrographs of altered sandstone samples, A) and B) CF-7, C) and D) CF-8, E) and F) CF-9. These samples are well cemented by carbonates.

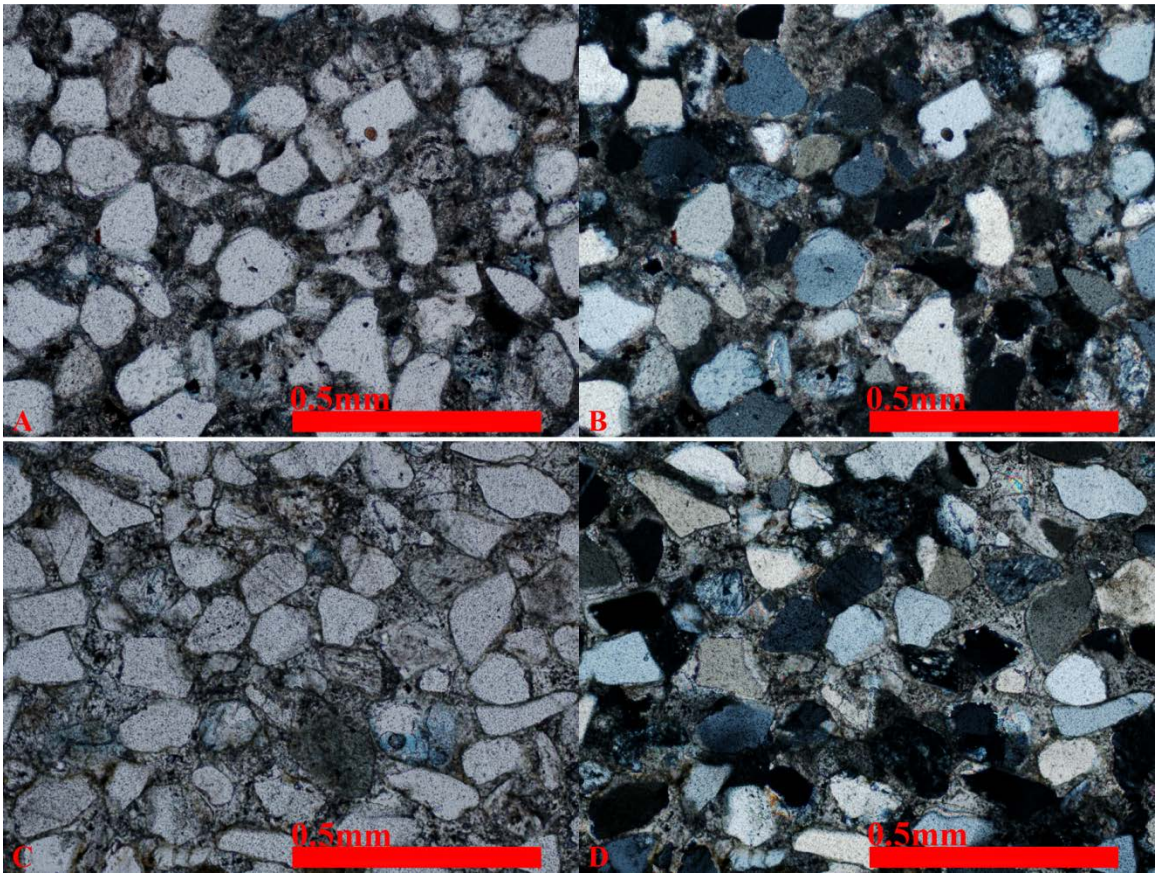

Figure 3-9, Photomicrographs of altered sandstone samples, A) and B) sandstone-10, C) and D) sample sandstone-22. These samples are well cemented by carbonates.

3.3.2 Gypsum Samples

Two unaltered gypsum samples were collected outside the alteration zone and three altered gypsum samples were collected inside the alteration site. All gypsum samples are massive; one unaltered sample is pinkish red and the others are white (Fig. 3-10). The thin sections of the unaltered ones (Fig. 3-11) show that they are composed of almost pure gypsum. They have large, elongated, subhedral crystal pellets of 0.3-0.7 millimeters in length, and small, equant fragments of 0.05-0.1millimeters in diameter. The red color could not be recognized in the thin section.

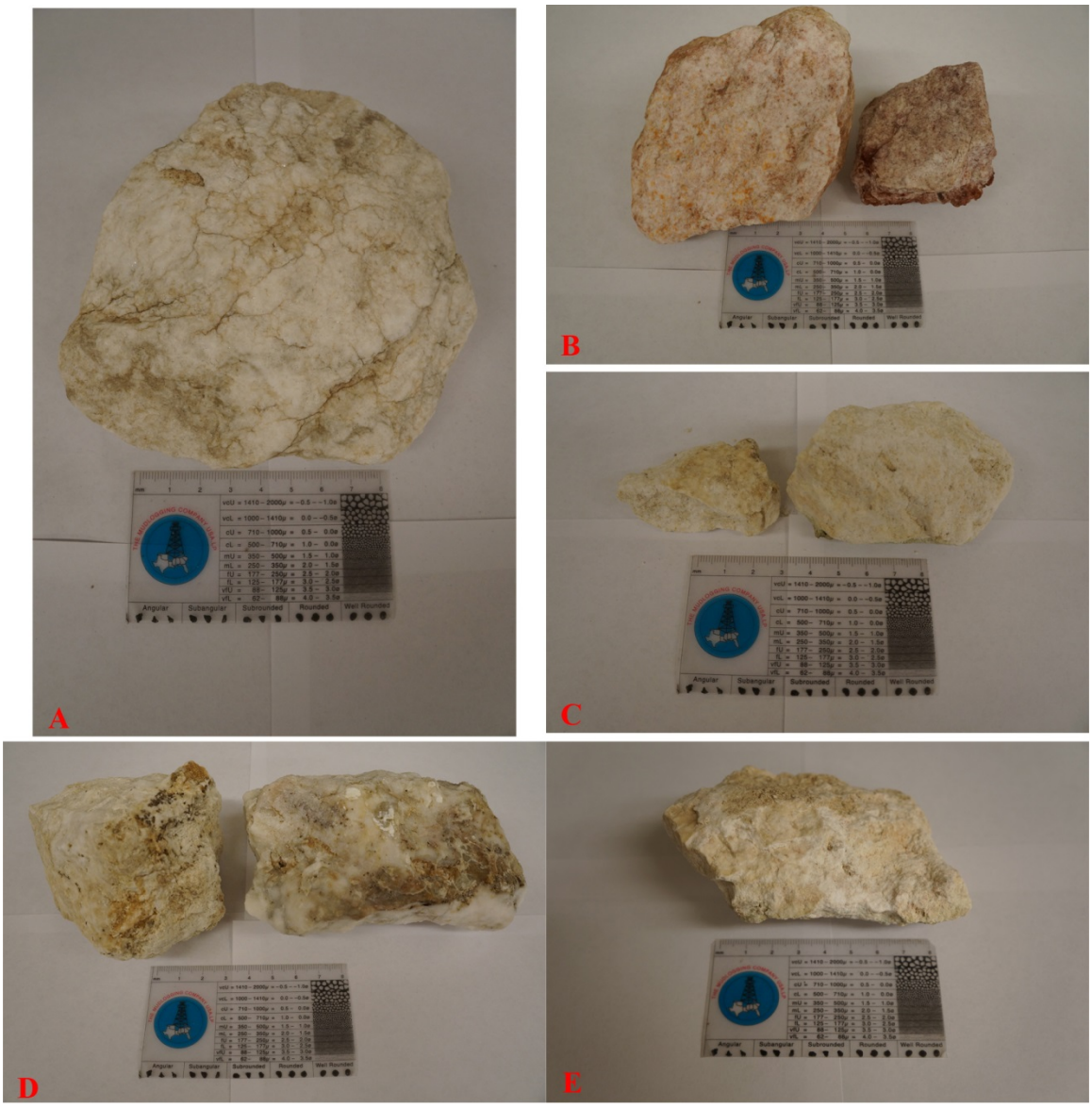

Figure 3-10, Hand samples of gypsum samples: A) unaltered Gypsum-White, B) unaltered Gypsum-Red, C) altered Gypsum-1, D) altered Gypsum-2, and E) altered Gypsum-3. All gypsum samples are massive.

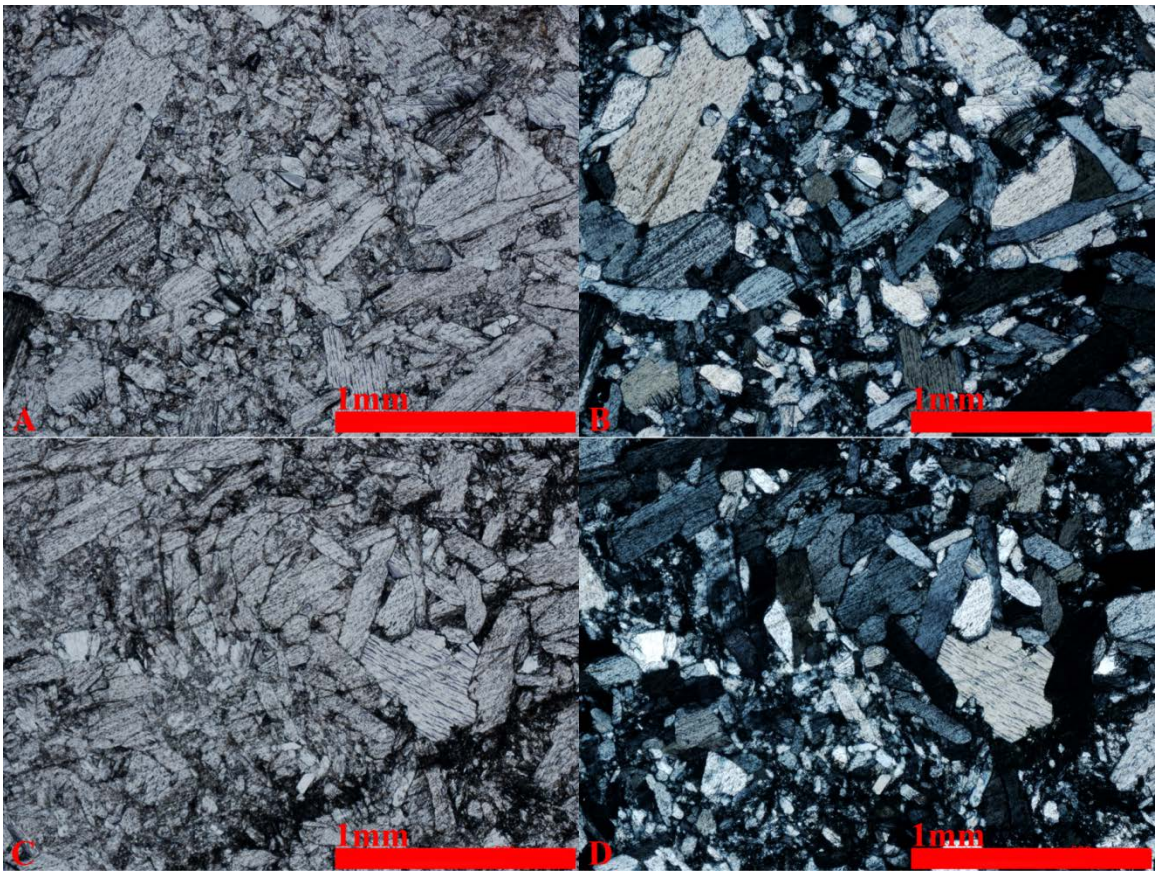

Figure 3-11, Photomicrographs of unaltered gypsum samples, A) and B) Gypsum-White, C) and D) Gypsum-Red..

The three altered gypsum samples (Fig. 3-12) show crystallization gradient: Gypsum-1 has smaller anhedral crystal pieces of about 0.3 millimeters in diameter, and irregular, pervasive gypsum; Gypsum-2 has almost no crystal pellets but their relics, and more irregular, pervasive gypsum than Gypsum-1; Gypsum-3 has no crystal pieces but all irregular, pervasive gypsum. No carbonate was observed in these thin sections.

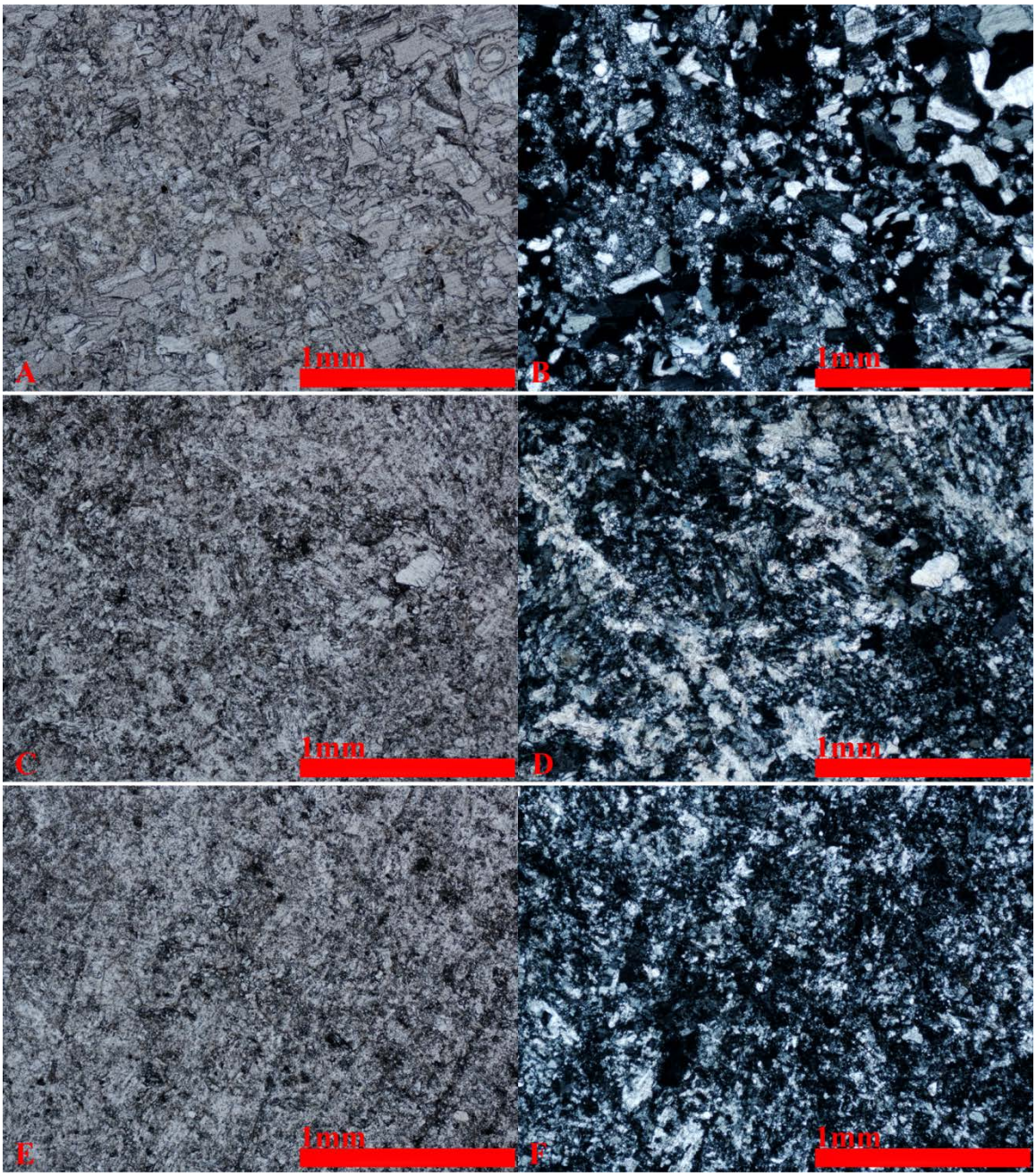

Figure 3-12, Photomicrographs of altered gypsum samples, A and B showing sample Gypsum-1, C and D showing sample Gypsum-2, E and F showing sample Gypsum-3, note the crystallization gradient in these samples.

4. Spectroscopy

4.1. Introduction

Spectroscopy is the study of the emission, reflection, and scattering of light as a function of wavelength (Clark, 1999). When photons encounter the surface of a medium, some are reflected, some are transmitted, and some are absorbed. Reflected photons can be detected and measured by spectrometers, and the ratio of intensity of reflected light versus incident light is called reflectance. Diagnostic features in reflectance spectra are caused by vibrational overtones, electronic transitions, charge transfer, and conduction processes, thus containing information about the chemistry of materials (Hunt, 1977). As a result, we can use reflectance spectra to identify various kinds of materials, and provide spectral reference for remote sensing imagery. United States Geological Survey has published 6 versions of spectral library, including samples of minerals, rocks, soils, mixtures, plants, vegetation communities, micro-organisms, and man-made materials (Clark et al., 2007). This library provides a knowledge base for spectroscopy of minerals as well as related materials, and permits accurate definitions of absorption features in spectra. By comparing with the spectral library, unknown spectra could be analyzed and chemical information contained in spectral features could be revealed.

As stated before, loss of iron and impregnation of sandstone by carbonate cements and replacement of gypsum by calcite are the major alteration phenomena in Cement field, Oklahoma (Donovan et al., 1979b). In this study, the main focus is to detect ferrous iron and calcite in the sandstone.

Ferric iron minerals show several absorption features in VNIR spectral range caused by crystal field effects of Fe^{3+} (F_{515}, F_{668}, and F_{900}) (Murphy et al., 2014). All major ferric iron minerals like goethite (α-FeO(OH)), limonite ($FeO(OH)\cdot nH_20$), and hematite (Fe_2O_3), have these 3 absorptions

in visible and near-infrared spectral range. Ferrous iron minerals like pyrite, pyrrhotite, and siderite, on the other hand, do not have these absorptions (Fig. 4-1). Magnetite has both ferric and ferrous iron, but the reflectance spectrum does not show major absorption features of ferric iron. Based on these differences, information about the existence of ferric iron minerals could be extracted from image and ASD spectra. F_{515} and F_{668} are relatively small. We mainly use F_{900} to identify ferric iron in spectra. Besides, the wavelength positions of F_{900} are different among ferric iron minerals: hematite has F_{900} at 852 nm, goethite has F_{900} at 926 nm, and limonite has F_{900} at 945 nm. This could be used to identify minerals in whole rock samples.

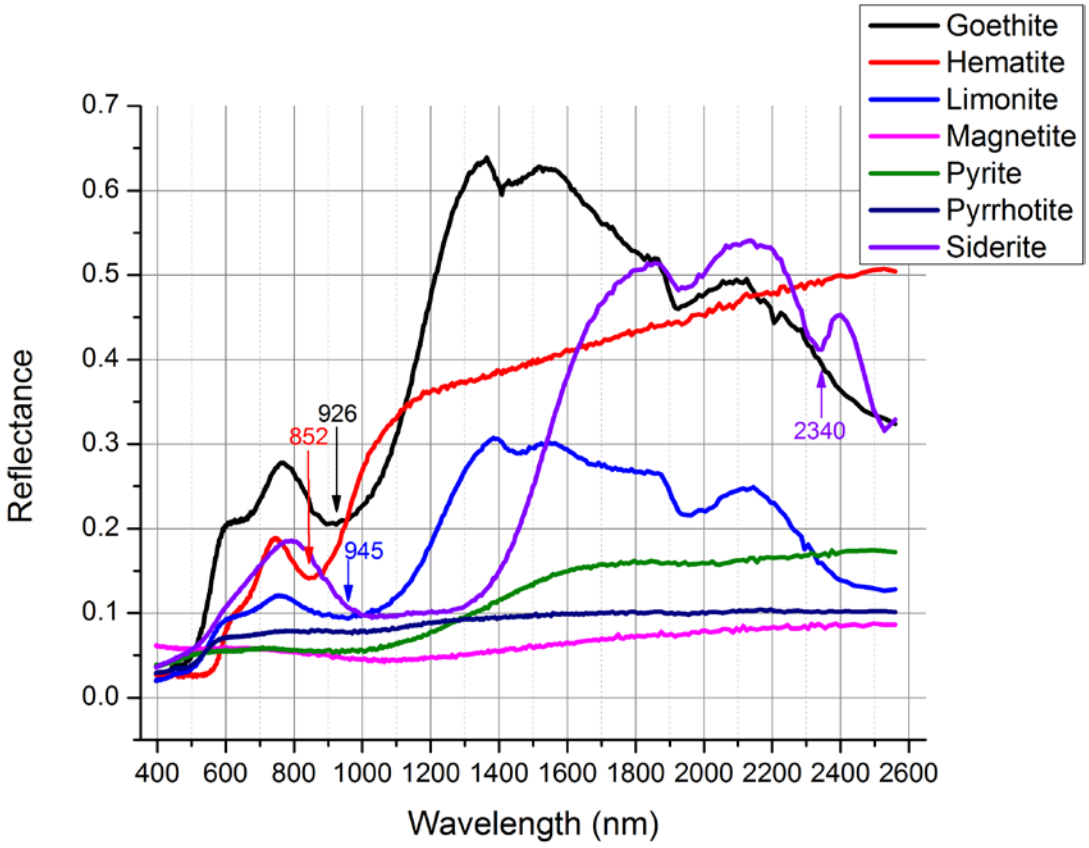

Figure 4-1, Spectra of iron minerals, wavelength positions of F_{900} are marked by arrows. Data from Clark et al. (2007).

Gypsum has major absorption features at 1445 nm, 1750 nm, 1945 nm and 2215 nm, and minor absorption features at 1000 nm, 1200 nm, 1490 nm, 1535 nm, and 2265 nm. The two major calcium carbonate have very similar spectral shape: calcite has major absorption features at 2340 nm and 2530 nm, and minor absorptions at 1875 nm, 1995 nm, and 2165 nm; dolomite has a violet-shift of about 20nm for every absorption feature (Fig. 4-2). All minor absorptions of calcium carbonates are masked by gypsum absorption features; the 2530 nm absorption is out of the wavelength range, so the only indicator of carbonate in gypsum is the 2340 nm feature.

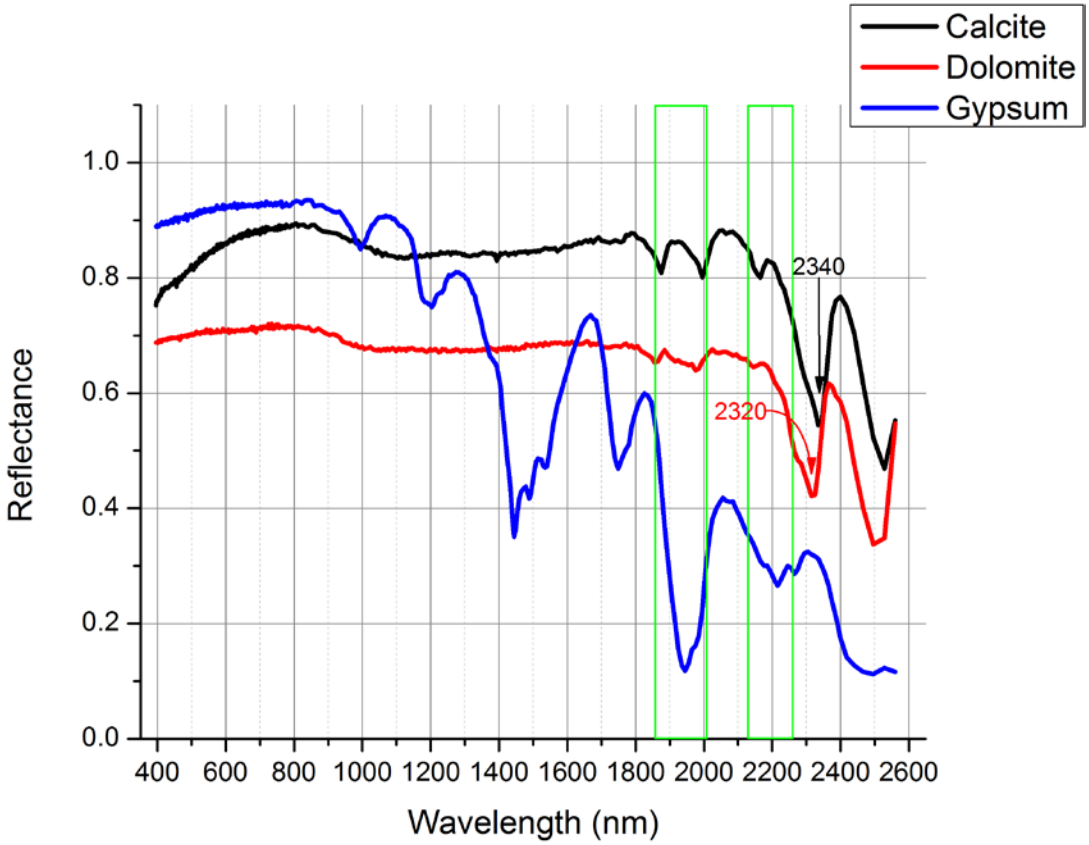

Figure 4-2, Spectra of gypsum and carbonates. Wavelength positions of recognizable absorption features of carbonates are marked by arrows, green rectangle mark minor absorption features of carbonates which would be masked by gypsum. Data from Clark et al. (2007).

Azurite has major absorption features at 1500 nm, 2045 nm, 2290 nm, and 2350 nm, as well as a reflectance peak at 453 nm. Malachite has major absorption features at 2270 nm, and 2355 – 2430 nm, as well as a reflectance peak at 537 nm. Other copper minerals do not have prominent features to be recognized from spectra (Fig. 3-3).

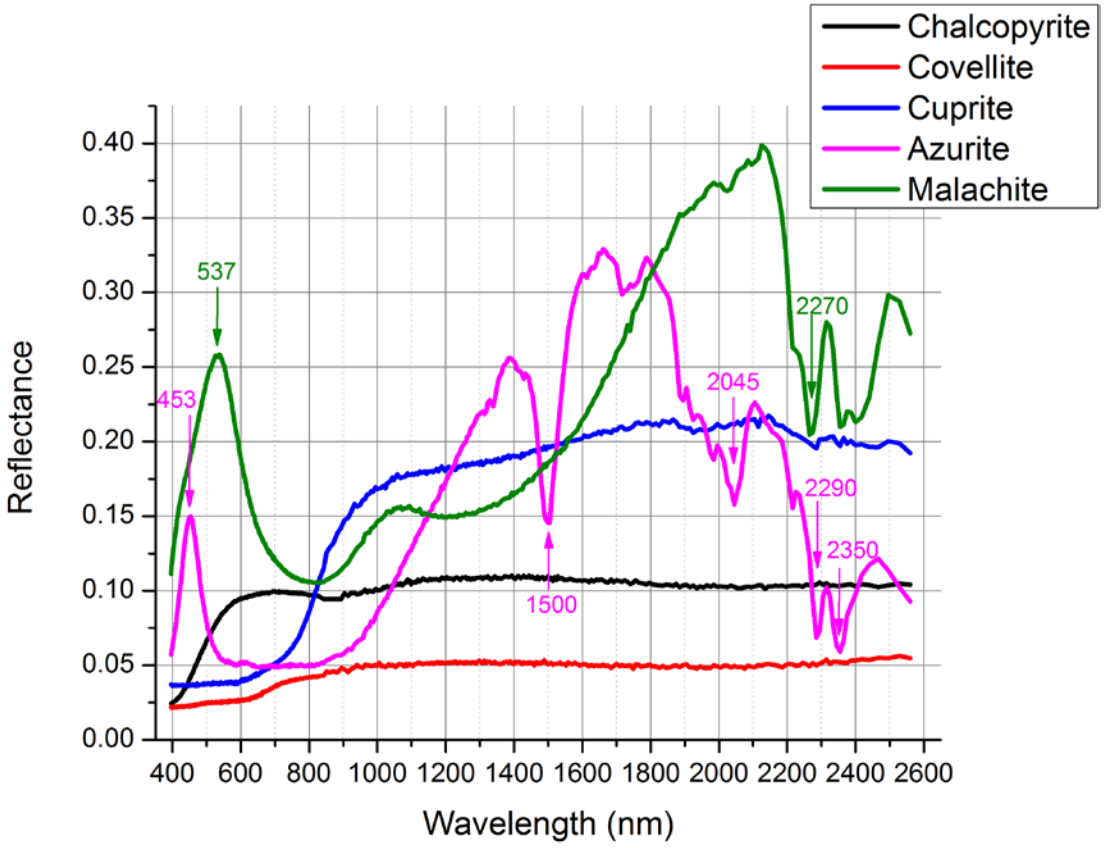

Figure 4-3, Spectra of copper minerals, wavelength positions of major features are marked by arrows, data from Clark et al. (2007).

Based on spectroscopy, we could build laboratory spectral references for data processing in remote sensing imagery. Bands of interest in remote sensing could also be extracted from spectra plots.

4.2 Methods

In this study ASD FieldSpec Pro spectroradiometer was used to collect laboratory spectra. The FieldSpec Pro system (Fig. 4-4) is a high performance, single-beam portable spectrometry device manufactured by the Analytical Spectral Devices, Inc. (now PANalytical Boulder); it is able to provide standard or reference spectra for scientific or industrial applications. The spectroradiometer covers 350 – 2500 nm wavelength range with 1 nm band interval, 3 nm spectral resolution in VNIR region, and 10 nm spectral resolution in SWIR region. There are three sensors in the system: VNIR, SWIR1, and SWIR2, covering 350 – 1000 nm, 1001 – 1830 nm, and 1831 – 2500 nm, respectively. A lot of remote sensing workers have reported the applications of ASD spectrometer to build reference libraries (Peddle et al., 2001; Vermote et al., 2002; Herold et al., 2004).

Figure 4-4, ASD Fieldspec Pro spectroradiometer, photo taken in the lab.

ASD spectra of field samples were taken in the laboratory in early-November, 2013. An average of three measurements was calculated for each sample. During the measurements, the system loses continuation frequently between contiguous sensors, displaying spectral curve jumps at 1000 – 1001 nm and 1830 – 1831 nm. These jumps were corrected by subtracting all the VNIR and SWIR2 reflectance values by the differences between the sensors. This process makes the spectra continuous without changing the spectral wavelengths of absorption features.

4.3 Results

4.3.1 Sandstones

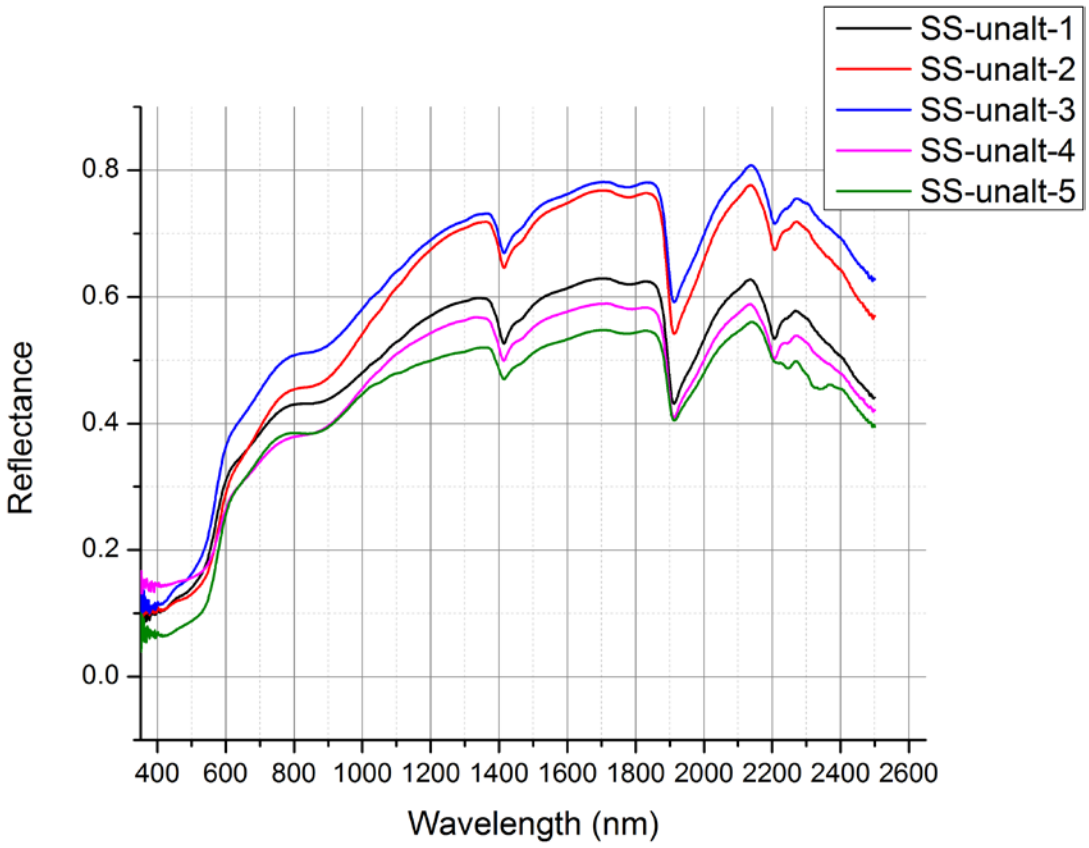

Figure 4-5, Spectra of unaltered Rush Springs sandstones, from Cement field, Oklahoma. Ferric iron absorption features could be identified in the VNIR spectral range.

ASD spectra of the unaltered sandstones (Fig. 4-5) show major absorption features at about 900 nm, 1415 nm, 1915 nm, and 2207 – 2215 nm, and minor absorptions at about 510 nm, 670 nm, and 1770 nm. Clear F_{900} absorption trough could be identified from all spectra of unaltered sandstones; F_{515} and F_{668} are also recognizable.

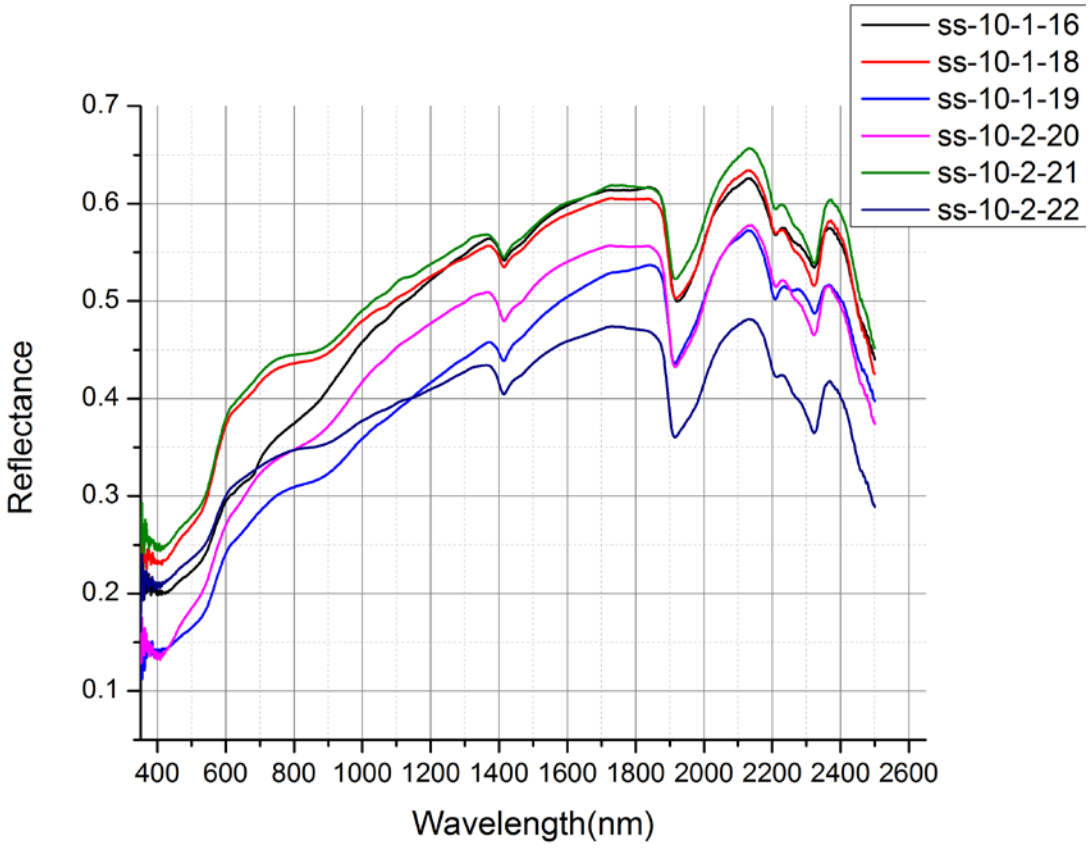

Figure 4-6, Spectra of sample sandstone-10. These spectra have shallower ferric iron absorption features compared with the unaltered sandstones. Absorption features at 2322 nm indicate dolomite.

ASD spectra of sample sandstone-10 (Fig. 4-6) have strong absorption features at 1413 nm, 1915 – 1920 nm, 2209 – 2215 nm, and 2322 nm. The 2322 nm absorption feature indicates the

existence of dolomite. Shallower F_{900} troughs compared with the unaltered sandstones could be identified from the spectra.

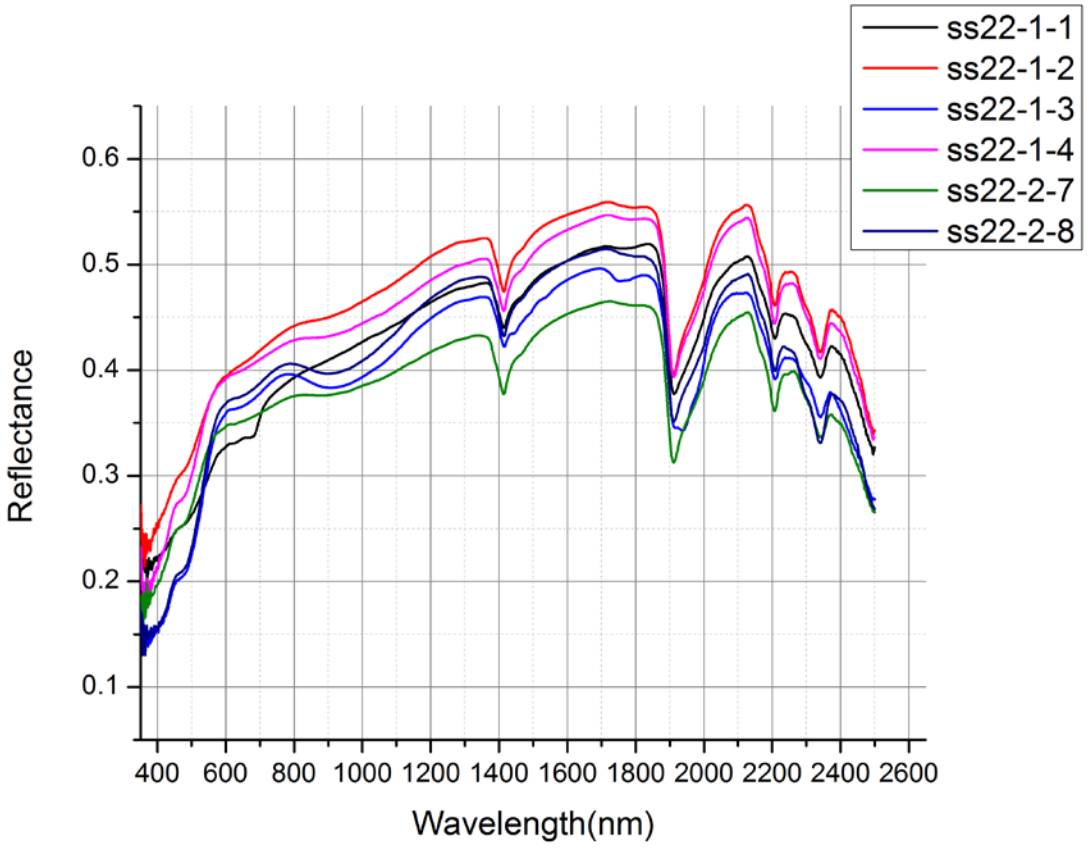

Figure 4-7, Spectra of sample sandstone-22. Absorption features at 2340 nm indicate calcite. Two spectra (SS22-1-1 and SS22-1-3) which were taken on reddish-brown bands on the sample show ferric iron absorption features.

ASD spectra of sample sandstone-22 (Fig. 4-7) have strong absorption features at 1413 nm, 1912 nm, 2208 nm and 2340 nm. The 2340 nm absorption feature indicates the presence of calcite in this sandstone. Two spectra were taken on reddish-brown bands, resulting in F_{900}, F_{515}, and F_{668} troughs in spectra.

ASD spectra of Cement factory samples were quite variable. Major absorption features were observed at about 1410 – 1440 nm, 1910 – 1940 nm, and 2320 nm.

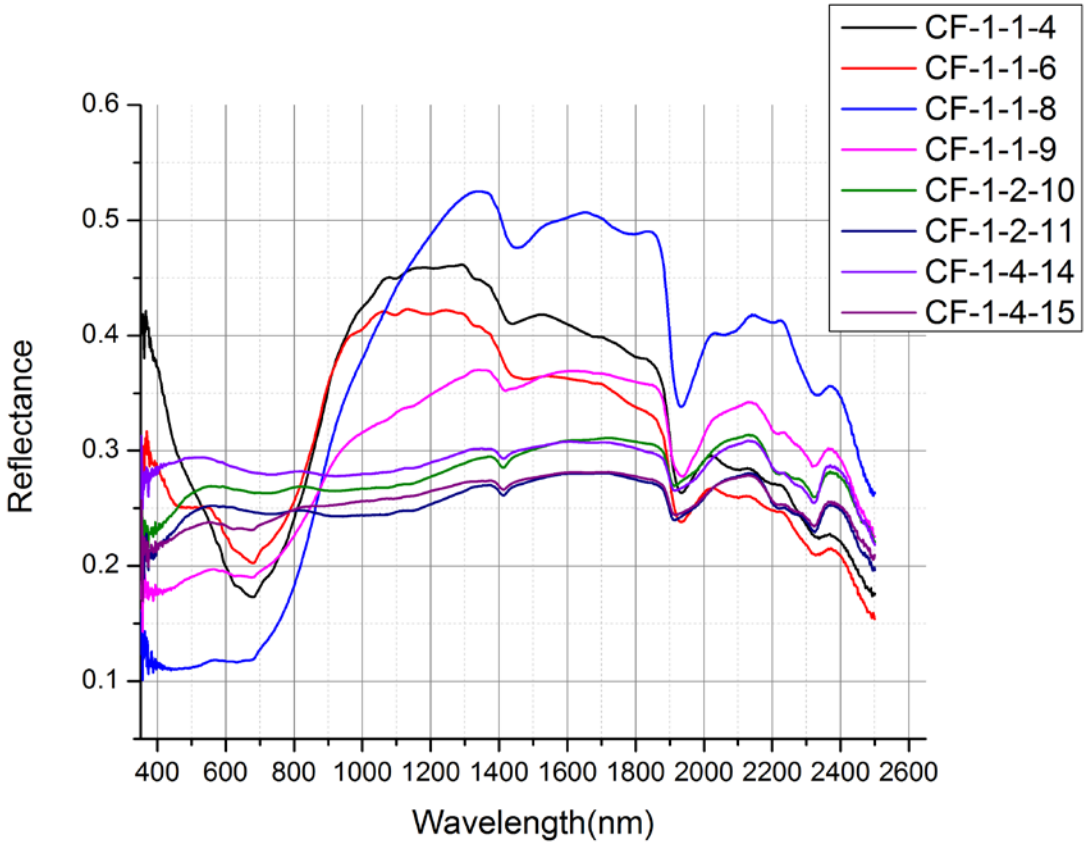

Figure 4-8, Spectra of sandstone sample CF-1.These spectra were taken on a dark exposed surface and a grey fresh surface, resulting in two different kinds of spectra. Absorption features at 2322 nm indicate dolomite.

Sample CF-1 has a dark exposed surface and grey fresh surface. Spectra of the dark surface (CF-1-1-4, 6, 8, and 9 in Fig. 4-8) have lower reflectance than those of the grey surface (CF-1-1-10, 11, 14, and 15) in the visible spectrum, and higher reflectance in the NIR spectrum. They also have broader and deeper absorption features at longer wavelengths compared to the grey surface.

Spectra CF-1-1-4 and CF-1-1-6 show very broad absorption trough at 450 – 900 nm with a minimum at about 680nm.

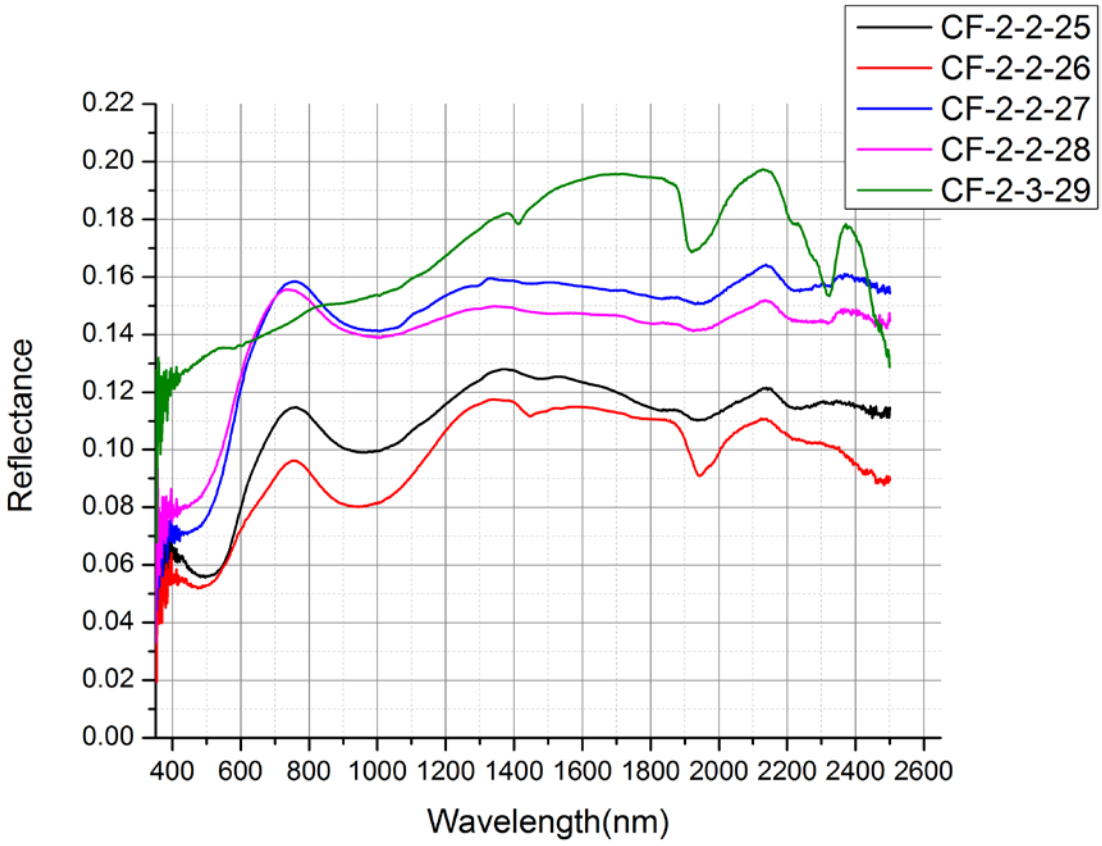

Figure 4-9, Spectra of sandstone sample CF-2. Most of these spectra were taken on the rusty surface and show ferric iron absorption features but no hydroxyl and carbonate absorptions. CF-2-3-29 was taken on a fresh grey surface and shows hydroxyl and dolomite absorptions but no ferric iron absorptions.

Sample CF-2 (Fig. 4-9) has pyrite – iron oxide surface alterations (Fig. 3-5, A, B, and C). Spectra of surface alterations do not show major absorptions observed on spectra of fresh surfaces, but they have a clear F_{900} trough, which is an evidence of ferric iron. CF-2-3-29 was taken on a fresh surface; it didn't show ferric iron absorptions but hydroxyl and carbonate absorptions.

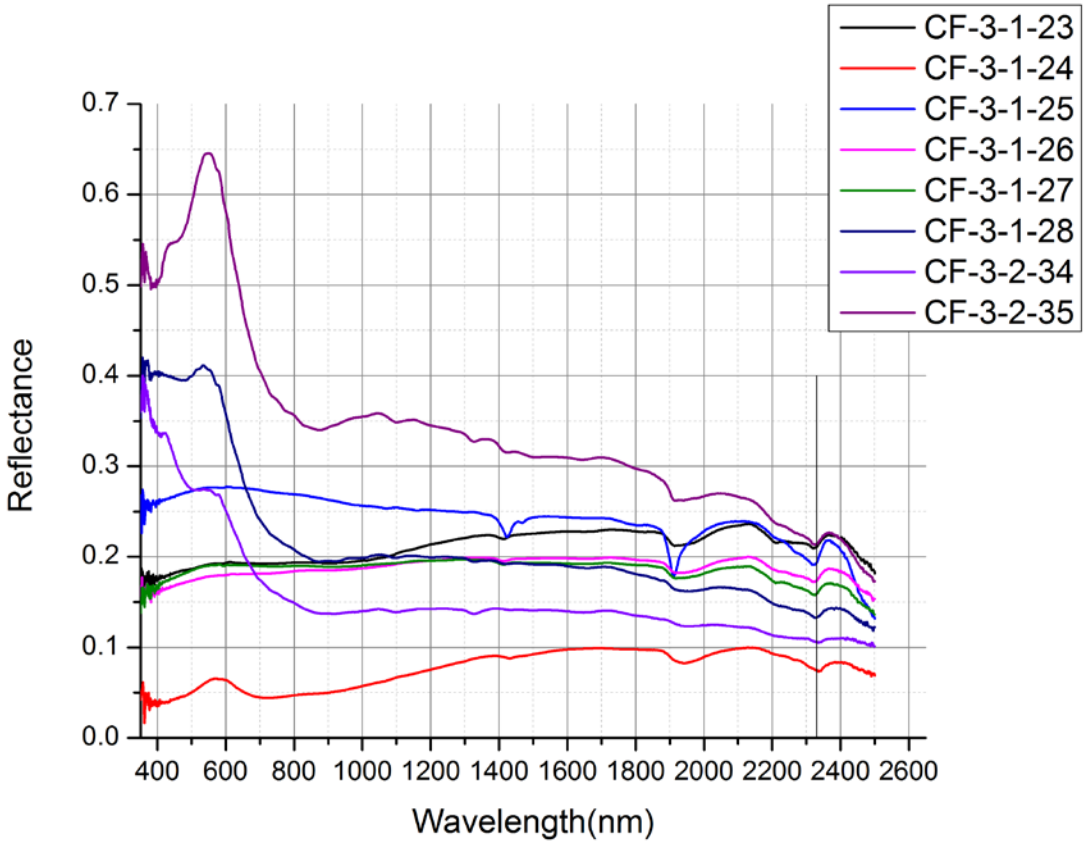

Figure 4-10, Spectra of sandstone sample CF-3. Some spectra were taken on brownish green surface alterations and show reflectance peaks at 550 – 570 nm, they were probably associated with copper. Most spectra have 2325 nm absorptions indicating dolomite, while CF-3-1-24 has a 2336 nm absorption feature indicating calcite. The black line shows the wavelength position of 2330 nm.

Sample CF-3 (Fig. 4-10) has brownish green surface alterations (Fig. 3-5, E and F). Spectra of these alterations (CF-3-1-24, 3-1-28, 3-2-34, and 3-2-35 in Fig. 4-10) show a reflectance peak at 550 – 570 nm in coincidence with the green color. A possible origin of this reflectance peak is copper. Spectrum CF-3-1-24 has an absorption feature at 2336 nm indicating calcite in this spectrum, whereas dolomite was found in other spectra. The black line in the figure indicates wavelength at 2330 nm.

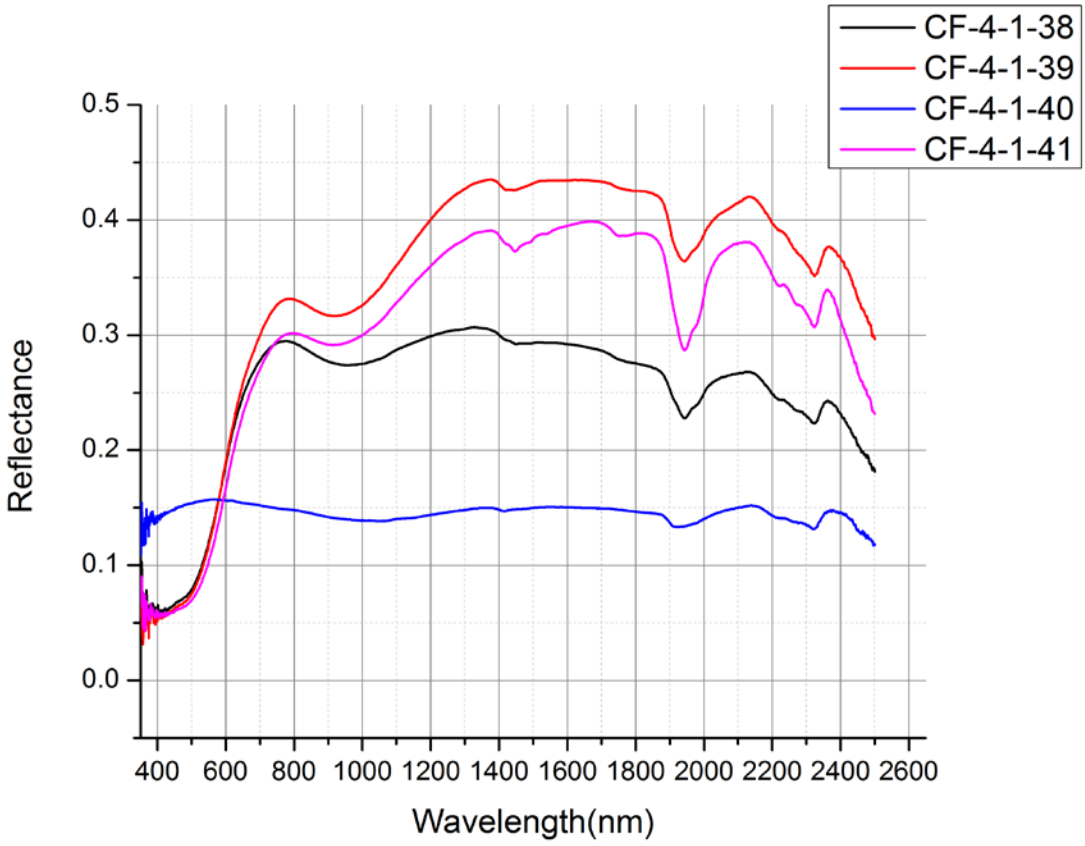

Figure 4-11, Spectra of sandstone sample CF-4. Most of these spectra were taken on the rusty surface and show ferric iron absorption features. CF-4-1-40 was taken on a fresh grey surface and shows no ferric iron absorptions. Absorption features at 2324 nm indicate dolomite.

Sample CF-4 has iron oxide surface alterations (Fig. 3-5, D). Spectra of surface alterations (CF-4-1-38, 39, and 41 in Fig. 4-11) have major absorptions at 1440 nm, 1940 nm and 2325 nm, which are not observed on spectra of alteration sites on CF-2; however they do have a clear F_{900} trough, which is an evidence of ferric iron. CF-4-1-40 was taken on a fresh surface and did not show ferric iron absorptions.

Sample CF-7 (Fig. 4-12) is mostly yellow in color, except from the two spectra (CF-7-2-53 and 54) taken on whitish spots. All spectra show broad F_{900} trough. All CF-7 spectra have a deep 2323 nm absorption feature, a deep 1940 nm absorption feature, and a shallow 2215 nm absorption feature.

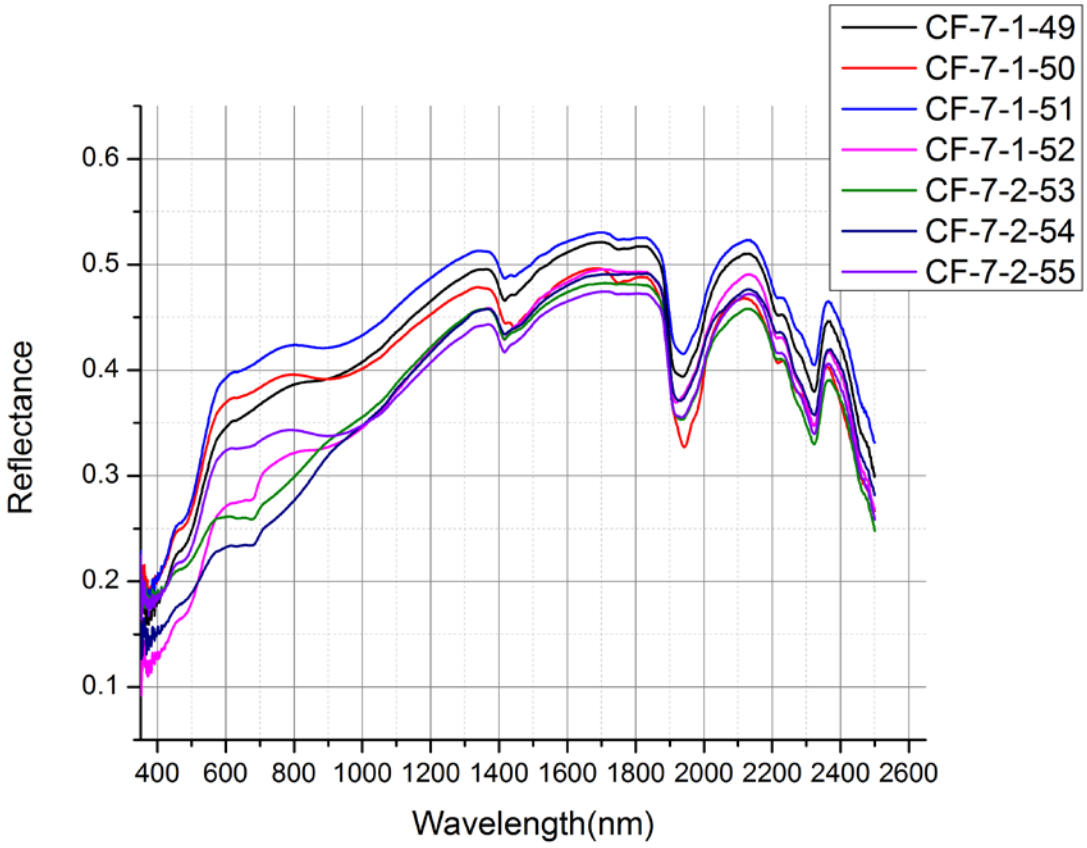

Figure 4-12, Spectra of sandstone sample CF-7. Most spectra show ferric iron absorption features. Deep absorption features at 2323 nm indicate dolomite.

Sample CF-9 (Fig. 4-13) has a color transition from yellow to light grey. Spectra taken on the yellow area show clear F_{900} troughs; however spectra of the grey area do not. All spectra have a deep absorption feature at 2335 nm.

The major absorption features in these spectra indicate the presence of clay minerals. Band ratio calculations suggest that there is not much kaolinite, but illite in these sandstones. Most spectra do not have F_{900} trough, meaning that most ferric iron has been reduced.

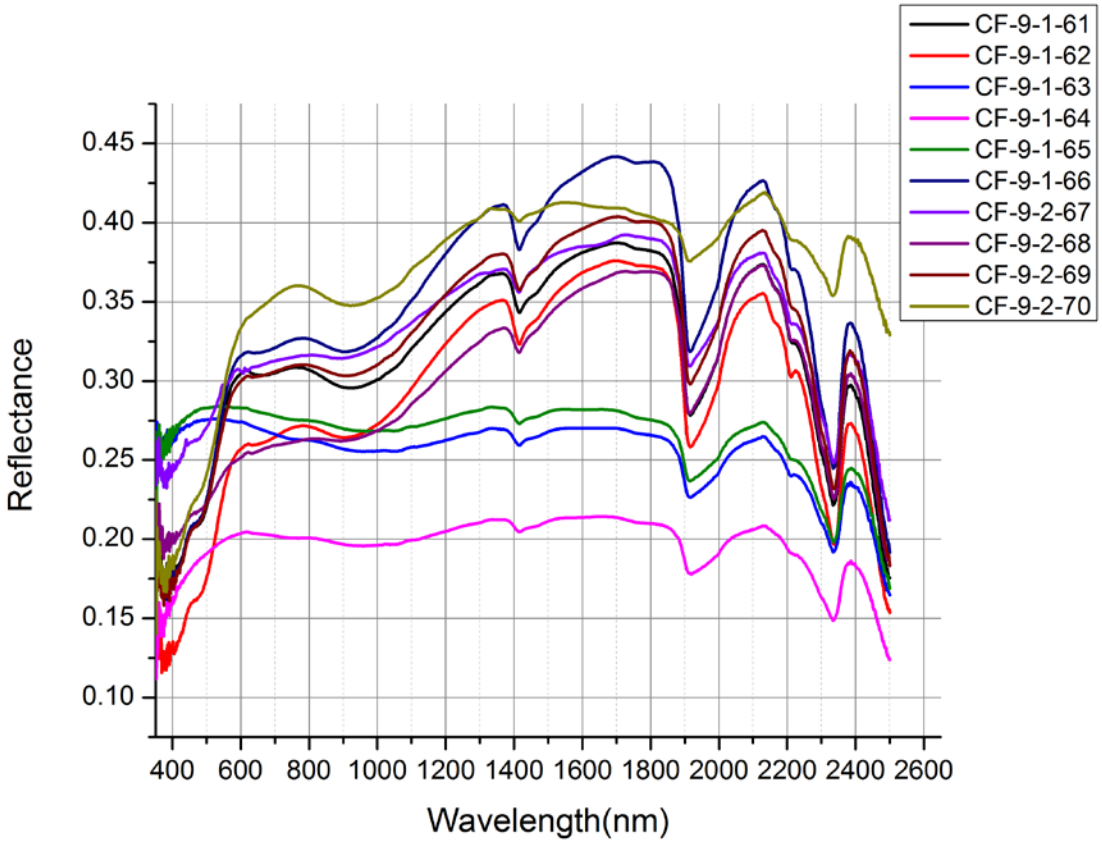

Figure 4-13, Spectra of sandstone sample CF-9. Some spectra were taken on the yellow area and show clear ferric iron absorptions, whereas the other spectra taken on the grey area do not show ferric iron absorptions. Absorption features at 2335 nm indicate calcite.

ASD spectra of most the sandstone samples have a 2325 nm absorption feature, while C-F-9 and Sandstone-22 have a 2335nm absorption feature, indicating the impregnation of dolomite in most sandstone samples, and calcite in these two samples.

4.3.2 Gypsum Samples

Nine ASD spectra (Fig. 4-14) are taken for 2 unaltered gypsum samples. These spectra show all major and minor absorption features found in the spectral library. In addition, spectra of the Gypsum-Red show a broad absorption feature at about 480 – 540 nm.

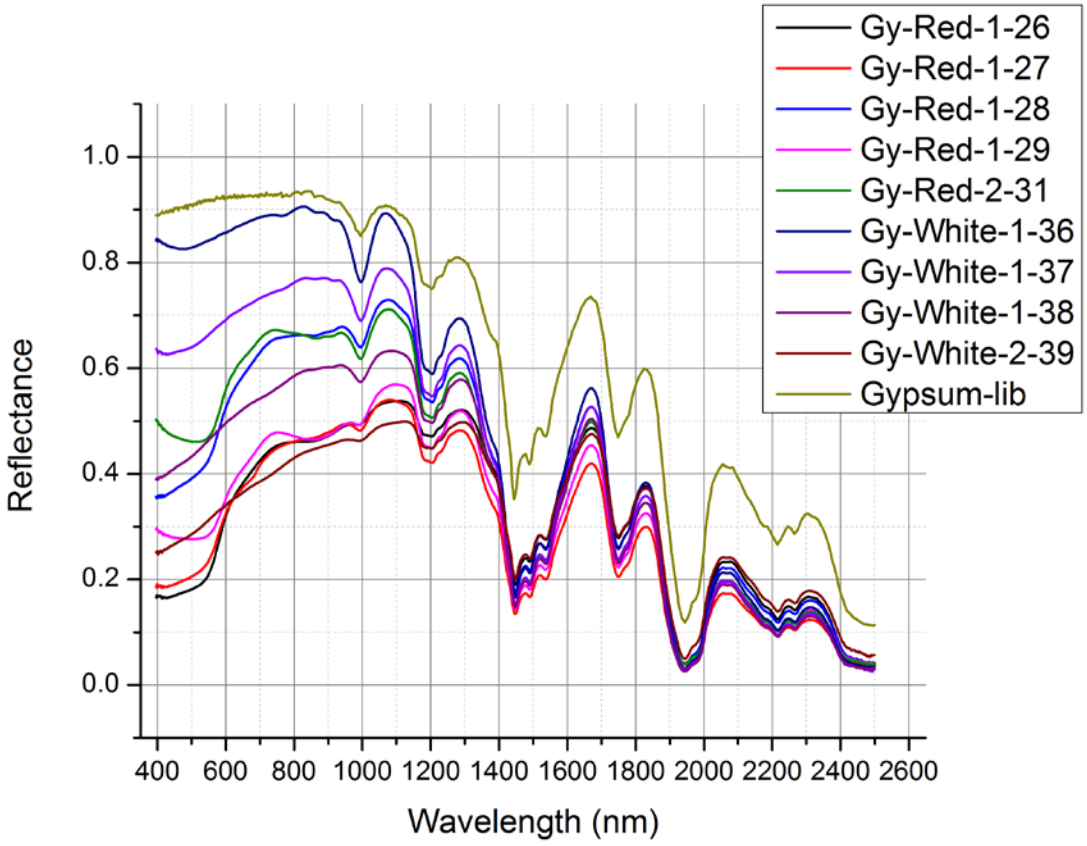

Figure 4-14, Spectra of unaltered gypsum samples compared with the spectral library. All the spectra of unaltered samples have the same absorption features with the spectrum from spectral library.

Twenty-three ASD spectra (Fig. 4-15, 16, 17) were taken for the 3 altered gypsum samples. These spectra show all major and minor absorption features in gypsum spectral library. Four spectra of surfaces on samples Gypsum-1and Gypsum-2 have minor absorption features at 437

nm, 490 nm, 627 nm, and 678 nm, and a big increase in reflectance near 700 nm. This phenomenon is believed to be caused by vegetation. Five spectra of surfaces on samples Gypsum-2 and Gypsum-3 have broad absorptions at 480-540nm. No spectra of altered gypsum samples have a 2325 – 2340 nm absorption trough, indicating that there are no detectable carbonates in gypsum samples collected; this is also confirmed in the petrographic observation. No significant spectral difference has been identified among the 3 altered gypsum samples.

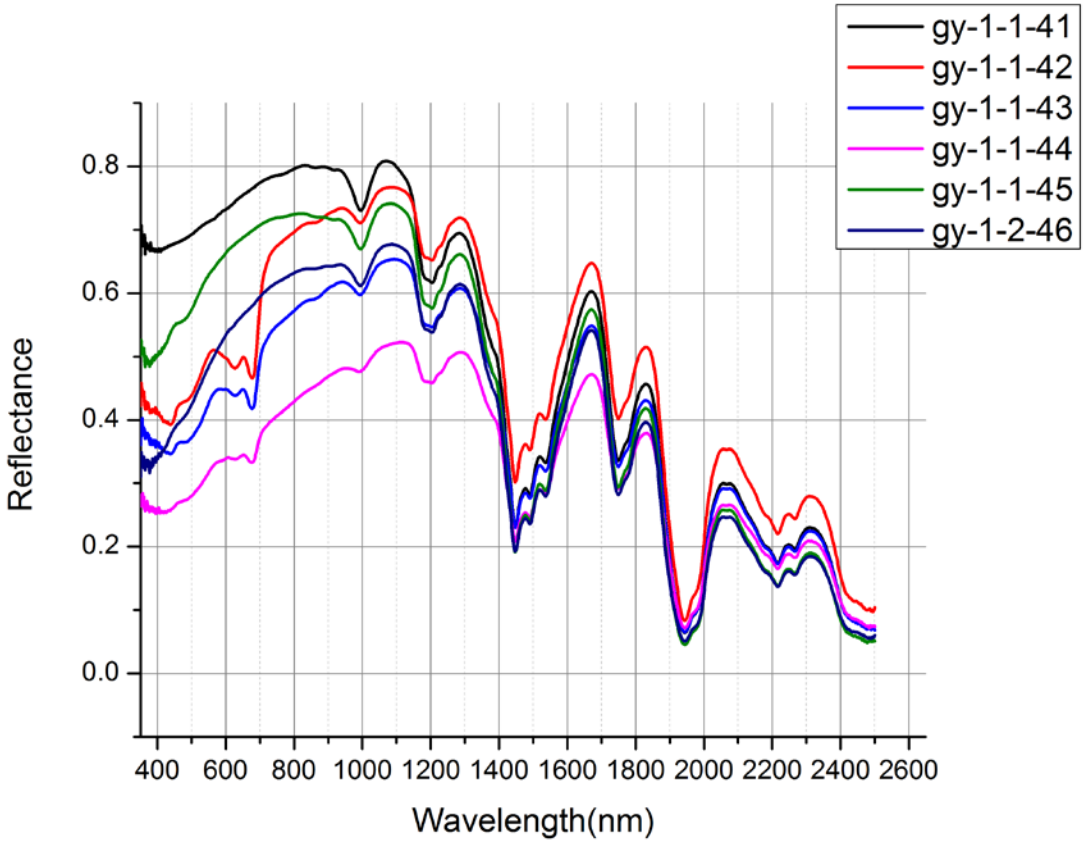

Figure 4-15, Spectra of sample Gypsum-1. They have all absorption features in spectral library and no carbonate absorptions.

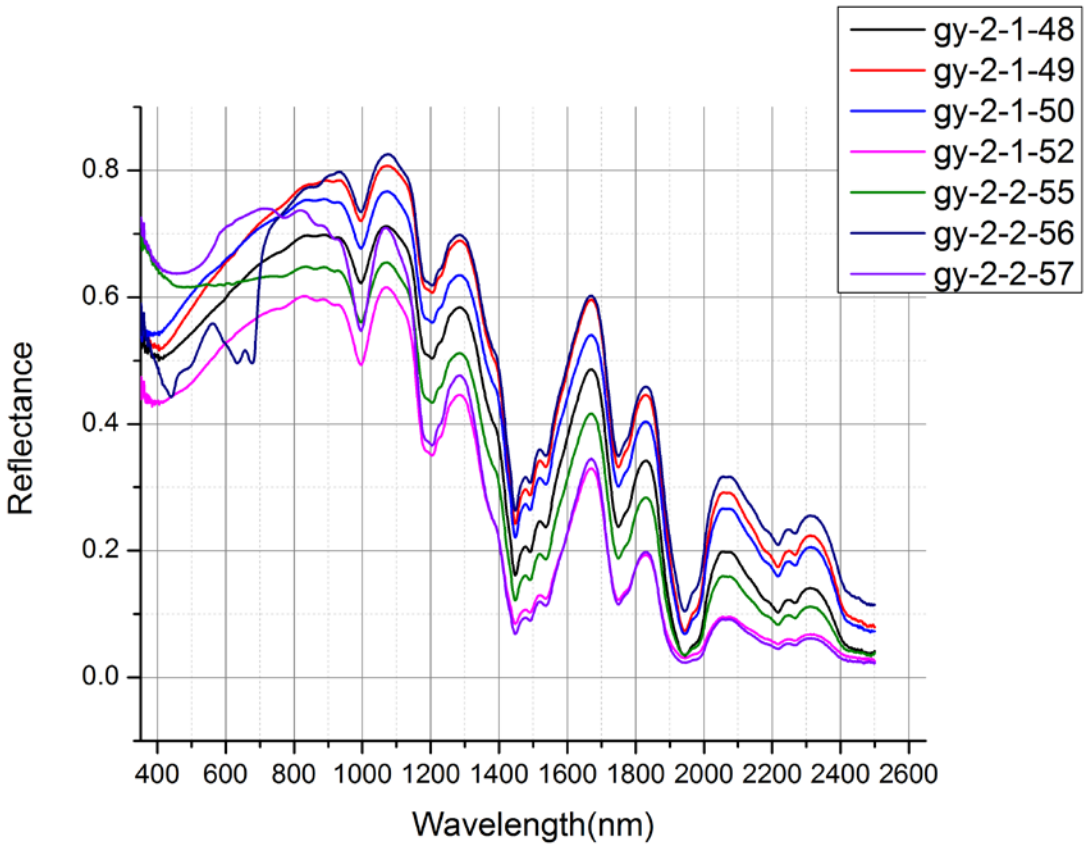

Figure 4-16, Spectra of sample Gypsum-2. They have all absorption features in spectral library and no carbonate absorptions.

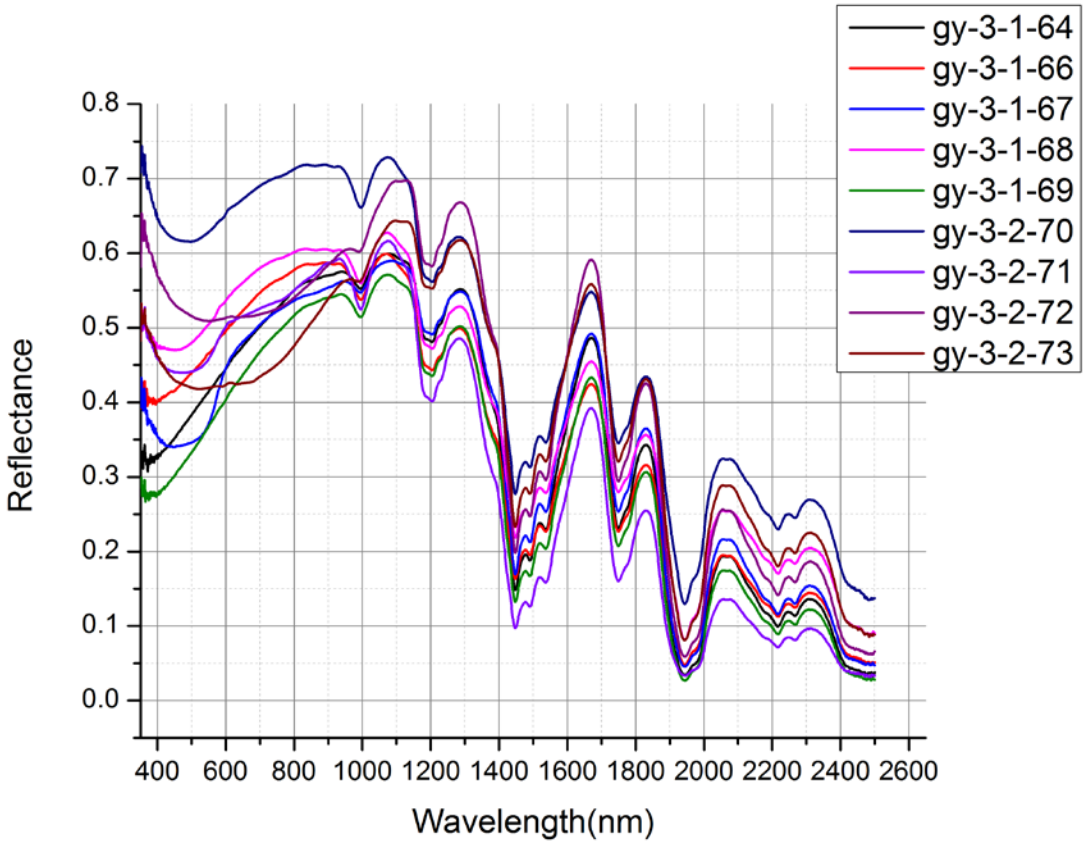

Figure 4-17, Spectra of sample Gypsum-3. They have all absorption features in spectral library and no carbonate absorptions.

5. Remote Sensing Imagery

5.1 Introduction

Remote sensing is the acquisition, processing, and interpretation of measurements of radiation reflected and emitted from the earth's surface by a sensor at a distance from the object (Campbell, 2002). The practice of remote sensing began in mid-19th century when aerial photographs were taken with the help of balloons, kites, and pigeons. Wilber Wright was the first person to take an aerial photograph from an airplane in 1910. Later in the two World Wars, aerial photographs were extensively used for mapping and reconnaissance. In 1972, the launch of Landsat 1 marked a great advance of remote sensing in satellite imagery. From then on many remote sensing satellites have been launched by various countries. Most of these satellite sensors, like Landsat ETM+, Landsat 8, ASTER, and SPOT, have several broad bands of about 100 nm wide, and several spectral gaps between bands. They are called multispectral sensors. Comparing with multispectral techniques, hyperspectral sensors have tens or hundreds of bands of equal spectral width and full spectrum coverage. In the 1980s the first airborne hyperspectral sensors became available, Airborne Imaging Spectrometer (AIS) and Airborne Visible / Infrared Imaging Spectrometer (AVIRIS) are most known. In 2003, the first successful satellite-based hyperspectral sensor, Hyperion, was launched. Now remote sensing is rapidly developing towards higher and higher spatial, spectral and temporal resolution.

Remote sensing imagery collects photographs of the ground in several spectral bands; each band collects emitted or reflected radiance at a spectral range. For each pixel in a remotely sensed image, a spectrum could be derived and physical and chemical information could be resolved from it. A lot of work in spectroscopy has been done to provide the basis for remote sensing imagery. In this way, field spectra collected with remote sensing instruments could be interpreted

and this information can be used for delineating surface geology. In this study, the main focus for remote sensing is to resolve mineral combinations and detect rock alterations.

5.2. Methods

5.2.1 Multispectral Remote Sensing

Multispectral imaging has several broad bands that are not “continuous”, as the bands do not cover the solar reflection range (0.4 – 2.5 μm) but have several gaps. Numerous multispectral sensors are available: low spatial resolution sensors like AVHRR, MODIS, and SeaWiFS; intermediate spatial resolution sensors like Landsat, SPOT, and ASTER; high spatial resolution sensors like IKONOS, QuickBird, GeoEye, and WorldView. Most high resolution sensors are commercial; in this study we use two of the most popular intermediate resolution satellite imagery systems whose data is free: Landsat 8 and ASTER.

5.2.1.1 Landsat 8

The Landsat 8 (Landsat Data Continuity Mission) system was launched on February 11, 2013. Landsat 8 is equipped with two sensors: the Operational Land Imager (OLI) and the Thermal Infrared Sensor (TIRS). OLI provides two new spectral bands, and has a different band designations compared with the Thematic Mapper (TM) on Landsat 4 and 5, as well as the Enhanced Thematic Mapper (ETM+) on Landsat 7 (Table 5-1). All bands listed have a spatial resolution of 30 meters. Landsat 8 has a sun-synchronous orbit at 705km, orbiting the earth every 98.9 minutes, and covers the same area every 16 days (http://landsat.usgs.gov/about_ldcm.php). The equatorial crossing time is about 10:00 am. Each Landsat scene has dimensions of 170 km × 185 km.

Wavelength (micrometers)	TM	ETM+	OLI
0.43 – 0.45			Band 1 – Coastal aerosol
0.45 – 0.52	Band 1	Band 1	Band 2 – Blue
0.53 – 0.59	Band 2	Band 2	Band 3 – Green
0.64 – 0.67	Band 3	Band 3	Band 4 – Red
0.85 – 0.88	Band 4	Band 4	Band 5 – Near Infrared (NIR)
1.57 – 1.65	Band 5	Band 5	Band 6 – SWIR 1
2.11 – 2.29	Band 7	Band 7	Band 7 – SWIR 2
1.36 – 1.38			Band 9 – Cirrus

Table 5-1, Band names and wavelengths in different Landsat sensors, redrawn after http://landsat.usgs.gov/band_designations_landsat_satellites.php

5.2.1.2 ASTER

The Advanced Spaceborne Thermal Emission and Reflection Radiometer (ASTER) is an imaging system on the NASA Terra satellite launched on December 18, 1999. ASTER is a cooperative mission between the United States and Japan. ASTER consists of three separate subsystems: VNIR, SWIR, and TIR; each has different spatial resolution (Table 5-2). The backward-looking near-infrared Band 3B has the same wavelength range but different looking angle from the nadir-looking Band 3, thus providing stereo coverage. The Terra satellite has the same orbit as Landsat 8, but flies later than Landsat 8 with an equatorial crossing time at about 10:30 am (http://asterweb.jpl.nasa.gov/eos.asp). ASTER has a smaller swath width compared with Landsat 8; each scene covers 60 km × 65 km on ground.

Wavelength (micrometers)	Subsystem	Band Names	Spatial Resolution (meters)
0.52 – 0.60	VNIR	Band 1	15
0.63 – 0.69	VNIR	Band 2	15
0.76 – 0.86	VNIR	Band 3	15
0.76 – 0.86	VNIR	Band 3B	15
1.60 – 1.70	SWIR	Band 4	30
2.145 – 2.185	SWIR	Band 5	30
2.185 – 2.225	SWIR	Band 6	30
2.235 – 2.285	SWIR	Band 7	30
2.295 – 2.365	SWIR	Band 8	30
2.360 – 2.430	SWIR	Band 9	30
8.125 – 8.475	TIR	Band 10	90
8.475 – 8.825	TIR	Band 11	90
8.925 – 9.275	TIR	Band 12	90
10.25 – 10.95	TIR	Band 13	90
10.95 – 11.65	TIR	Band 14	90

Table 5-2, Band names and wavelengths, redrawn after http://asterweb.jpl.nasa.gov/characteristics.asp

5.2.2 Hyperspectral Remote Sensing

Hyperspectral imaging combines the power of digital imaging and spectroscopy. For each pixel in an image, a hyperspectral camera acquires the light intensity (reflectance) for a large number of bands on a continuous spectrum and can be used to characterize the objects in the scene with great precision and detail (Lillesand et al., 2004). Hyperspectral imaging provides much more

bands than a normal color camera, so it leads to an improved capability in identifying objects. Hyperspectral imaging has a wide range of applications, ranging from satellite based/airborne remote sensing to industrial quality control and lab applications. It is utilized in areas of mining, geology, forestry, agriculture, environmental management and so on.

Hyperspectral sensors image the scene line by line using a so-called "push-broom" scanning mode. One narrow spatial line in the scene is imaged at a time, and this line is split into its spectral components. On the two-dimension sensor array, one dimension is used for spectral separation and the second dimension is used for imaging in one spatial direction. The second spatial dimension in the scene arises from scanning the camera over the scene (Hui et al., 1998). By scanning, hyperspectral cameras collect slices from adjacent lines, forming a hyperspectral image or "cube", with two spatial dimensions and one spectral dimension.

This study uses two hyperspectral imaging systems, the satellite-based Hyperion, and the ground-based Specim cameras to detect hydrocarbon-induced surficial alterations.

5.2.2.1 Hyperion

Hyperion is a hyperspectral sensor mounted on the Earth Observing 1 satellite launched on November 21, 2000. It is the first hyperspectral sensor which has succeeded on a satellite platform. Hyperion provides a high resolution hyperspectral imager capable of resolving 220 unique spectral bands (total 242 bands) from 357nm to 2576 nm, within which 198 bands are calibrated (Beck, 2003). The spatial resolution of Hyperion is about 30m, and the spectral bandwidth is 10nm.This instrument orbits the earth in the same orbit as Landsat 8, and can image a 7.5km by 100 km land area per image. Hyperion contains a single telescope and two

spectrometers, one visible/near-infrared (VNIR) spectrometer (70 bands with CCD detector array) and one short-wave infrared (SWIR) spectrometer (172 bands with HgCdTe detector array).

5.2.2.2 Specim

Specim is a suite of hyperspectral cameras developed and manufactured by Spectral Imaging Ltd., Finland. It consists of the Spectral Camera HS with a wavelength range of 394 – 1008 nm, and the Spectral Camera SWIR with a wavelength region of 896 – 2504 nm. The VNIR sensor has a sensitive high speed interlaced CCD detector with 1600 pixels, 840 bands, a spectral resolution of 2.8 nm, and band intervals of 0.7 nm (http://www.specim.fi/files/pdf/core/datasheets/HS_Spectral_Camera-v3-11.pdf). The SWIR sensor has a cooled, temperature stabilized MCT detector with 320 pixels, 256 bands, a spectral resolution of 10 nm, and band intervals of 6.3 nm (http://www.specim.fi/files/pdf/core/datasheets/SWIR_SpeCam_ver1-14.pdf). These two spectrometers could be mounted onto a tripod, and a motor on the tripod can rotate so the spectrometers could scan an outcrop with vertical relief.

The Specim data was acquired in the field on October 18, 2013. In order to increase signal and reduce file size, horizontal and vertical binning of two times was applied to the VNIR images during data acquisition as recommended by the manufacturer. This setting doubled the band interval to 1.4 nm while this value is still smaller than the spectral resolution (2.8 nm), so the spectral differentiation ability of the VNIR sensor was not sacrificed. Pan speed of each scan was set so that each pixel covers identical distance in both the horizontal and vertical dimensions to minimize spatial distortion. Exposure time of each image was set to maximize signal while the brightest pixel in image did not saturate.

5.2.3 Data Processing Techniques

Data processing involves the restoration, rectification, enhancement, and classification of the remotely sensed digital images (Lillesand et al., 2004). Image processing prepares remotely sensed photographs for information extraction. Restoration and rectification includes the rectification of geometric distortions, correction of atmospheric absorptions and topographic effects. Enhancement includes the color enhancement which improves visual interpretation through the manipulation of brightness, contrast, sharpness, etc.; as well as spectral transformation which removes spectral correlations between bands and redundancy in the data. Classification is the association of pixels in an image into several classes based on spectral similarity.

In this study, band ratios, principal component analysis, minimum noise fraction, and spectral angle mapper are used to extract spectral information from the data. Preprocessing is performed priori to prepare the images for these algorithms. All images are processed with ENVI 5.0.

5.2.3.1 Preprocessing

Remote sensing images downloaded from the USGS website (http://earthexplorer.usgs.gov) have been preprocessed by the data providers. The Landsat 8 image was processed to level 1 terrain corrected (L1T), which is radiometrically, geometrically, and topographically accurate (Roy et al., 2014). The ASTER data was processed to registered radiance at sensor (L1B), which is radiometrically corrected and geometrically co-registered (Abrams et al., 2002). The Hyperion data was processed to level 1Gst, which is radiometrically corrected and ortho-corrected using DEM (Simon, 2006). All these satellite images were subset for quicker processing.

Radiometric calibrations were performed on the multispectral images to convert the images into top of atmosphere (TOA) reflectance. For Landsat 8, the following formula was used:

$$\rho_\lambda = \frac{M_\rho Q_{Cal} + A_\rho}{\cos(\theta_{SZ})} = \frac{M_\rho Q_{Cal} + A_\rho}{\sin(\theta_{SE})}$$

Where ρ_λ is the TOA reflectance, M_ρ is the band-specific gain factor, A_ρ is the band-specific offset factor, Q_{Cal} is the quantized and calibrated standard product pixel DN value, θ_{SZ} is the sun zenith angle, and θ_{SE} is the sun elevation angle (http://landsat.usgs.gov/Landsat8_Using_Product.php).

For ASTER, the following formula was used:

$$\rho_\lambda = \frac{\pi L_\lambda d^2}{E_{Sun,\lambda}\cos(\theta_{SZ})} = \frac{\pi L_\lambda d^2}{E_{Sun,\lambda}\sin(\theta_{SE})}$$

Where L_λ is the spectral radiance at sensor, d is the earth-sun distance in astronomical units, and $E_{Sun,\ \lambda}$ is the mean solar spectral irradiance. L_λ comes with L1B band data, d could be read from a second order polynomial fit of data in Table 5-3, $E_{Sun,\ \lambda}$ could be read from Table 5-4. Calculation was performed using band math function.

Day of Year	Distance	Day of Year	Distance
1	0.98331	305	0.99253
15	0.98365	319	0.98916
32	0.98536	335	0.98608
46	0.98774	349	0.98426
60	0.99084	365	0.98333

Table 5-3, earth-sun distance in astronomical units, from (Irish, 2000)

Band Number	E_{Sun}
1	1845.99
2	1555.74
3	1119.47
4	231.25
5	79.81
6	74.99
7	68.66
8	59.74
9	56.92

Table 5-4, ASTER solar spectral irradiances (W·m-2·μm-1), redrawn after http://www.gis.slu.edu/RS/ASTER_Reflectance_Temperature_Calculation.php

The ASTER SWIR image has lower spatial resolution compared with the VNIR image and is hard to compare with the VNIR image, so it was pan-sharpened using ground control points into the same spatial solution with the VNIR image, and then layer stacked together with the VNIR image, resulting in a single image with 9 bands.

The Hyperion scene was rotated at a certain angle so the flight route of the satellite is vertical in the scene, and that the area with no data was cut out. Then the scene was calibrated using ENVI FLASSH, a first-principles atmospheric correction tool. Calibration parameters like sensor height, map coordinates, acquisition time, and sun elevation were read from metadata and filled in by hand. Eighty-seven uncalibrated bands and noisy bands were removed from the data.

The Specim SWIR images show a lot of stripes due to mal-function of detector arrays, they were processed using ENVI THOR de-striping tool, which calculates the mean of every n^{th} line,

and then normalizes each line to its respective mean of all bands, to reduce the effects of striping. Striping was not obvious in the VNIR images, so the de-striping processing was omitted in VNIR images preprocessing. DN values in the images were calibrated into reflectance using a manufacturer provided converting utility based on the following equation:

$$R = \frac{Sample - Dark}{White - Dark} \times \frac{Exposure_{White}}{Exposure_{Sample}}$$

The VNIR images were then rotated 90 degrees counter-clockwise, and the SWIR images were transposed, so all the images show correct orientation. Due to sensitivity differences in two half parts of VNIR images, the calibrated VNIR images were cut into halves, and processed separately in further steps.

5.2.3.2 Band Ratios

Band ratio is a useful technique to enhance spectral differences between bands and to reduce topographic and illumination effects (Gao, 2008). Calculating band ratio is simple: just specify a numerator band and a denominator band, then the resulting band has the spectral information we need.

There are a lot of applications of band ratios. The normalized difference vegetation index (NDVI), is calculated as:

$$NDVI = \frac{NIR - Red}{NIR + Red}.$$

NDVI enhances the strong difference in reflectance between near-infrared and red in spectra of vegetation. NDVI could be used to highlight vegetation, as NDVI close to -1 corresponds to water, NDVI close to 0 corresponds to rock, sand or snow, and positive NDVI corresponds to

vegetation. This study focuses on rock alterations and vegetation can act as interference. So NDVI was calculated for the ASTER and Specim datasets, and areas with NDVI higher than 0.25 were masked to rule out the influences of vegetation.

Band ratios could also be used to enhance rocks and minerals. Sultan et al. (1987) suggested the usage of following Landsat TM band ratios in mineral mapping:

(1) Increasing opaque minerals decrease TM Band 5 / Band 1;

(2) Band 5 / Band 7 emphasizes hydroxyl-bearing minerals content variations;

(3) (Bands 5 / Band 4) × (Band 3 / Band 4) emphasizes ferrous minerals variations.

Ninomiya (2003) formulated following mineral indices of ASTER data:

(1) OH bearing altered mineral index (OHI) = (Band 7 / Band 6) × (Band 4 / Band 6);

(2) Kaolinite index (KLI) = (Band 4 / Band 5) × (Band 8 / Band 6);

(3) Alunite index (ALI) = (Band 7 / Band 5) × (Band 7 / Band 8);

(4) Calcite index (CLI) = (Band 6 / Band 8) × (Band 9 / Band 8).

These band ratios are utilized in this study to enhance the spectral differences of various minerals, and map the rock alterations.

5.2.3.3 Principal Components Analysis

Principal Components Analysis (PCA) is a linear transformation algorithm to produce uncorrelated bands, to segregate noise components, and to reduce the dimensionality of datasets

(Richards, 1999). The resulting PC bands are uncorrelated, and the bands have decreasing proportions of data variances.

5.2.3.4 Minimum Noise Fraction

Minimum Noise Fraction (MNF) is a linear transformation algorithm used to determine the inherent dimensionality of image data and to segregate noise in the data (Green et al., 1988; Boardman and Kruse, 1994). This transformation consists of two rotations: to use the principal components of the noise covariance matrix to decorrelate and rescale the noise, and to use the principal components derived from the noise-whitened image to create components that contain weighted information about variance across all bands (Vermillion and Sader, 1999).

5.2.3.5 Spectral Angle Mapper

Spectral angle mapper (SAM) is a supervised classification algorithm which takes user defined spectral endmembers, and classifies each pixel in image based on spectral resemblance to endmembers (Lillesand et al., 2004). SAM treats spectra as vectors in an n-dimensional space whose dimensionality equals to the number of bands, and uses n-dimensional angles between the pixel and reference spectra as the norm to measure the spectral similarities (Kruse et al., 1993). This algorithm is insensitive to illumination and topographic effects. Endmember spectra could be extracted from ASCII files, spectral libraries, or regions of interest (ROIs) directly in the image.

5.3 Results

5.3.1. Landsat 8

In order to minimize the disturbance of vegetation, images taken in winter were preferred in this analysis. The Landsat 8 image was acquired on January 29th, 2014.

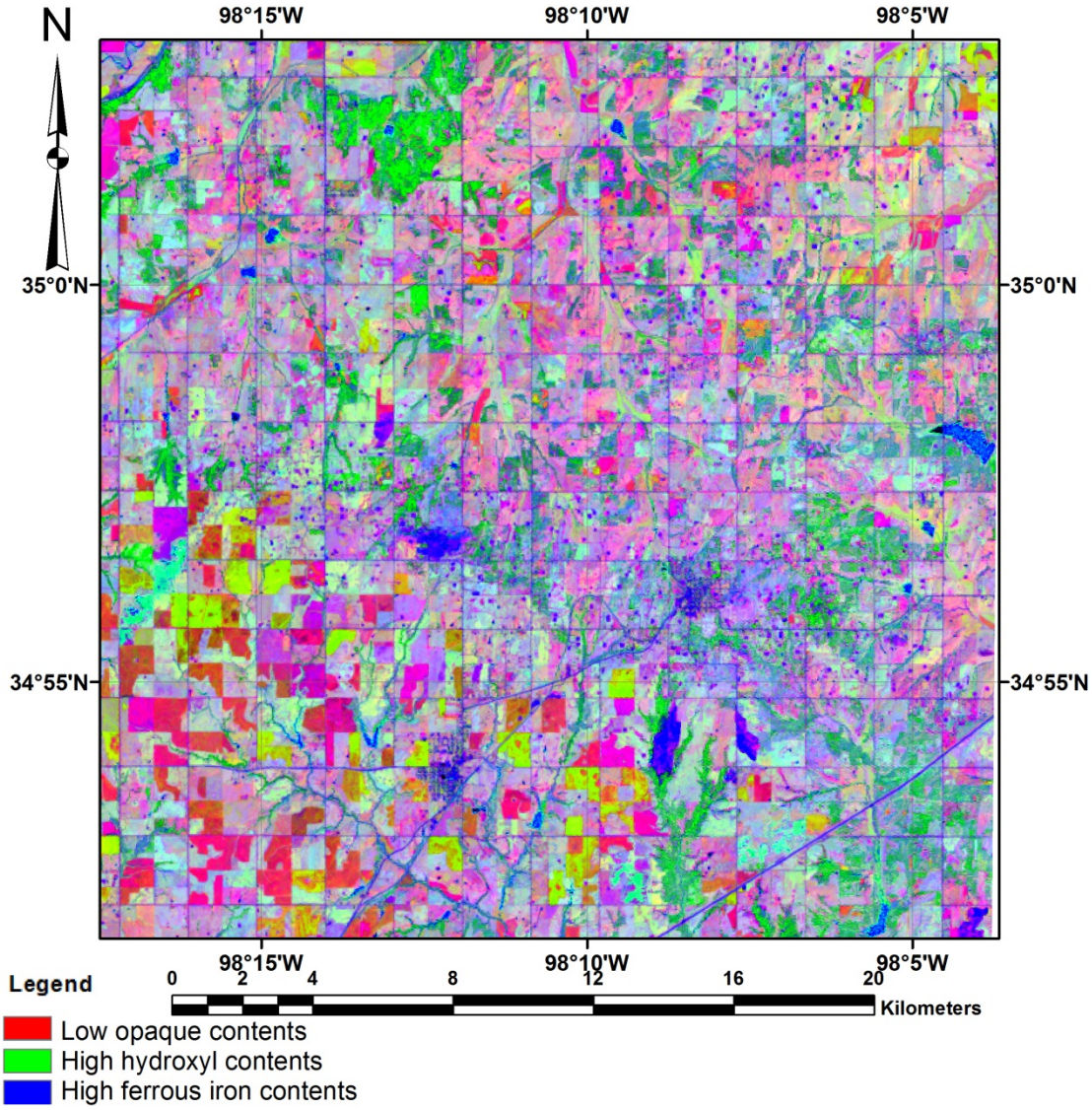

Figure 5-1, False color composite of Landsat 8 band ratios 6/2, 5/7, and 6/5 × 4/5. The red color represents low opaque content, the green color represents hydroxyl content, and the blue color represents ferrous iron content.

In Landsat 8 OLI data bands are assigned different numbers from Landsat TM and ETM+ data, so OLI band ratios 6/2, 5/7, and 6/5 × 4/5 are mostly equivalent to Sultan et al. (1987) type band ratios previous mentioned. False color composite (FCC) of these band ratios (Fig. 5-1) maps the alteration zone in greenish blue color. The alteration zone has low indices of opaque and hydroxyl contents, but a high index of ferrous iron.

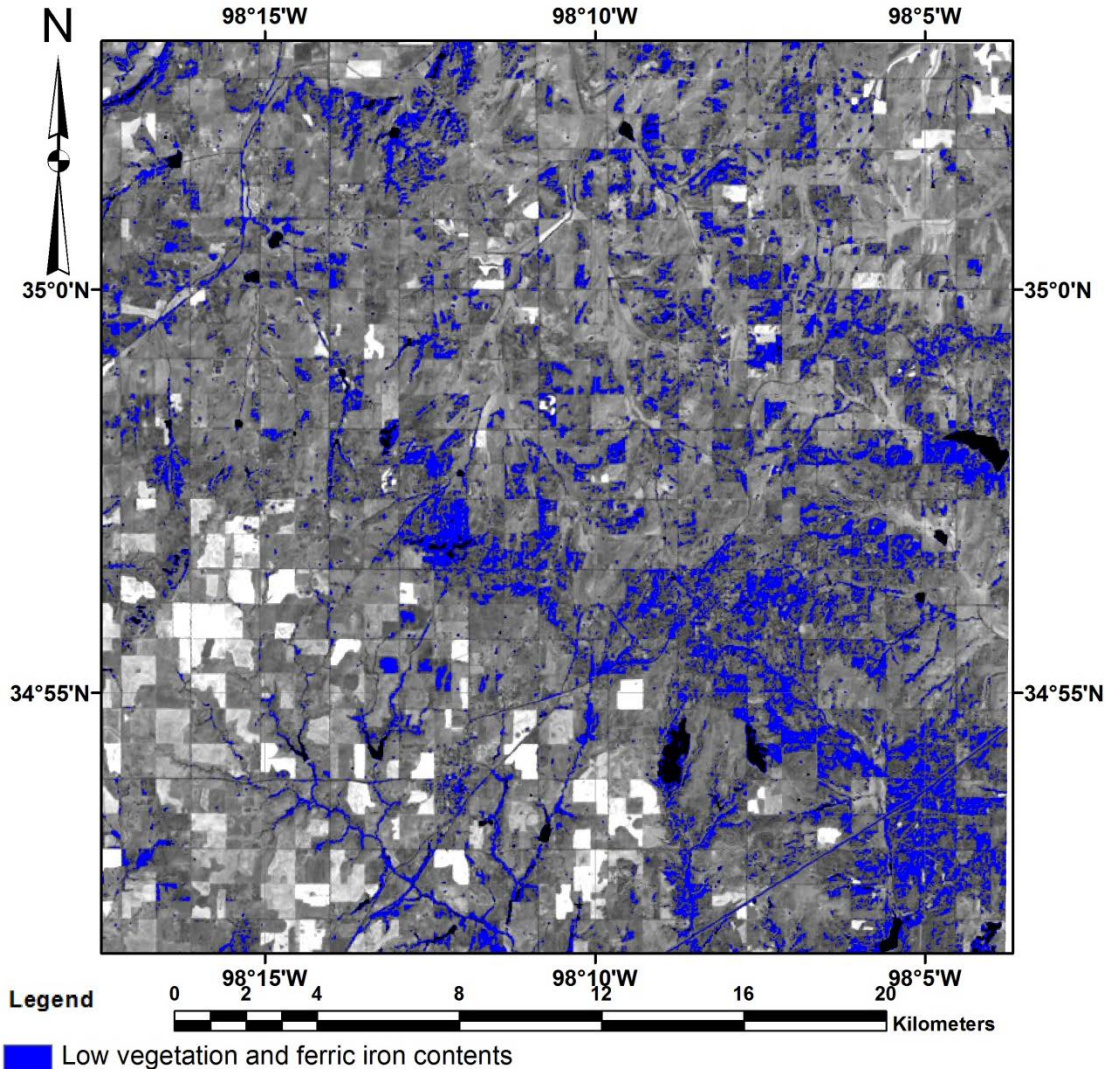

Figure 5-2, Map of Landsat 8 band ratio 5/2, highlighting materials with high reflectance in infrared and low reflectance in blue bands. Regions with a low band ratio value are shown in blue color, indicating lower content of vegetation and ferric iron.

Band ratio 5/2 highlights materials with high reflectance in near-infrared and low reflectance in blue bands; Fig. 5-2 shows regions with low band ratio 5/2 values, indicating low vegetation and ferric iron contents. Band ratio 4/2 highlights materials with high reflectance in red and low reflectance in blue bands; Fig. 5-3 shows regions with low band ratio 4/2 values, indicating low ferric iron content. The two images intersect mostly in the center to the southeast part of the scene.

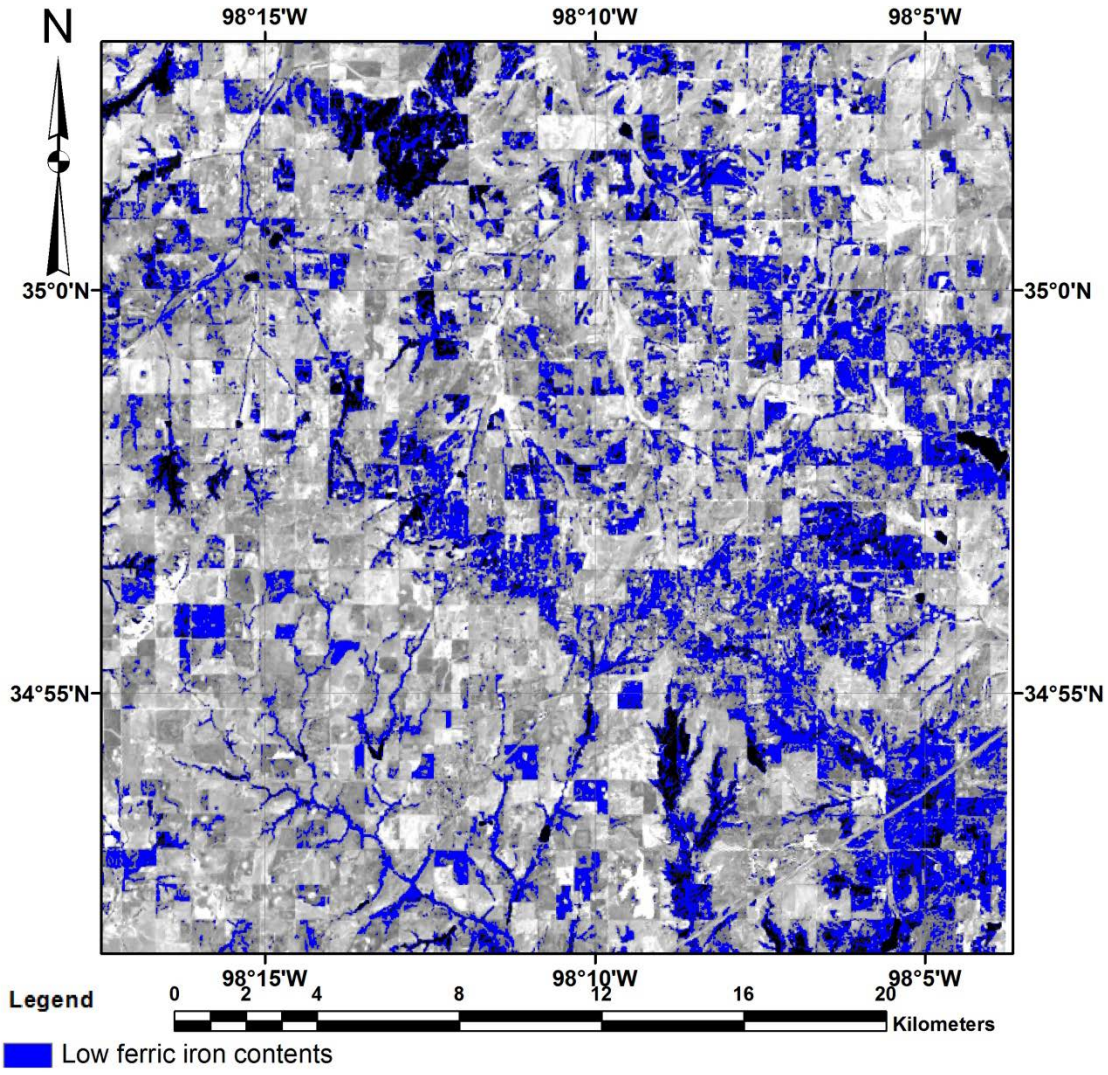

Figure 5-3, Map of Landsat 8 band ratio 4/2, highlighting materials with high reflectance in red and low reflectance in blue bands. Regions with a low band ratio value are shown in blue color, indicating lower content of ferric iron.

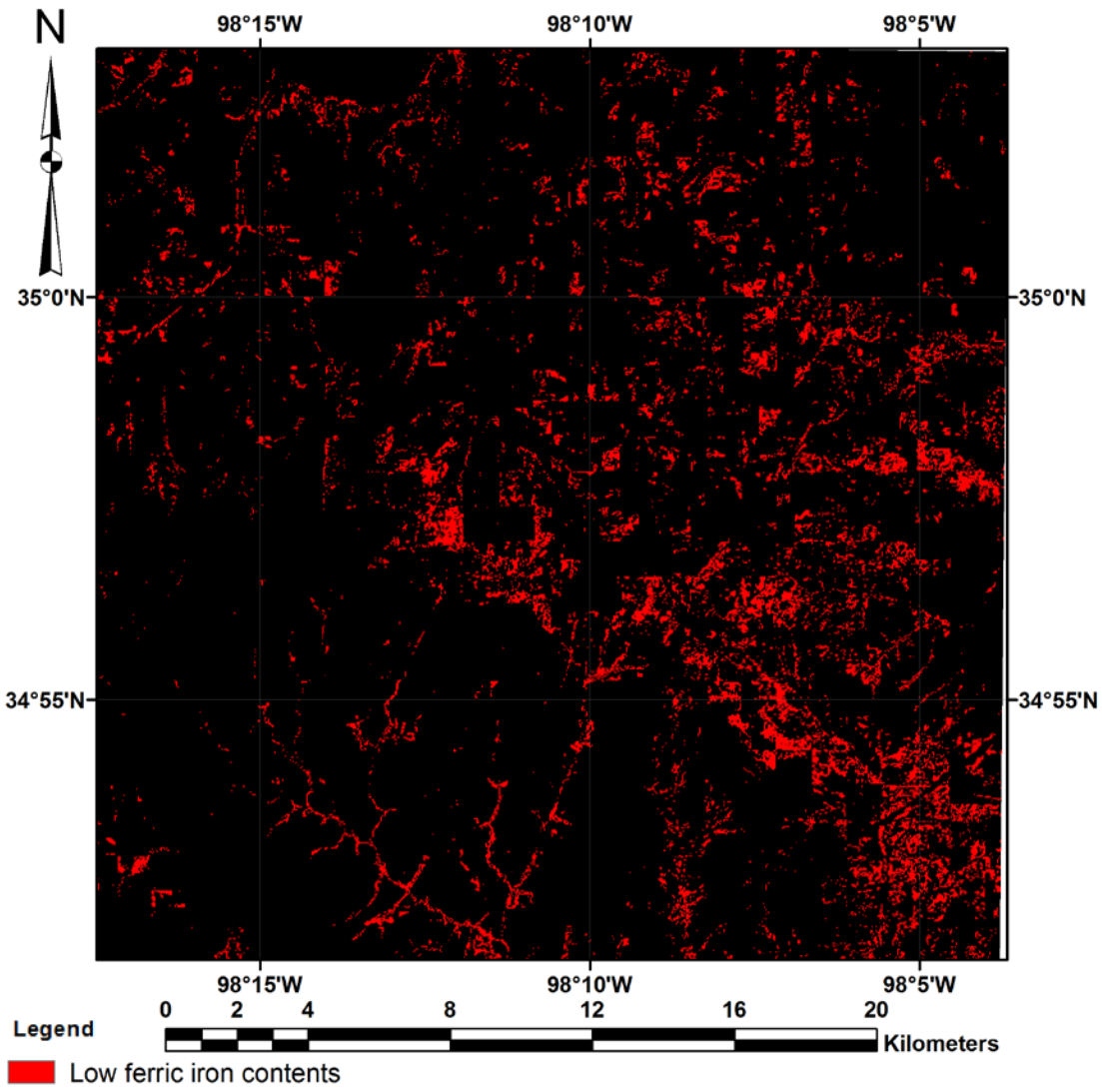

Figure 5-4, Combination of Landsat 8 band ratios 5/2 and 4/2, highlighting areas with low 5/2 and 4/2 band ratios, hence indicating alteration sites with low ferric iron content.

5.3.2 ASTER

Because of the anomalous high SWIR detector temperature, SWIR images after April 2008 are not available. The ASTER image used in this study was acquired on January 3rd, 2003.

Band ratios are calculated as suggested by Ninomiya (2003). Bands 5 – 9 are averaged to generate a "pseudo OLI Band 7", and then band ratios indicating ferrous iron minerals and hydroxyl-bearing minerals like the ones used in Landsat 8 image processing are calculated. False color composite (FCC) of OHI, KLI, ALI (Fig. 5-5) maps the alteration zone in dark brownish red color, which is a combination of relative low OHI, low KLI, and low ALI, compared with surrounding areas; while FCC of CLI, ferrous minerals index, hydroxyl minerals index (Fig. 5-6) maps the alteration zone in orange to red color, which is a combination of relatively high CLI, mid to high ferrous content, and low hydroxyl content. The CLI image (Fig. 5-7) maps areas with high carbonate content, as ASTER band 8 collects radiance in 2.295 – 2.365 μm, and cannot differentiate calcite versus dolomite. Previous petrographic studies show that both calcite and dolomite perform as inter-granular cement in the altered sandstones, thus a high CLI can be an indication of the alteration sites.

As ASTER has near-hyperspectral spectral resolution in the 2.14 – 2.43 μm range, Spectral Angle Mapper (SAM) classification was performed on ASTER bands 5-9. Endmembers spectra resampled to ASTER resolution are shown in Fig. 5-8. Most pixels are not classified, because the spectral angles are not small enough, but the reciprocals of the rule images can show the similarities. Fig. 5-9 shows the reciprocal band of calcite, areas with high resemblance are shown in red. This area is very similar to the alteration site mapped in Fig. 5-5 and 5-6. FCC of reciprocal bands of calcite, dolomite, and sandstone-unaltered-1 (Fig. 5-10) maps the alteration

site in bright yellow; while FCC of reciprocal bands of calcite, CF1-4-14, and CF9-2-70 (Fig. 5-11) maps the alteration site in whitish red.

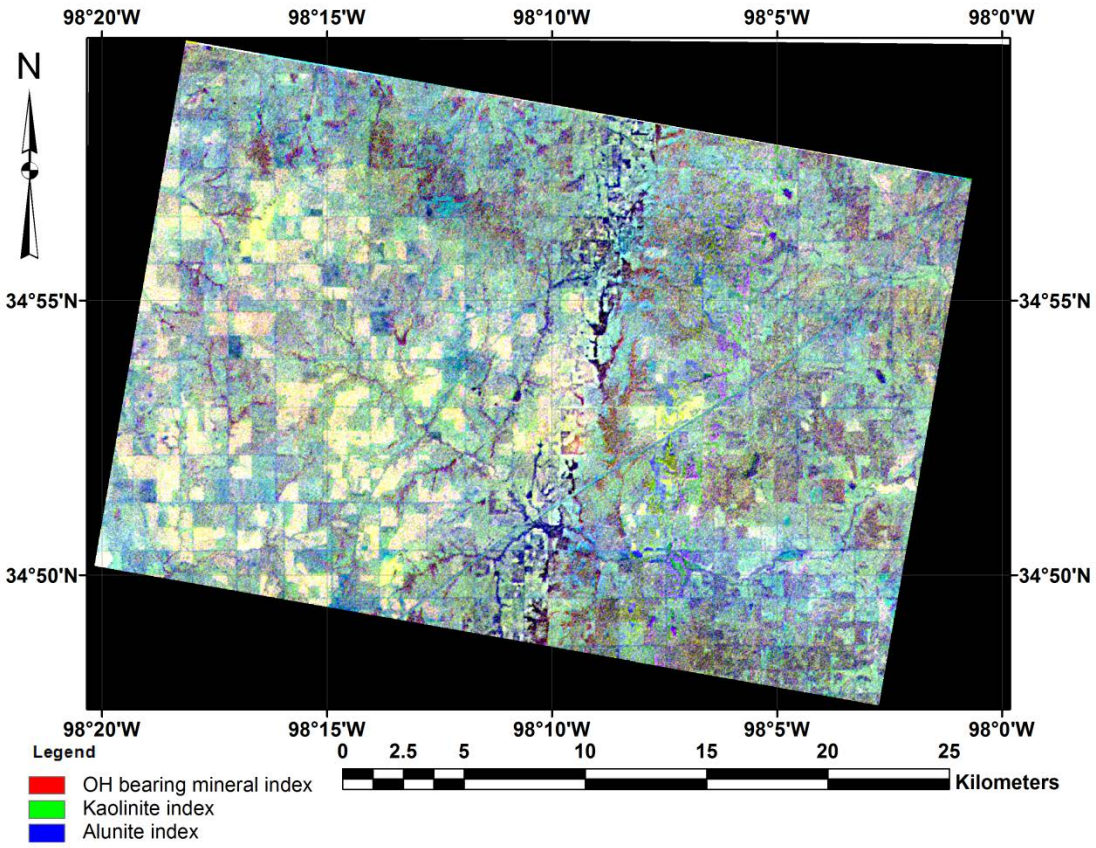

Figure 5-5, False color composite of ASTER band ratios OHI, KLI, and ALI. The red color represents OH bearing mineral contents, the green color represents kaolinite contents, and the blue color represents alunite contents. The alteration sites are mapped with dark brownish red.

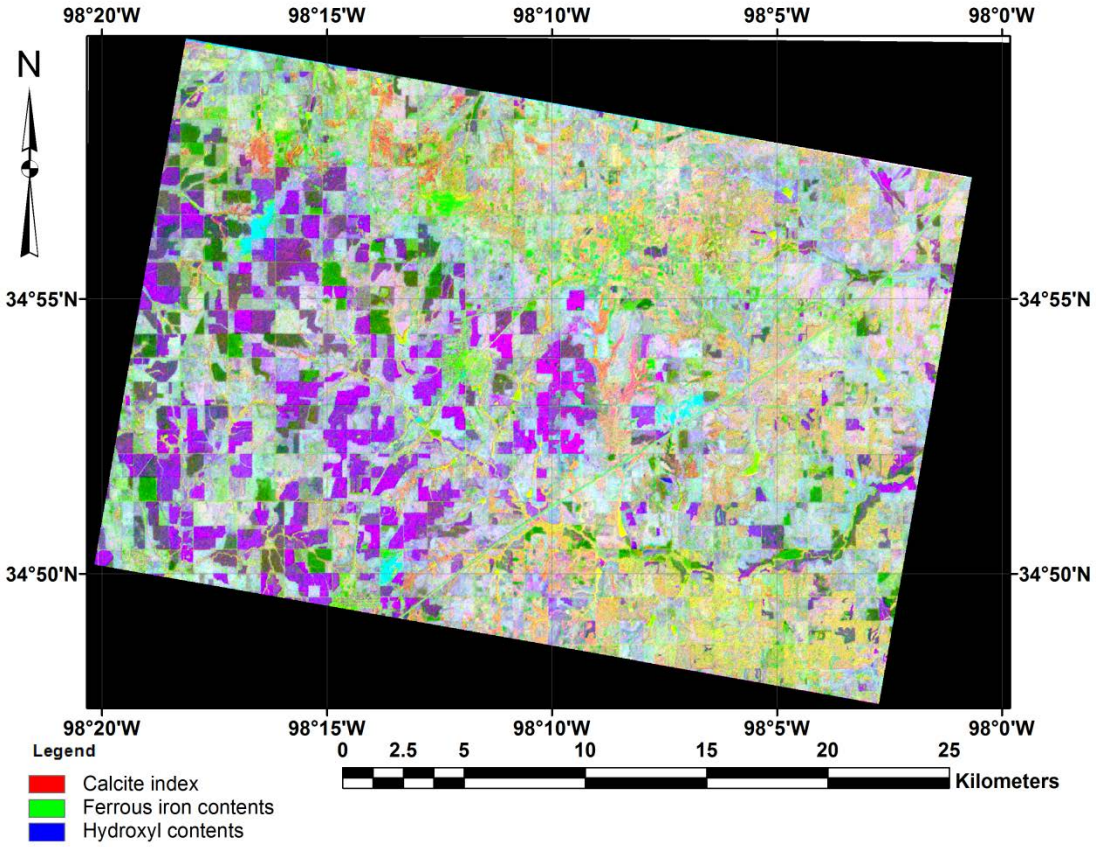

Figure 5-6, False color composite of ASTER band ratios CLI, FI, and HI. The red color represents calcite contents, the green color represents ferrous iron contents, and the blue color represents hydroxyl contents. The alteration sites are mapped with orange to red color.

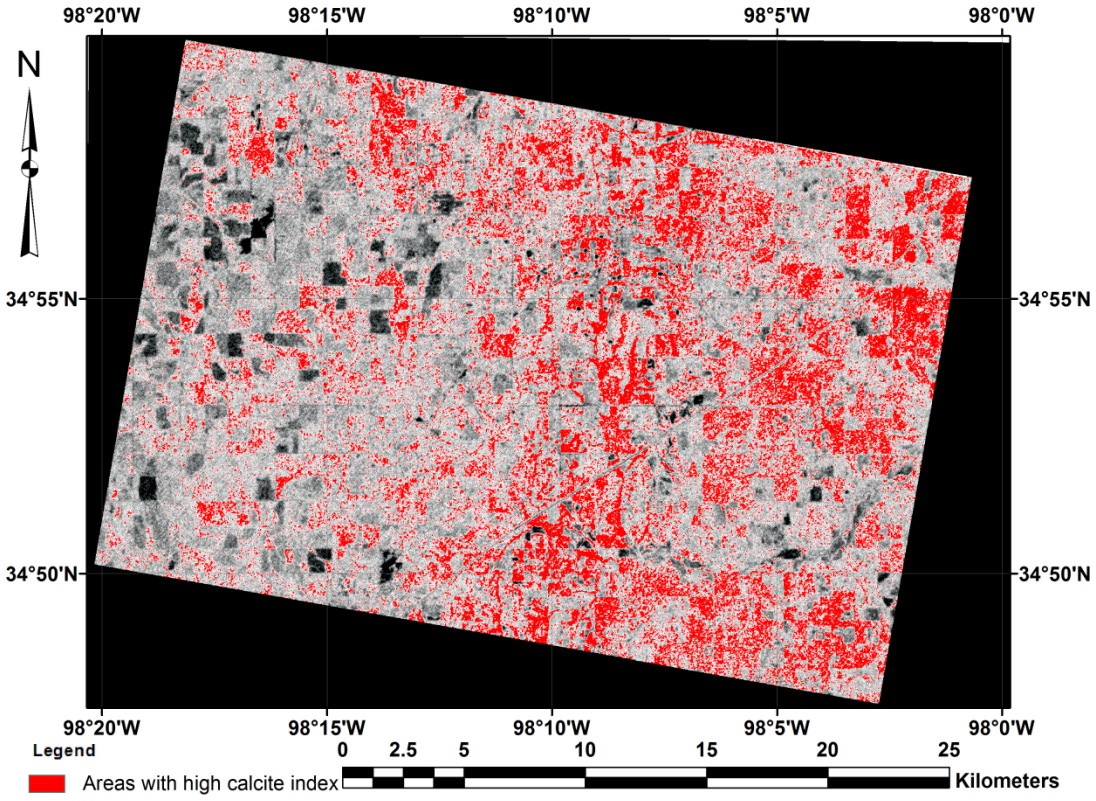

Figure 5-7, ASTER Calcite index band ratio image, areas of high carbonate content are mapped in red.

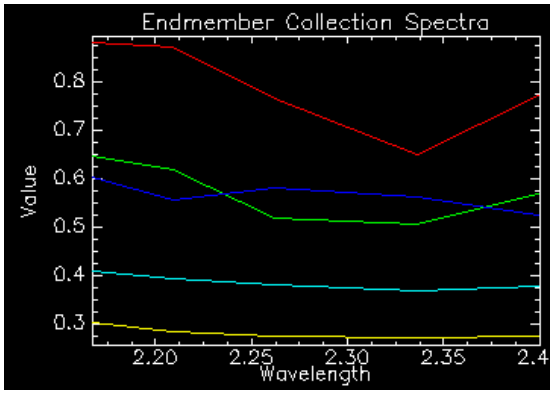

Figure 5-8, Endmembers spectra used in SAM classification. Red shows calcite, green shows dolomite, blue shows sample sandstone-unaltered-1, yellow shows sample CF-1-4-14, and cyan shows sample CF-9-2-70.

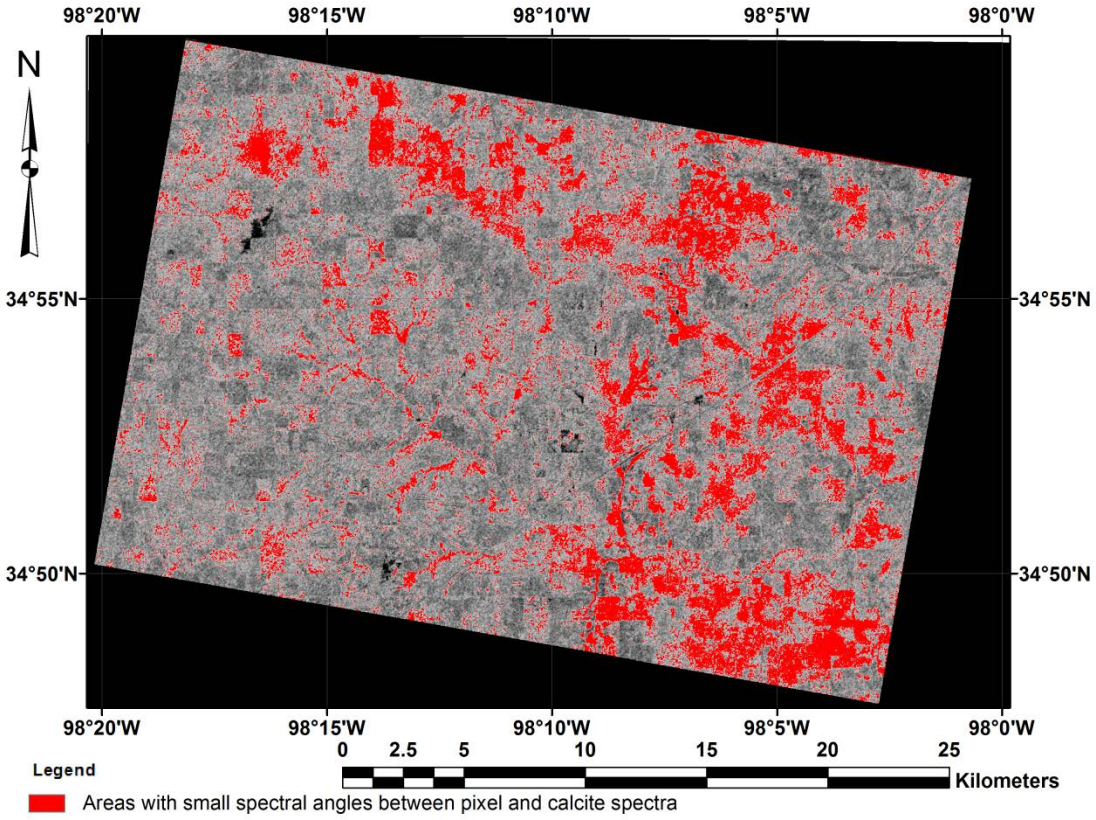

Figure 5-9, SAM reciprocal of calcite rule image, areas with high value are shown in red, indicating high calcite contents.

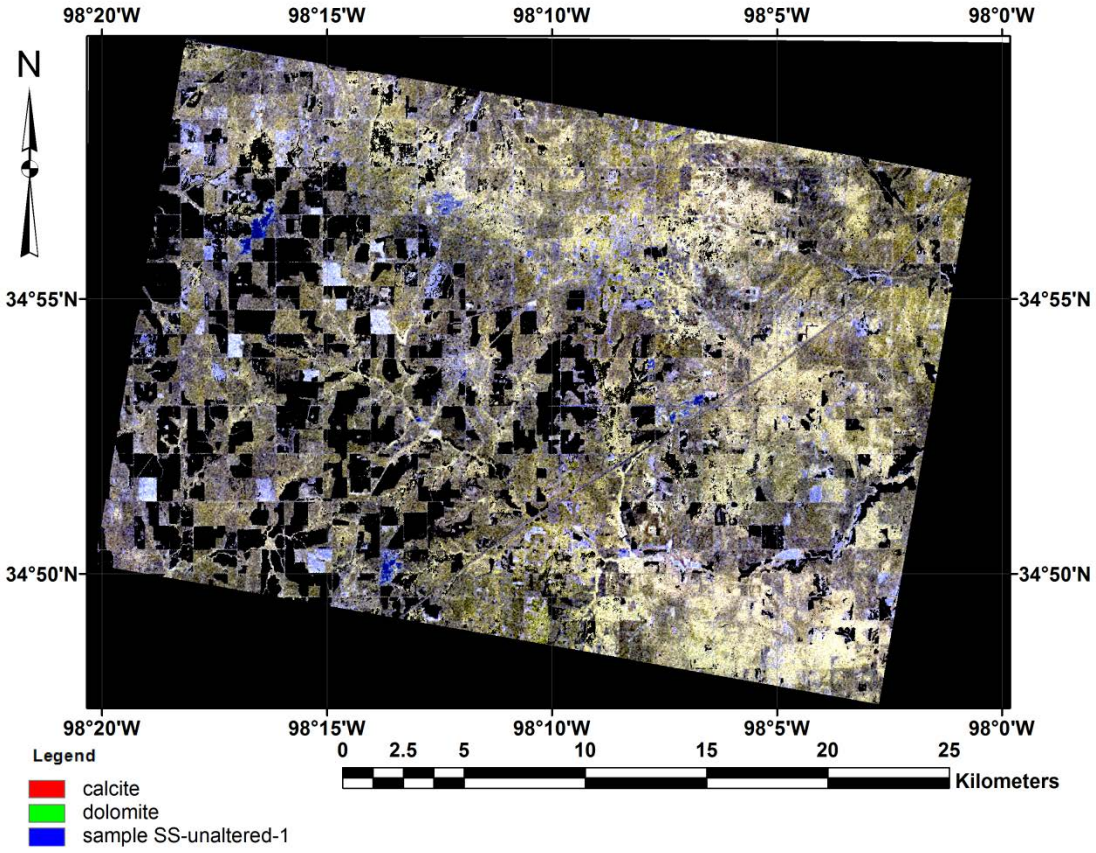

Figure 5-10, False color composite of reciprocal bands of calcite, dolomite, and sample sandstone-unaltered-1, the alteration sites are mapped in bright yellow.

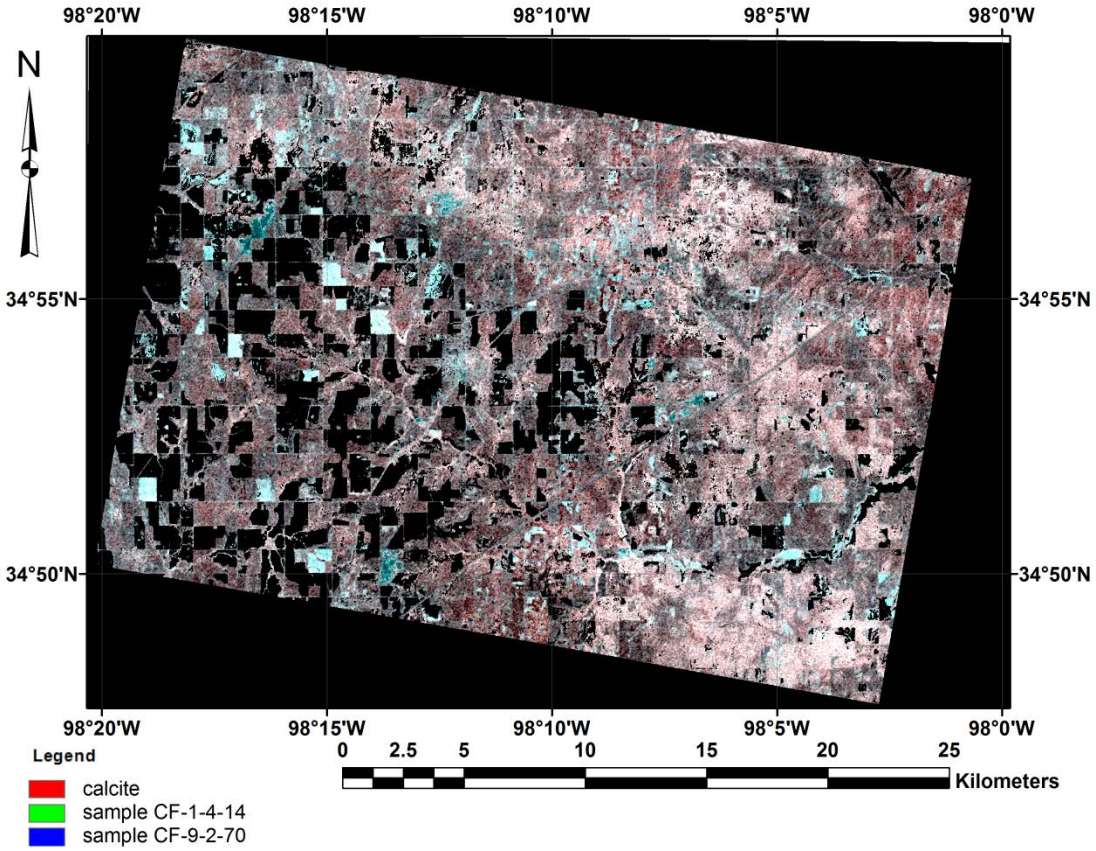

Figure 5-11, False color composite of SAM reciprocal bands of calcite, sample CF-1-4-14, and sample CF-9-2-70, the alteration sites are mapped in whitish red.

5.3.3 Hyperion

The Hyperion scene used in this study is the only image available on USGS website, and was acquired on October 21st, 2007. Only the eastern part of the study site is covered in the scene. Fig. 5-12 shows the 3D cube of the data, displaying spectral information of the edge pixels. Water absorptions could be identified at the blue gaps on the spectral dimension.

MNF rotation is performed on the reflectance image to segregate noise and show principal components in the data. Vertical stripes are obvious in the MNF image; red, magenta, green, and dark green colors represent different materials on the ground.

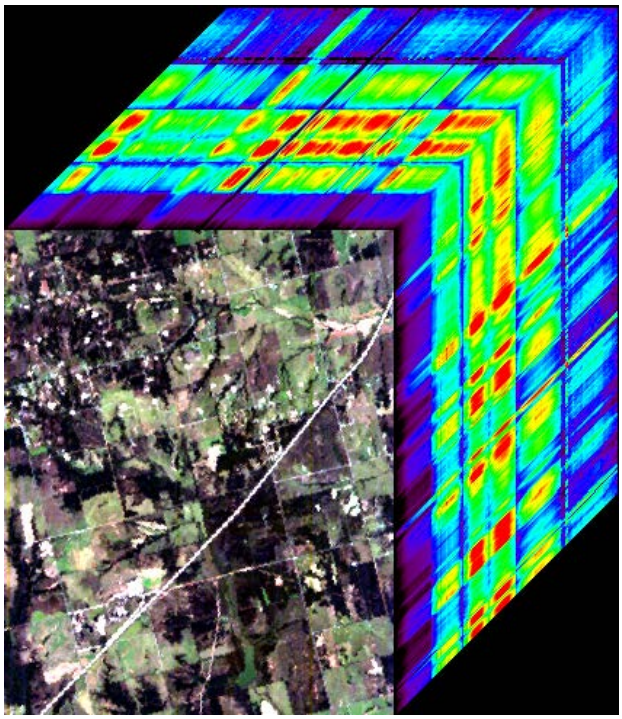

Figure 5-12, 3D cube of the Hyperion data.

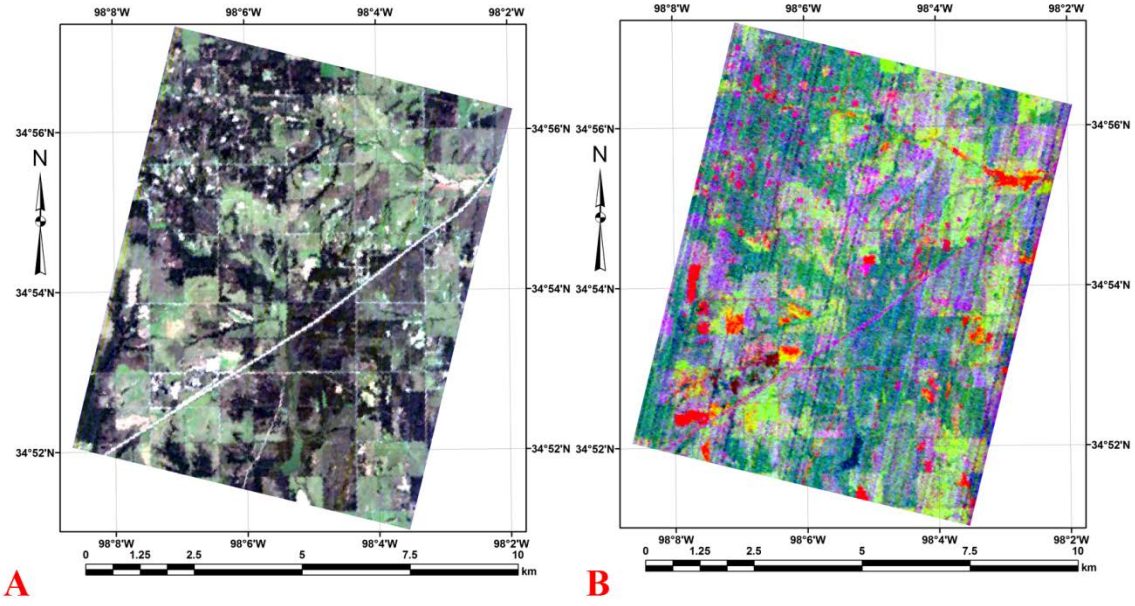

Figure 5-13, True color image (A) and the MNF result (B) of the Hyperion data. The MNF image shows vertical stripping, and different colors represent different materials on the ground.

Spectral angle mapper (SAM) technique is performed to classify the reflectance image. Endmembers are goethite from the USGS spectral library (Clark et al., 2007), and ASD spectra of field samples sandstone-unaltered-1, CF-1-4-14, and CF-9-2-70. As the spectral similarities are not high enough, the classification cannot classify most pixels in the image, but the rule images produced in the algorithm are the spectral angles between pixel spectrum and endmembers spectra. Thus the reciprocals of the rule images could represent the spectral similarities. Blue and green tones in Fig. 5-14 could represent similarities to sample CF-1-4-14, which is a representation of bleaching.

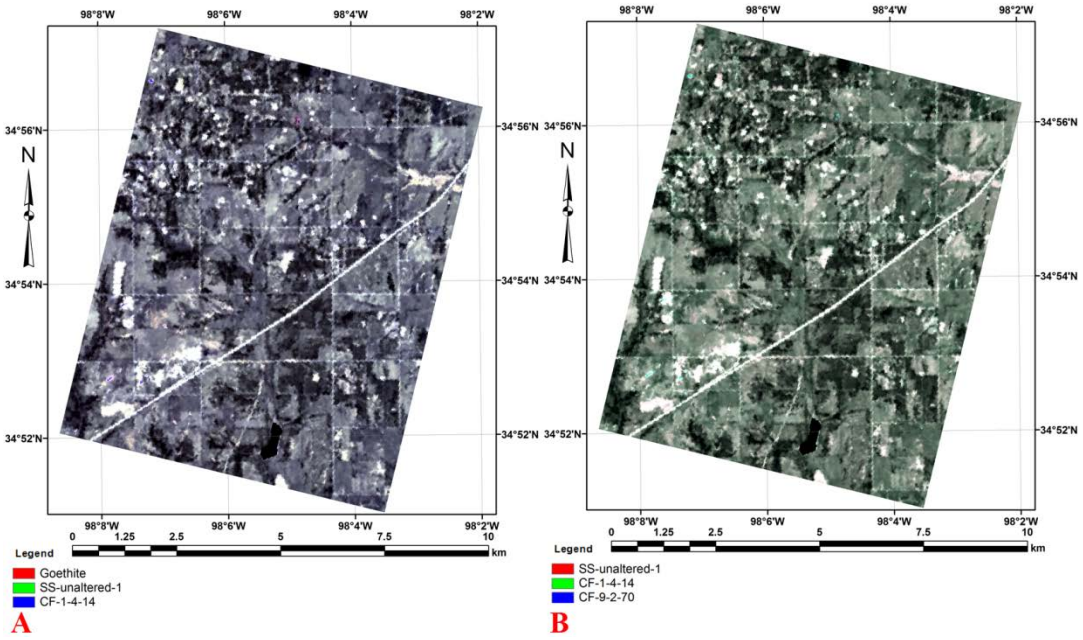

Figure 5-14, Two false color composites of SAM classification results of the Hyperion data. Red, green, and blue color in A) stand for endmembers goethite, sandstone-unaltered-1, and CF-1-4-14, respectively; red green, and blue in B) stand for endmembers sandstone-unaltered-1, CF-1-4-14, and CF-9-2-70, respectively. High values in the CF-1-4-14 band show blue tone in A) and green tone in B), with the absence of ferric iron. The spectral signatures of endmembers are shown in Figure 5-15.

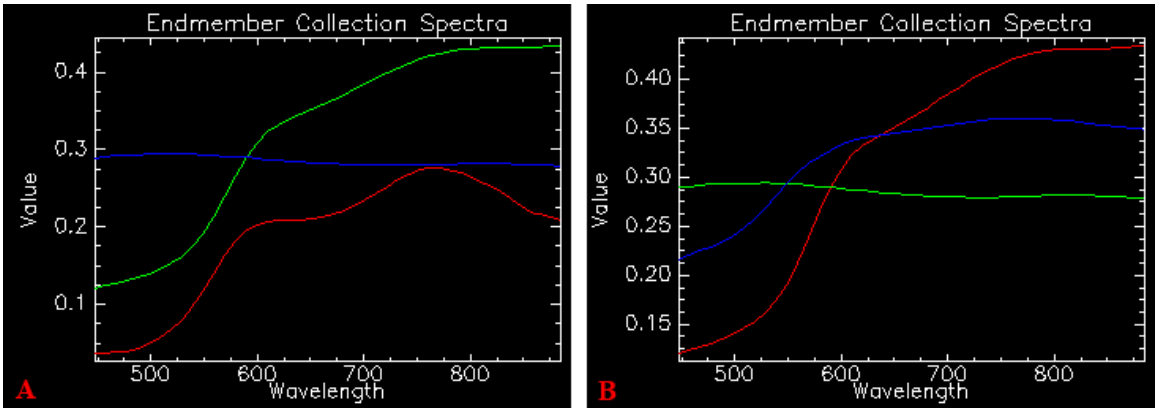

Figure 5-15, Spectral signatures of endmembers in SAM classification: A) goethite – red, sandstone-unaltered-1 – green, and sample CF-1-4-14 – blue; B) sandstone-unaltered-1 – red, CF-1-4-14 – green, and CF-9-2-70 – blue.

5.3.4 Specim

The field Specim data was acquired on October 18th, 2013. An outcrop of about 600 meters long and 30 meters high was scanned in two scenes. The outline of the outcrop is shown in Fig. 5-16. Because of a response difference between two spatial half parts of VNIR scans, the VNIR images are cut into two halves and processed separately. Fig. 5-17 shows the 3D cube of the lower part of the first scan, displaying spectral signatures of edge pixels in the VNIR range.

Spectral angle mapper (SAM) classification was performed on the hyperspectral images. As the image gets noisy in longer wavelengths in VNIR range with the signal to noise ratio very low, only bands 6 – 215, covering 400 – 700 nm spectral range, are used in the classification. The F_{900} absorption feature of ferric iron is not in this range, while F_{515} and F_{668} are. The classification could classify the image based mainly on these two small features of ferric iron. Endmembers are goethite from the USGS spectral library (Clark et al., 2007), and ASD spectra of field samples sandstone-unaltered-1, CF-1-4-14, and CF-9-2-70. Sample CF-1-4-14 is well bleached and the spectrum has no ferric iron absorption features. Fig. 5-18, 5-20, and 5-21 show false color

composites (FCC) of reciprocals of the rule images on the VNIR data, and the spectra of endmembers in these images are shown in Fig. 5-19. The sky, artificial buildings, and vegetation are masked in the images. Fig. 5-18 and 5-20 clearly shows that most of the scanned outcrop has been bleached of ferric iron, the left part and the top show more ferric iron. Fig. 5-21 shows that the left part of the second scan, which is the continuation on the right of the first scan, has been bleached of ferric iron, the right part has more ferric iron.

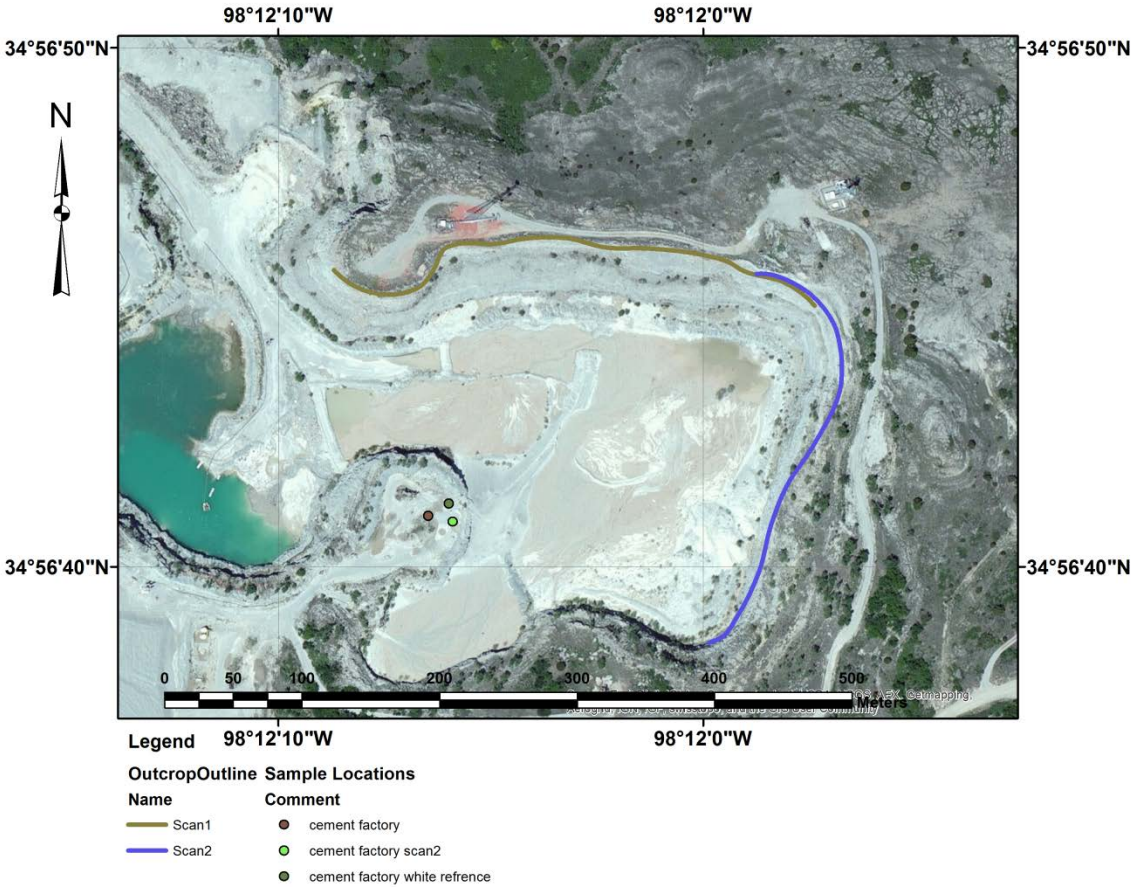

Figure 5-16, The outline of the scanned outcrop, the locations of cameras are also shown.

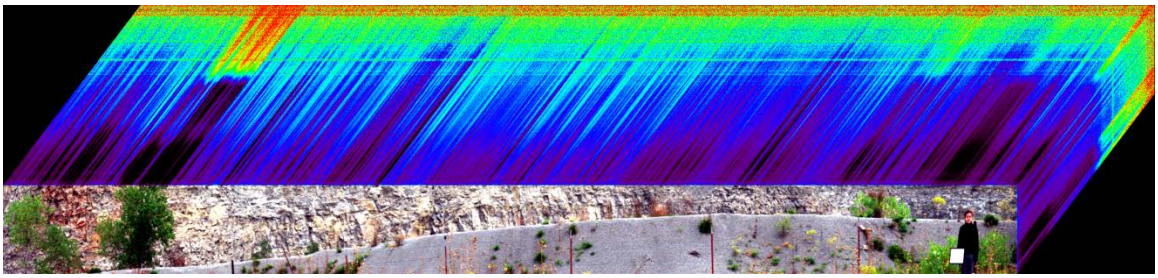

Figure 5-17, 3D cube of the lower half part of VNIR data of the scan1 in a mining quarry.

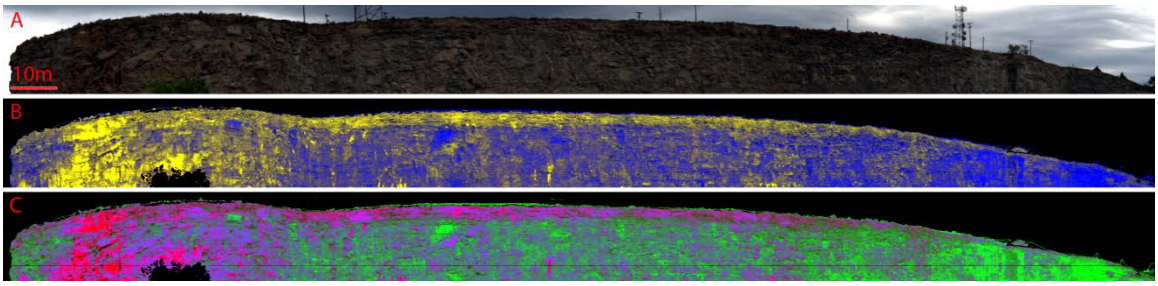

Figure 5-18, Two false color composites of SAM classification results of the upper part of the first VNIR scan shown in B) and C), the true color image is shown for comparison in A). Red, green, and blue in B) stand for endmembers goethite, sandstone-unaltered-1, and CF-1-4-14, respectively; red, green, and blue in C) stand for endmembers sandstone-unaltered-1, CF-1-4-14, and CF-9-2-70, respectively. High values in sandstone-unaltered-1, and CF-9-2-70 bands show yellow color in B) and red, magenta to violet in C), indicating the presence of ferric iron; high values of the CF-1-4-14 band show blue color in B) and green color in C), with the absence of ferric iron. The spectral signatures of endmembers are shown in Figure 5-19.

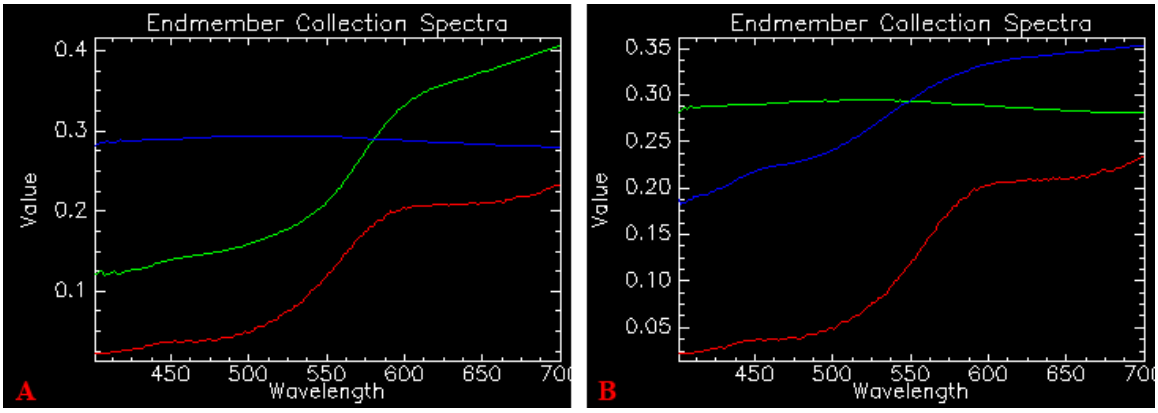

Figure 5-19, Spectral signatures of endmembers in SAM classifications: A) goethite – red, sandstone-unaltered-1 – green, and sample CF-1-4-14 – blue; B) sandstone-unaltered-1 – red, CF-1-4-14 – green, and CF-9-2-70 – blue. F_{515} and F_{668} could be seen on most spectra, but not on CF-1-4-14, indicating the presence of ferric iron in these endmembers but not in CF-1-4-14.

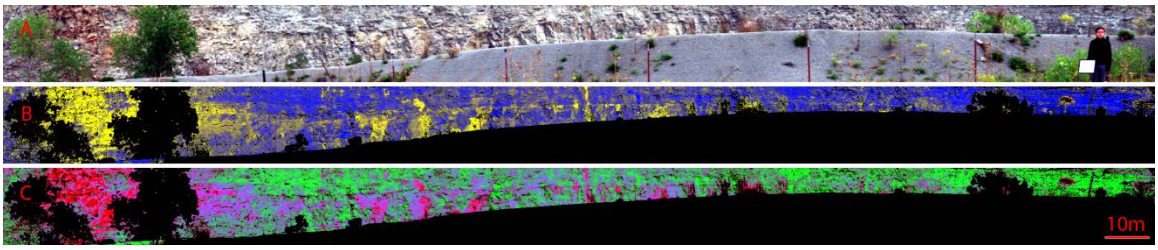

Figure 5-20, Two false color composites of SAM classification results of the lower part of the first VNIR scan shown in B) and C), the true color image is shown for comparison in A). Red, green, and blue in B) stand for endmembers goethite, sandstone-unaltered-1, and CF-1-4-14, respectively; red, green, and blue in C) stand for endmembers sandstone-unaltered-1, CF-1-4-14, and CF-9-2-70, respectively. High values in sandstone-unaltered-1, and CF-9-2-70 bands show yellow color in B), and red, magenta to violet in C), indicating the presence of ferric iron; high values of the CF-1-4-14 band show blue color in B) and green color in C), with the absence of ferric iron. The spectral signatures of endmembers are shown in Figure 5-19. Note that the scale does not apply to objects in the front but the outcrop rocks.

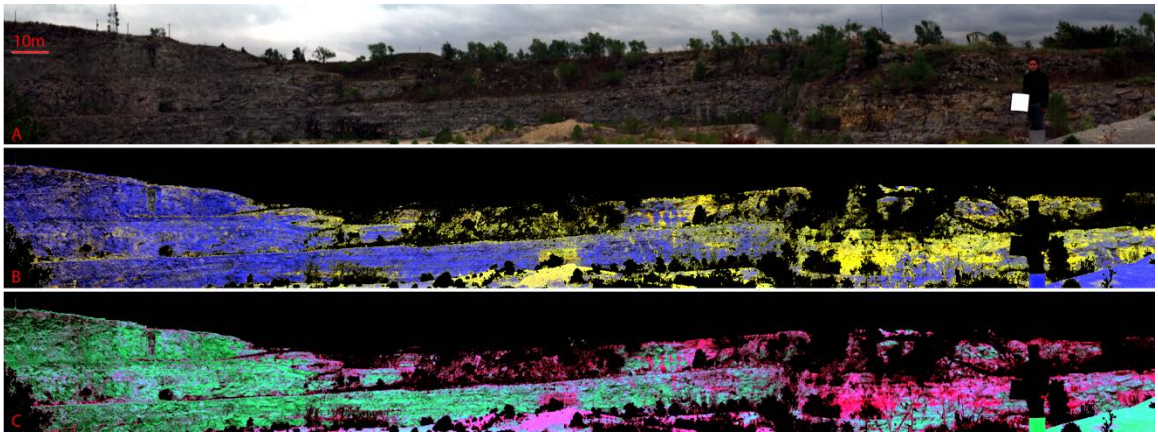

Figure 5-21, Two false color composites of SAM classification results of the upper part of the second VNIR scan shown in B) and C), the true color image is shown for comparison in A). Red, green, and blue in B) stand for endmembers goethite, sandstone-unaltered-1, and CF-1-4-14, respectively; red, green, and blue in C) stand for endmembers sandstone-unaltered-1, CF-1-4-14, and CF-9-2-70, respectively. High values in sandstone-unaltered-1, and CF-9-2-70 bands show yellow color in B) and red, magenta to violet in C), indicating the presence of ferric iron; high values of the CF-1-4-14 band show blue color in B) and green color in C), with the absence of ferric iron. The spectral signatures of endmembers are shown in Figure 5-19. Note that the scale does not apply to objects in the front but the outcrop rocks.

The SWIR images have some problems and are challenging to interpret. The first problem is noise in the data. In the first scan, bands with wavelength longer than 1800 nm are very noisy, only the outline of the outcrop, with a little bit of detail, could be identified. All the bands have some horizontal strips with lower values compared to adjacent lines; the spectral differences between strips are more prominent than the spectral differences between different materials. In the second scan, any band beyond 1800 nm is pure noise.

Minimum noise fraction (MNF) transformation was performed on the first 45 bands covering 896 – 1176 nm in SWIR data of the first scan. The resulting bands (Fig. 5-22, A) can successfully distinguish vegetation from the outcrop and the gravel wall, but the difference in ferric iron on the

outcrop could not be seen. SAM classification (Fig. 5-22, B) was performed on the same bands; the endmembers are picked from the image according to the SAM results in the VNIR images. Vegetation is classified well, but the outcrop is not. The classification follows mostly the strips but not the ferric iron content. MNF transformation (Fig. 5-23, A) on the 66 bands beyond 1800 nm shows no spectral differences in the outcrop. SAM classification (Fig. 5-23, B)) performed on the 13 bands at 2303 – 2378 nm shows a similar result to MNF.

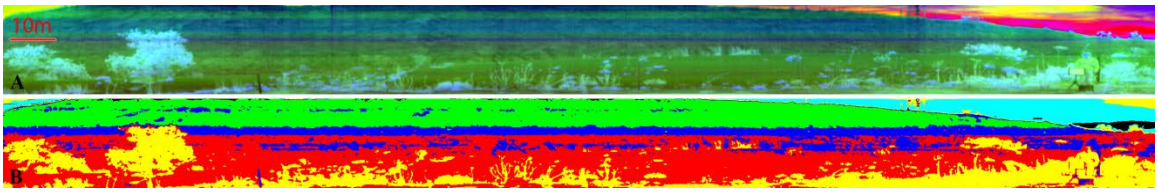

Figure 5-22, MNF (A) and SAM (B) results of bands 1 – 45 in SWIR data of the first scan. MNF could differentiate some materials but cannot see ferric iron variation on the outcrop. SAM follows mostly the lines. Note that the scale does not apply to objects in the front but the outcrop rocks.

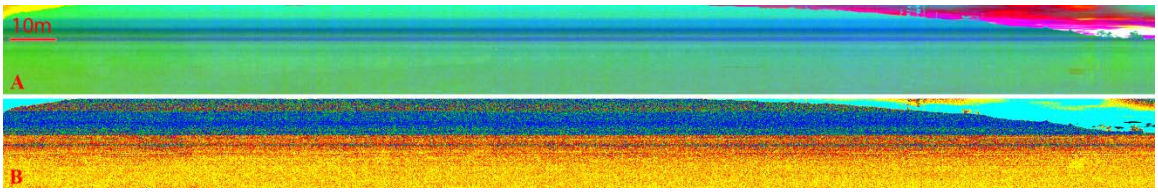

Figure 5-23, MNF results (A) of bands 171 – 236, and SAM results (B) of bands 224 – 236 in SWIR data of the first scan. Both MNF and SAM only show lines. Note that the scale does not apply to objects in the front but the outcrop rocks.

SAM classification is more successful in the second scan, although bands with wavelengths longer than 1800 nm are noisy and not used. The main reason for the success is that there are fewer bad lines in the second image than in the first one. Endmembers are selected from the image according to the classification results in the VNIR image. The results (Fig. 5-24) are also

similar to the classification results in the VNIR image: the left side is more bleached than the right side of the outcrop.

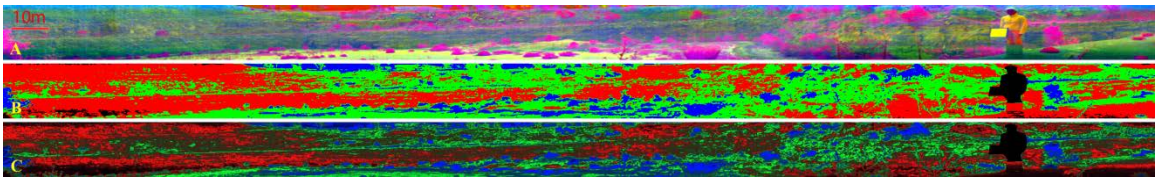

Figure 5-24, SAM classification results of bands 1 – 45 of SWIR data in the second scan. The direct classification result is shown in B, an FCC of reciprocals of rule images is shown in C, and an FCC of the first 3 bands in MNF transformation is shown in A for comparison.

Some small sections are cropped out from the images and processed separately; the reason for doing so is to circumvent the troubles caused by stripping. Principal components analysis (PCA) and MNF transformations are performed to highlight major spectral differences in these small sections. Fig. 5-25 and 5-26 show PCA and MNF transformations of two small sections in the VNIR data. Different colors in transformed images can represent changes in ferric iron contents. Fig. 5-27 shows PCA and MNF transformations of a small section in the SWIR data, stripping is prominent but some variation could be recognized in these images. Some areas in red to magenta colors represent higher ferric iron content compared to the surrounding rocks. Transformations on bands 224 – 236 cannot give more spectral information other than strips.

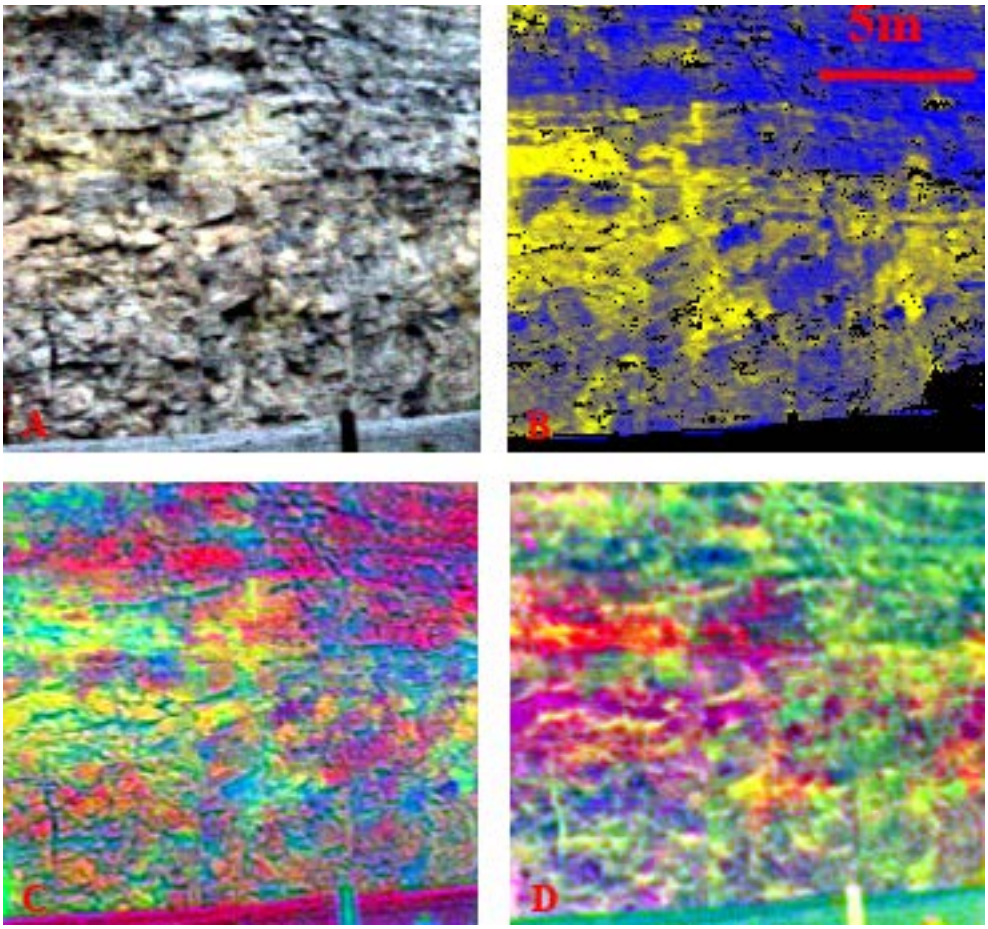

Figure 5-25, PCA (C) and MNF (D) transformations of a small section in the VNIR data of the first scan, true color image (A) and SAM classification image (B) are shown for comparison. Red to magenta color in the PCA image, as well as green color in the MNF image, represents low ferric iron contents; whereas yellow to cyan color in the PCA image, as well as red to magenta color in the MNF image, represents high ferric iron contents.

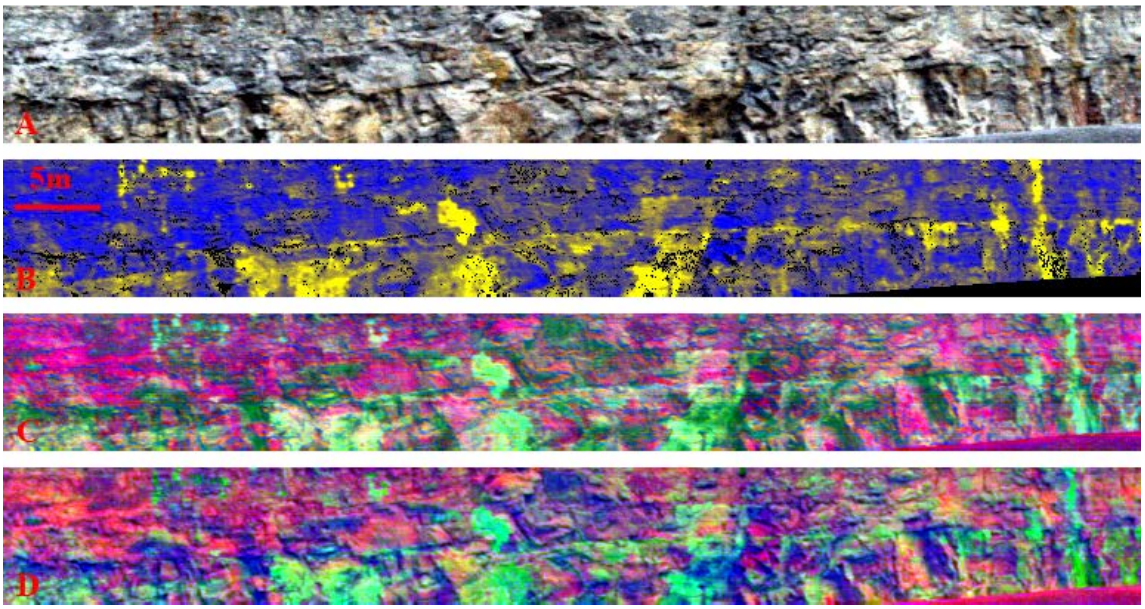

Figure 5-26, PCA (C) and MNF (D) transformations of a small section in the VNIR data of the first scan, true color image (A) and SAM classification image (B) are shown for comparison. Red to magenta color in the PCA and MNF images represent low ferric iron contents; whereas green to blue colors in both images represent high ferric iron contents.

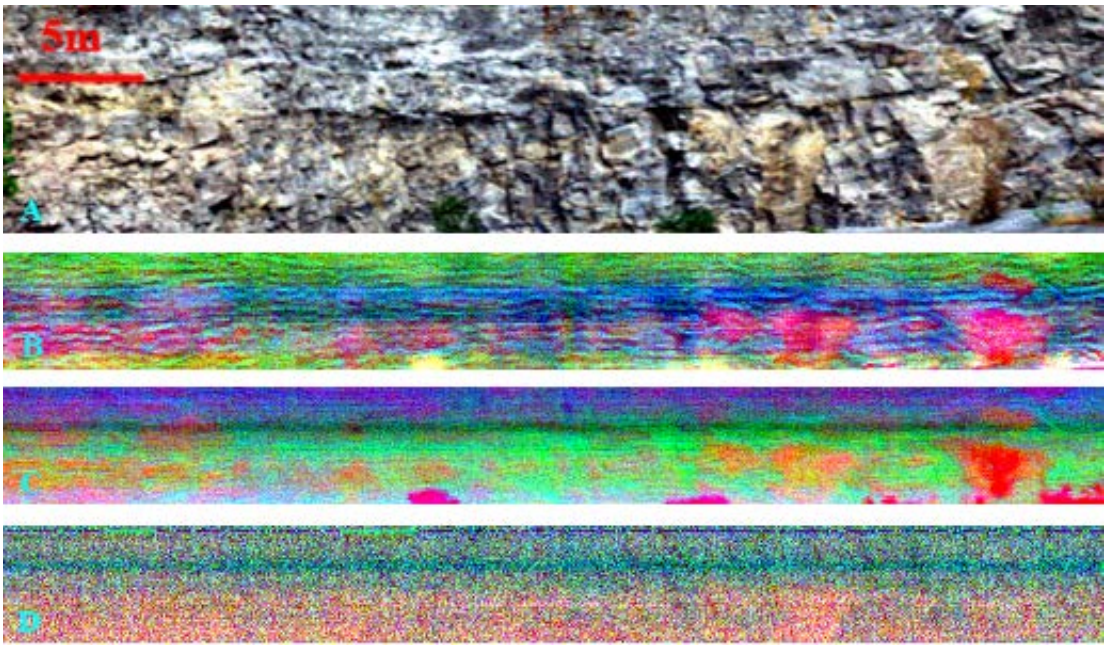

Figure 5-27, PCA (B) and MNF (C) transformations of bands 1 – 45, as well as PCA (D) transformation of bands 224 – 236 of a small section in the SWIR data of the first scan, a section of true color image of about the same area (A) is shown for comparison. Magenta to red color in both images represents high ferric iron contents.

Because the weather conditions during data acquisition were not optimum and the data was noisy, the field samples were scanned at close range with Specim cameras in the lab. The samples were illuminated with a tungsten light source. With lower moisture content in the air and the closer distance between the scanning cameras and objects, atmospheric absorption was minimized. Principal components analysis (PCA), minimum noise fraction (MNF) and spectral angle mapper (SAM) processing algorithms were performed on rotated and calibrated images, and the results are shown in Fig. 5-28 – 5-32. Different colors in the PCA and MNF images represent different mineral content, ferric iron content, as well as illumination conditions. Some pyrite grains could be identified on the alteration surface in Fig. 5-28. The endmembers used in SAM classification are identical to those used in outcrop scan classifications. As a result, the colors in classification

results have the same meanings to those in outcrop scan classifications. The yellow color on CF samples (Fig. 5-28, 29, and 30) represents high ferric iron contents, whereas blue color on CF samples represents low ferric iron content.

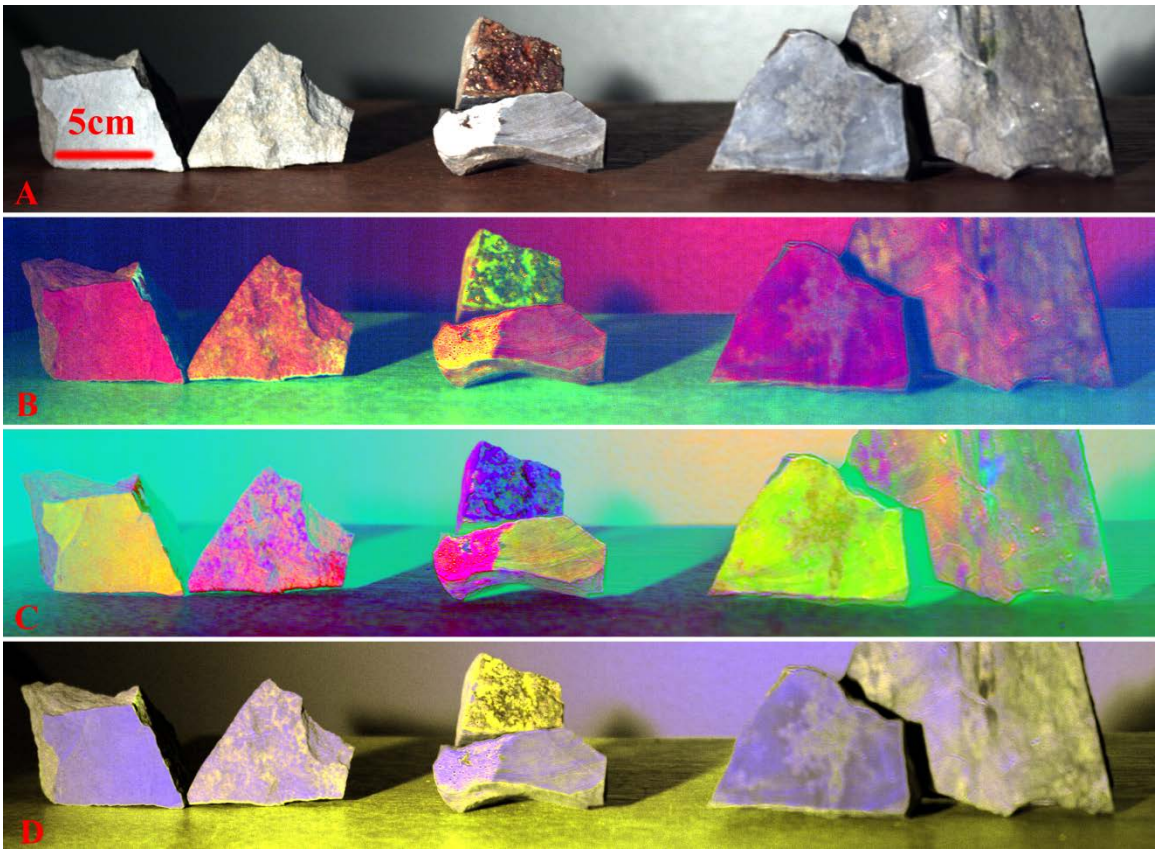

Figure 5-28, True color image (A), PCA (B), MNF (C), and SAM (D) results of scan-1 of the samples. Different colors in PCA and MNF images represent different mineral contents as well as illumination conditions. The endmembers used in the classification are: red – goethite, green – sample sandstone-unaltered-1, and blue – sample CF-1-4-14. The blue color on the samples shows more similarity to the bleached endmember CF-1-4-14, and the yellow color on the alteration surface indicates higher ferric iron content.

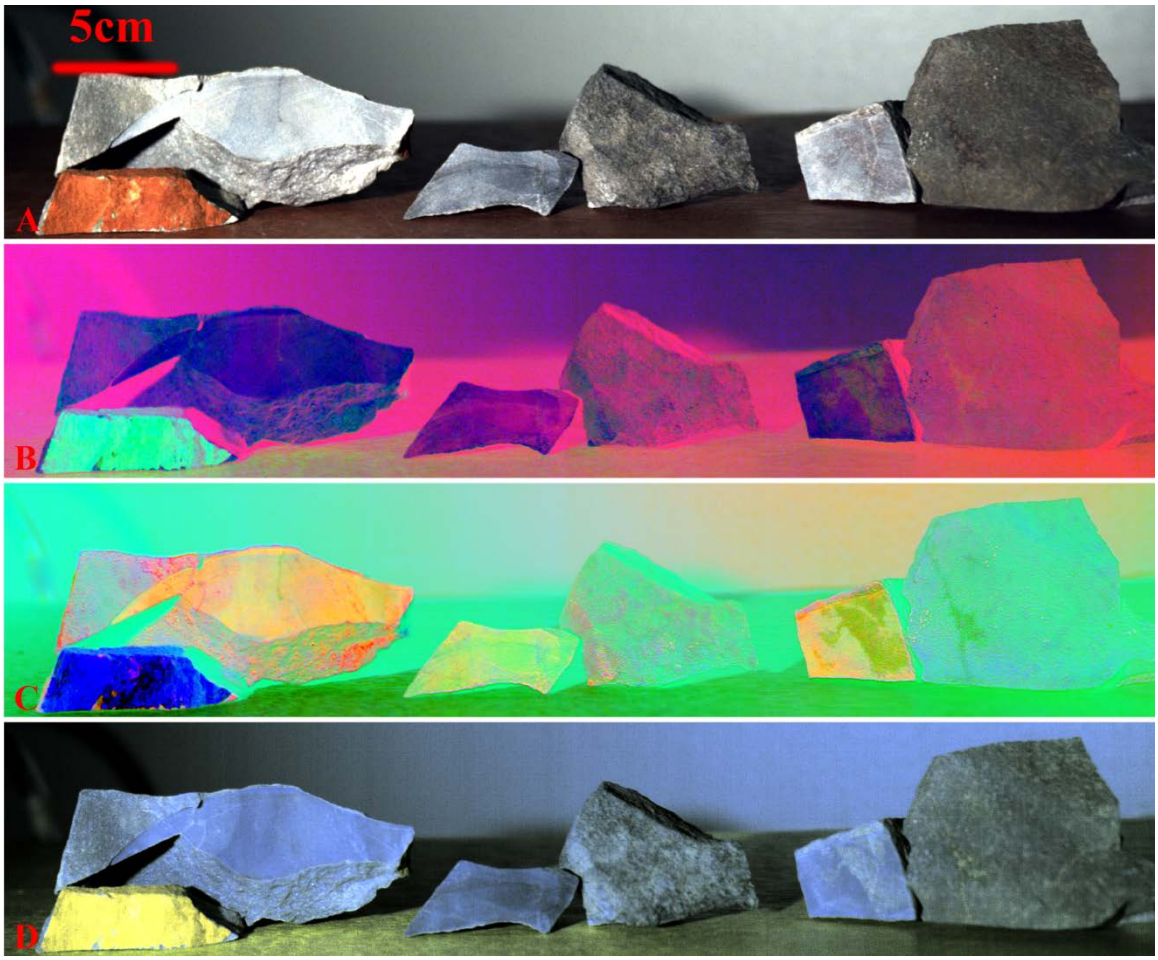

Figure 5-29, True color image (A), PCA (B), MNF (C), and SAM (D) results of scan-2 of the samples. Different colors in PCA and MNF images represent different mineral contents as well as illumination conditions. The endmembers used in the classification are: red – goethite, green – sample sandstone-unaltered-1, and blue – sample CF-1-4-14. The blue color on the samples shows more similarity to the bleached endmember CF-1-4-14, and the yellow color on the alteration surface indicates higher ferric iron content.

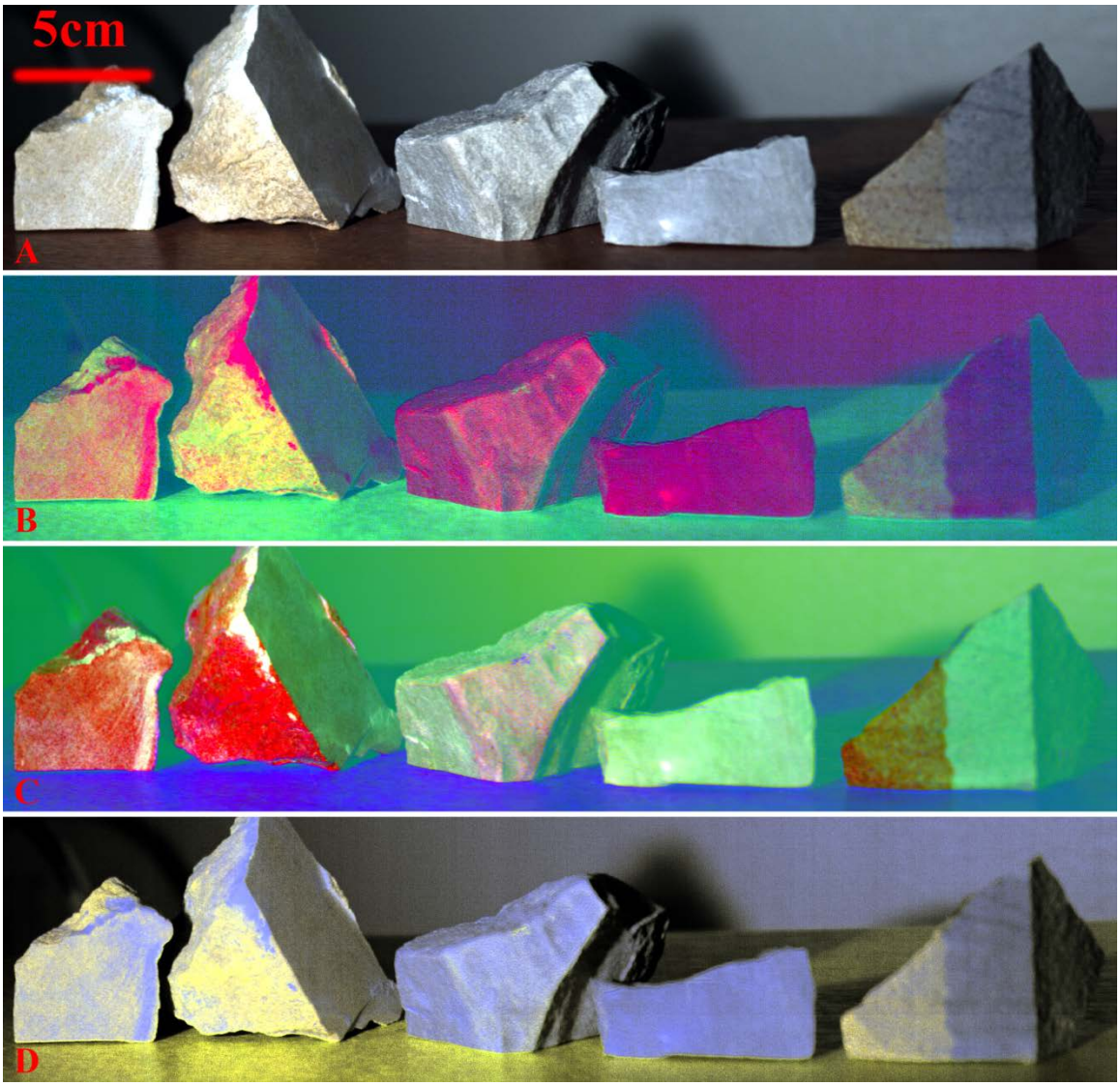

Figure 5-30, True color image (A), PCA (B), MNF (C), and SAM (D) results of scan-3 of the samples. Different colors in PCA and MNF images represent different ferric iron contents as well as illumination conditions. The endmembers used in the classification are: red – goethite, green – sample sandstone-unaltered-1, and blue – sample CF-1-4-14. The blue color on the samples shows more similarity to the bleached endmember CF-1-4-14, and the yellow color on the samples indicates higher ferric iron content.

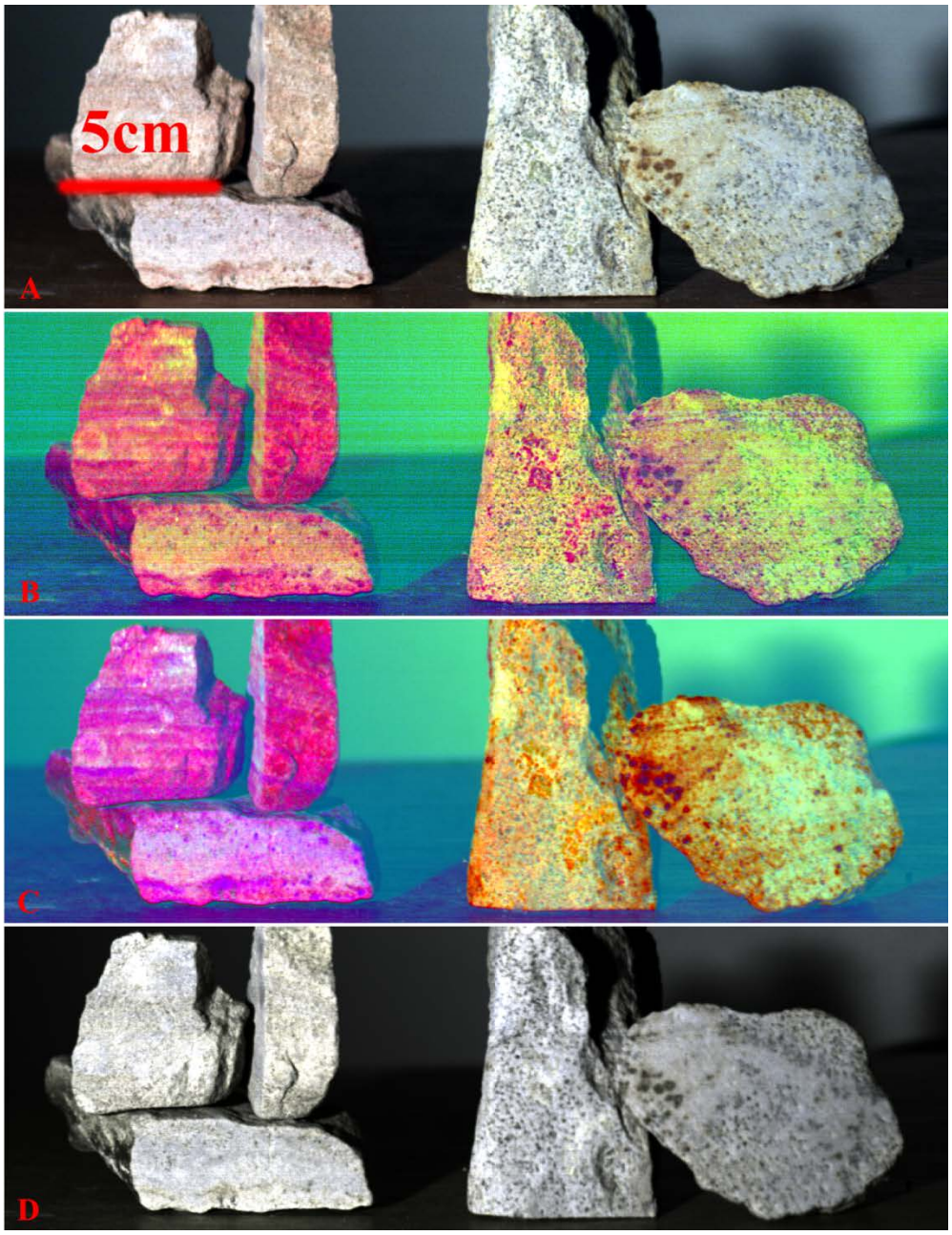

Figure 5-31, True color image (A), PCA (B), MNF (C), and SAM (D) results of scan-4 of the samples. Different colors in PCA and MNF images represent different ferric iron contents as well as illumination conditions. The endmembers used in the classification are: red – goethite, green – sample sandstone-unaltered-1, and blue – sample CF-1-4-14. The bluish color on the samples shows more similarity to the bleached endmember CF-1-4-14, and the yellowish color on the samples indicates higher ferric iron content.

Figure 5-32, True color image (A), PCA (B), MNF (C), and SAM (D) results of scan-5 of the samples. Different colors in PCA and MNF images represent different ferric iron contents as well as illumination conditions. The endmembers used in the classification are: red – goethite, green – sample sandstone-unaltered-1, and blue – sample CF-1-4-14. The dark color on the samples shows some surface alterations, and the cyan color represents some dents on the surface.

6. Discussion and Conclusions

6.1 Petrography

Petrographic analysis was performed to study the composition and texture of the samples collected in the field. The results show that: 1) unaltered sandstones are red, limonite / hematite coating is common, while altered sandstones are grey, yellow, white or a little bit of red in color, and coating is rare; 2) unaltered sandstones are soft, porous and easy to break, limited cementation of iron oxide coating and clay minerals could not fill the inter-granular space, while altered sandstones are hard, compact, very well cemented by carbonates; and 3) surface aggregation of pyrites confirmed the reduction of ferric iron, and secondary oxidation produced a thin rusty surface. The bleaching and cementation of the Rush Springs sandstones are significant alteration phenomena.

Crystallization gradient in the altered gypsum samples shows the effects of alteration. The closer to the crest of the anticline, the smaller crystal size they have. It is inferred that the Cyril Gypsum Formation may have undergone recrystallization related to hydrocarbon alteration. The abundance of hydrocarbons in the near-surface provides a premium environment for recrystallization. Further investigation including collection of more samples at more locations should be performed to confirm an actual relationship between the gypsum recrystallization and hydrocarbons; mineralogical and geochemical study should be performed to test if a causal relationship exists, and rule out other possible explanations of recrystallization.

6.2 Spectral Analysis

Spectral analysis was performed to provide laboratory references for data processing in remote sensing imagery. Important bands and spectral features are resolved from spectral analysis.

Analyzing ASD spectra of rock samples, the loss of ferric iron content in sandstone samples is confirmed by the presence of the shallower or none F_{900} trough. In unaltered sandstones there is no 2320 – 2340 nm features, indicating the absence of carbonate cementation, whereas spectra of all sandstones collected in the alteration zone show spectral signatures of carbonate cementation. The cementation by carbonates is also confirmed by the petrographic analysis. Surface alterations of iron minerals observed on hand samples are confirmed by deep F_{900} and relatively small F_{515} and F_{668} absorption troughs.

No carbonate absorption features could be identified in altered gypsum spectra, and there's no significant spectral difference between unaltered and altered gypsum samples. As a result, there is no way to differentiate unaltered from altered gypsum samples with remote sensing techniques. One possible solution is to find more gypsum samples with a higher degree of alteration, and identify the spectral differences between unaltered gypsum and altered gypsum samples.

Comparing with the ASD spectra, all bands in Specim VNIR imagery, and bands 1 – 45 (896 – 1176 nm) in Specim SWIR imagery, as well as bands 10 - 103 (447 – 1174 nm) in Hyperion imagery, can provide information about ferric iron in sandstones. Cementation of carbonates can be confirmed by absorption feature at 2320 – 2340 nm in ASD spectra, so bands 226 – 232 (2316 – 2353 nm) in Specim SWIR imagery, as well as bands 216 – 220 (2315 – 2355 nm) in Hyperion imagery, could be used to identify calcite.

6.3 Remote Sensing Imagery

The main focus of this study is to identify surface rock alterations induced by hydrocarbons. Multispectral and hyperspectral remote sensing imagery are used for this purpose. The major alteration phenomena in the Cement field are bleaching of ferric iron and cementation of carbonates in Rush Springs sandstones, as shown by petrographic analysis. Spectral signatures

related to these alterations are the presence or absence of ferric iron absorptions: F_{900}, F_{515}, and F_{668}, as well as the absorptions caused by carbonates at 2320 – 2340 nm. Alterations of the Cloud Chief Formation are not recognizable with spectral analysis.

Landsat 8 provides a blue band, so it is useful in identifying ferric iron which has low reflectance in blue bands. Analysis of band ratios mapped the alteration zones with low ferric iron contents in the Landsat 8 scene. ASTER data has no blue bands, but a near hyperspectral resolution in 2.14 – 2.43 μm, so it is useful in identifying carbonates, which have an absorption feature at 2320 – 2340 nm. Analysis of band ratios, as well as SAM classifications successfully mapped the alteration zones with high carbonate content in the ASTER scene. The combination of Landsat 8 and ASTER data (Fig. 6-1) shows the alteration sites with low ferric iron and high carbonate contents.

Hyperion data cover a very small section in the study site; SAM classifications compared spectral similarities between pixel spectra and endmembers, and mapped the alteration zones with low ferric iron contents. The bands in long wavelengths are noisy and full of strips; however, analysis of carbonates is not successful.

All the satellite data mentioned before have a spatial resolution of tens of meters, while Specim data provide high spatial resolution in outcrop scale as well as hand-specimen scale. Although bands in long wavelengths are noisy, and signal-to-noise ratios are low (Fig. 6-1), Specim data provide great spectral information with fine detail. PCA, MNF transformations, as well as SAM classifications, are successful in identifying variations in ferric iron contents within an outcrop, and among hand samples. Although SWIR data are noisy and full of strips, transformations on small sections can map variations in ferric iron contents. Carbonates are not analyzed because of

the lack of high enough signal-to-noise ratios. Further processing should be performed to extract more spectral information from long wavelength spectrum, especially for SWIR images.

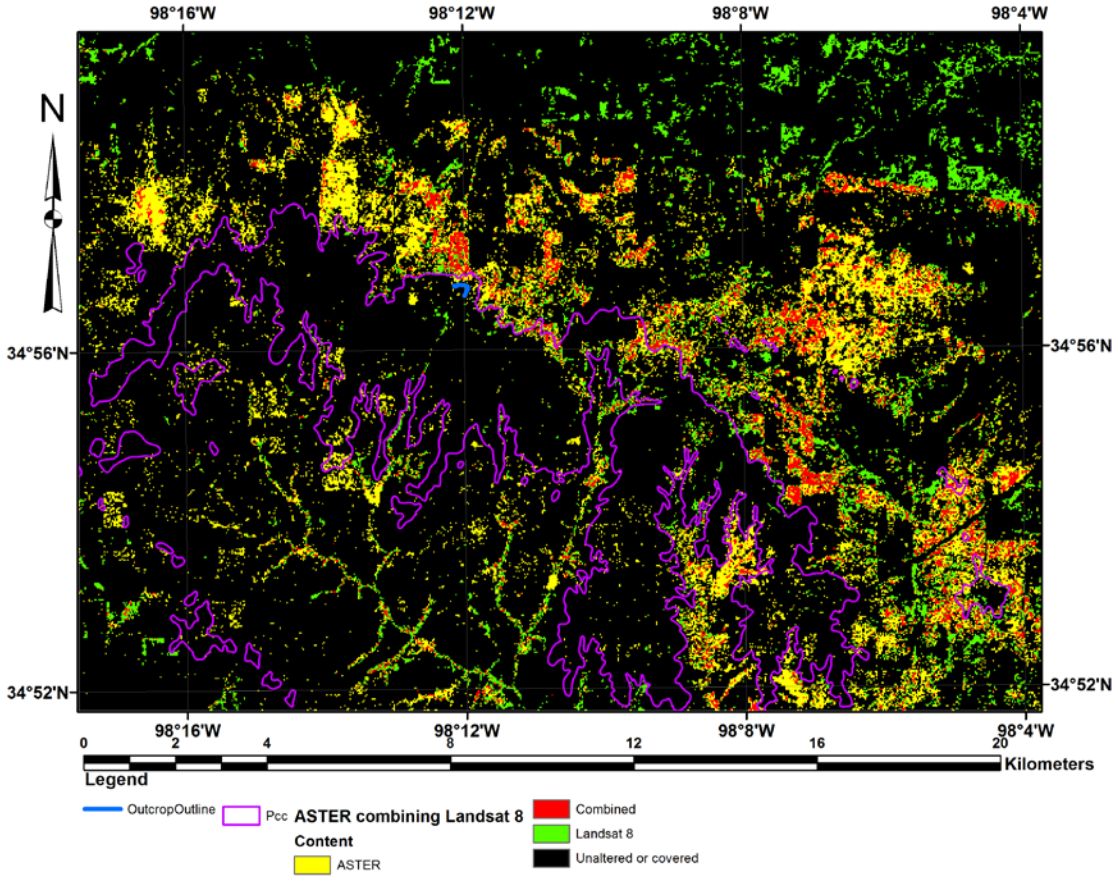

Figure 6-1, Combination of alteration sites mapped by Landsat 8 and ASTER. The black color represents area that are unaltered or covered, the yellow color represents altered area with high carbonate contents mapped by ASTER, the green color represents the altered area with low ferric iron content mapped by Landsat 8, the red color represents the altered area with high carbonate content and low ferric iron content mapped by ASTER and Landsat combined. The magenta outlines show the areal extent of the Cloud Chief Formation, the rest of the map outcrops the Rush Springs Formation. The alteration sites mapped by Landsat 8 and ASTER are mostly located in the Rush Springs Formation. The blue line shows the outline of the scanned outcrop. Note that the northeast part is not covered by the ASTER scene.

Fig. 6-2 compares the image spectra with ASD spectra and the USGS spectral library. Note the offset among spectra for clarity. The image spectra get very noisy and wavy in long wavelengths, but show great spectral information in short wavelengths. The presence of ferric iron can be identified from image spectra CF-7 and CF-Red, as well as ASD spectra sandstone-unaltered-1 and library spectra goethite.

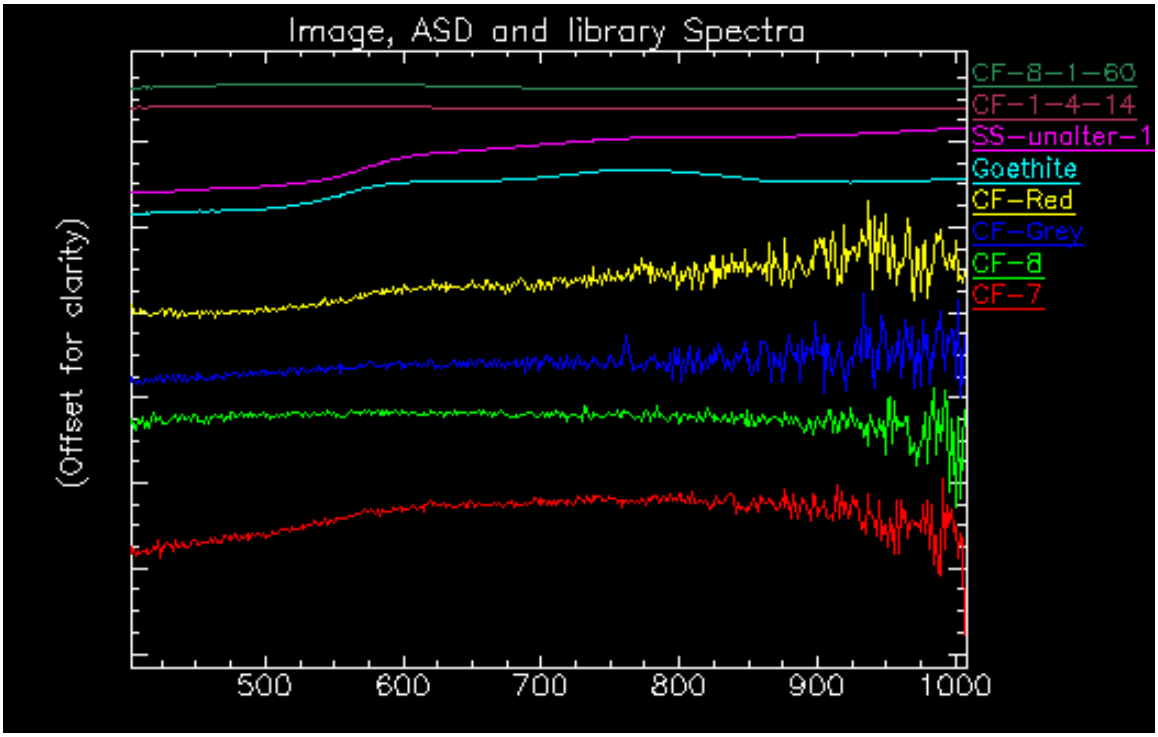

Figure 6-2, Comparison of image spectra, ASD spectra, and spectral library. These spectra have been offset for clarity. CF-7 and CF-8 are sample image spectra, CF-Grey and CF-Red are field image spectra, goethite is from spectral library, CF-1-4-14 and CF-8-1-60 are ASD spectra. Ferric iron absorption features could be identified on CF-7, CF-Red, sandstone-unaltered-1, and goethite.

6.4 Mechanism of Hydrocarbon Seepage

It is inferred that the surface alterations studied in this thesis are caused by leaking hydrocarbons from petroleum reservoirs. The reduction of ferric iron and the presence of pyrite can be both explained by the influence of hydrogen sulfide:

$$Fe_2O_3 + 2H_2S = FeS_2 + FeO + 2H_2O$$

Hydrogen sulfide can come from two sources: petroleum reservoir at depth, and surficial reduction from sulfates. Sulfate is very common in the study area, the Cloud Chief Formation lies on top of the Rush Springs Formation. It is also reported that gypsum is altered into carbonates (Donovan, 1974), the mechanism of this alteration can be:

$$C_nH_{2n+2} + CaSO_4 = CaCO_3 + H_2S + H_2O$$

This could explain the alteration of gypsum into carbonates, the origin of hydrogen sulfide, as well as the cementation of the sandstones. With the presence of some clay minerals and magnesium ion bearing formation waters in the sandstones, the resulting cementation mineral is dolomite in the alteration zone.

Isotopic studies (Fig. 6-3) show that the $\delta^{13}C$ of the carbonate cements in sandstones is lower than normal carbonates at the surface and should have an organic origin. This evidence supports the mechanism of hydrocarbon-induced rock alterations.

Abundant faulting (Fig. 6-4) and the anticlinal structure (Fig. 6-5) in the area provided perfect conduit for hydrocarbons to migrate from their reservoirs in the Pennsylvanian strata to the Permian-Pennsylvanian contact, an angular unconformity. A cross section on west Cement (Fig. 6-6) shows the normal and reverse faults, as well as the anticlinal structure. The dome structures

also provided temporary accumulation space below the unconformity. The hydrocarbons then rose across the unconformity and through the porous Permian beds, and induced alterations we see on the surface.

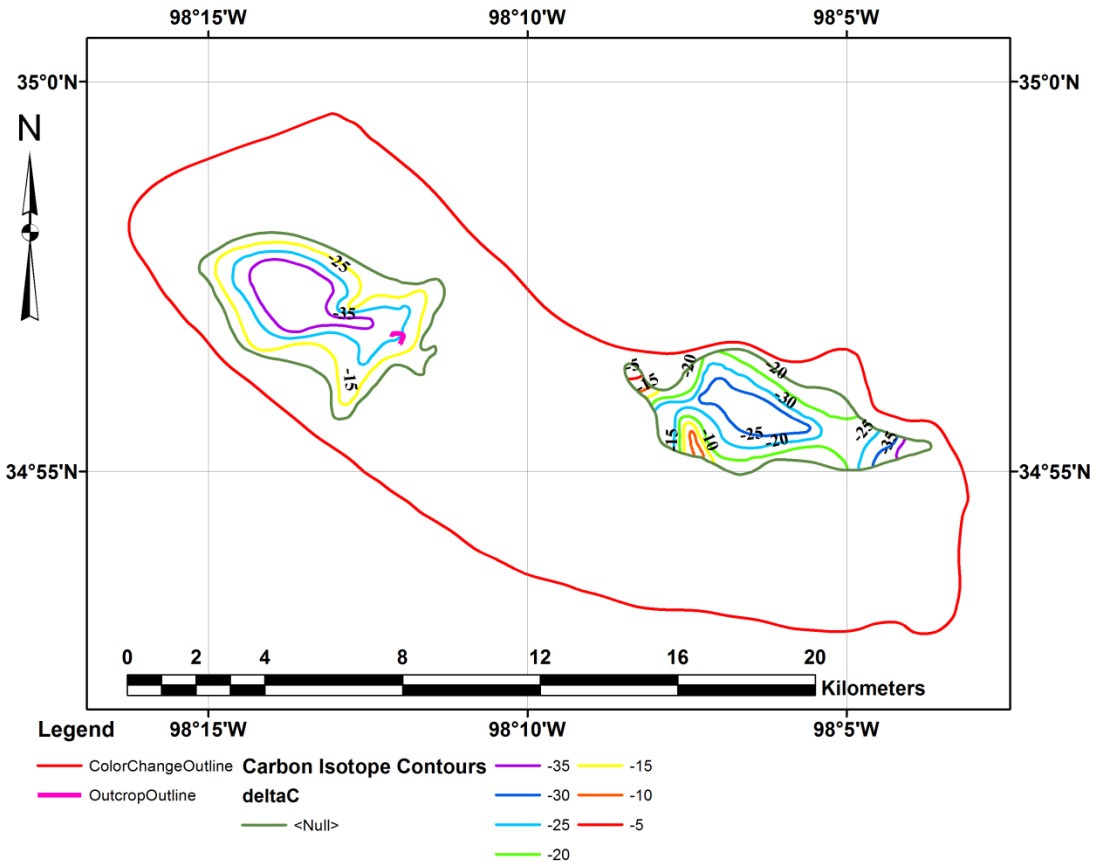

Figure 6-3, $\delta^{13}C$ contour map of the Cement field. The red line shows the color change limit, and the magenta line shows the outline of the scanned outcrop, redrawn after Donovan (1974).

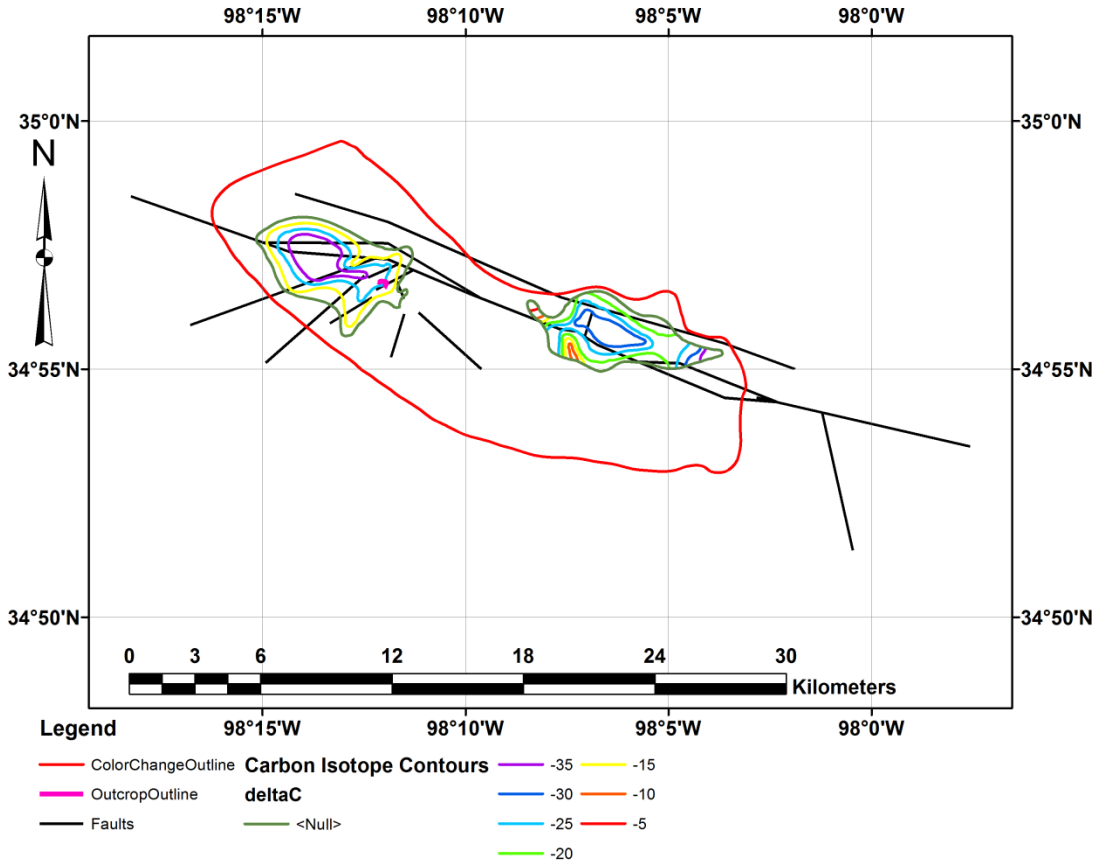

Figure 6-4, $\delta^{13}C$ contour map of the Cement field shown on top of fault traces on Hoxbar Group. The red line shows the color change limit, the magenta line shows the outline of the scanned outcrop, and the black lines shows faults mapped in the Hoxbar Group, redrawn after (Herrmann, 1961; Donovan, 1974).

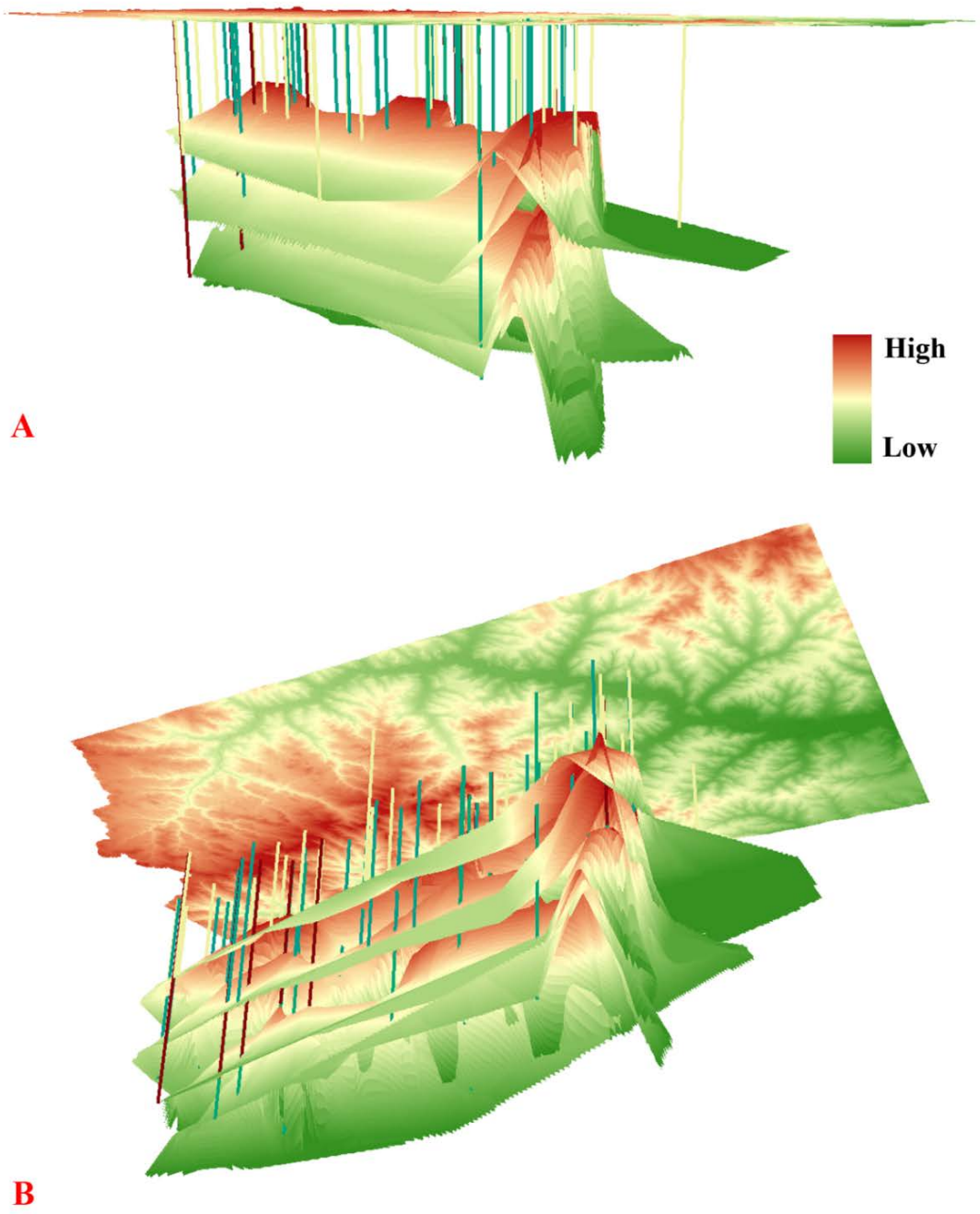

Figure 6-5, Paleo-structure maps of Hoxbar, Deese, Atoka, and Morrow Groups showing the general anticline and the dome structures where hydrocarbons could accumulate. Data from Herrmann (1961).

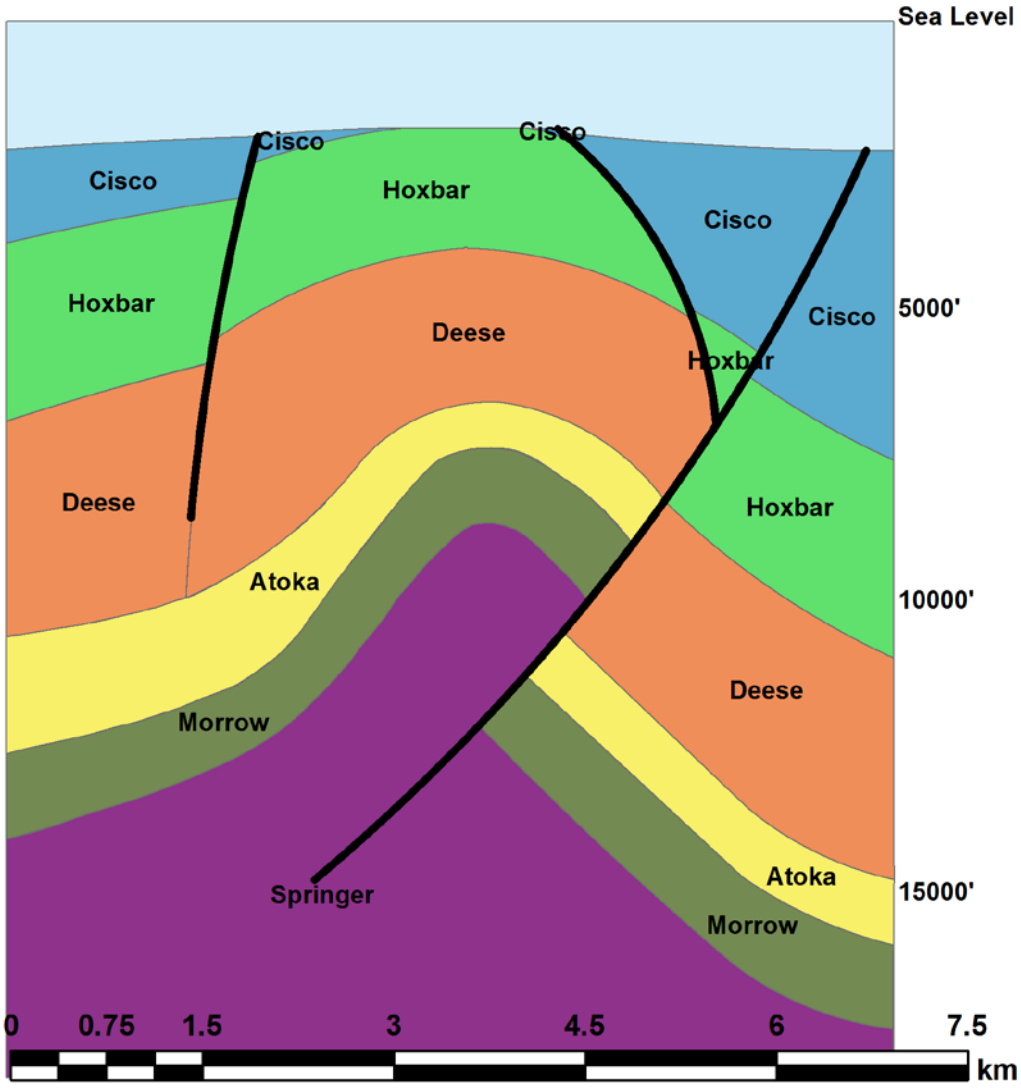

Figure 6-6, A cross section illustrating the anticlinal structure and faults in Pennsylvanian strata , west Cement field, Oklahoma. Redrawn after Herrmann (1961).

6.5 Conclusions

Petrographic analysis show that unaltered sandstones are red, with hematite/limonite coatings, not well-cemented, while altered sandstones are bleached, with rare iron oxide coatings, and very well-cemented by carbonates. Aggregation of pyrite and secondary oxidation are also identified

on rock samples. The bleaching and cementation of the Rush Springs sandstones are the major and significant alteration phenomena. Alterations in the gypsum member are embodied in a crystallization gradient.

Spectroscopy analyses show that variations in ferric iron content can be recognized by the presence or absence of ferric iron absorption features; cementation of carbonates can be recognized by absorption features in altered sandstones. On the other hand, gypsum alterations could not be identified in spectra.

Multispectral and hyperspectral remote sensing imagery mapped the alteration sites with bleaching of red beds and cementation of carbonates in Rush Springs sandstones. Band ratios, principal components analysis (PCA), minimum noise fraction (MNF), and spectral angle mapper (SAM) processing algorithms provide powerful tools in identifying these alterations.

With a mechanism of hydrocarbon seepage and surficial alterations, this study could be a paradigm of the application of remote sensing techniques, and a perspective tool in further petroleum exploration.

References

Abrams, M., Hook, S., Ramachandran, B., 2002. ASTER user handbook, version 2. Jet Propulsion Laboratory.

Abrams, M.J., Ashley, R.P., Rowan, L.C., Goetz, A.F., Kahle, A.B., 1977. Mapping of hydrothermal alteration in the Cuprite mining district, Nevada, using aircraft scanner images for the spectral region 0.46 to 2.36 μm. Geology 5, 713-718.

Allen, R.F., Thomas, R.G., 1984. The uranium potential of diagenetically altered sandstones of the Permian Rush Springs Formation, Cement District, Southwest Oklahoma. Economic Geology 79, 284-296.

Beck, R., 2003. EO-1 User Guide-Version 2.3. Satellite Systems Branch, USGS Earth Resources Observation Systems Data Center (EDC).

Berger, Z., Williams, T.L., Anderson, D., 1992. Geologic stereo mapping of geologic structures with SPOT satellite data. AAPG Bulletin 76, 101-120.

Boardman, J.W., Kruse, F., 1994. Automated spectral analysis: a geological example using AVIRIS data, north Grapevine Mountains, Nevada, Proceedings of the Thematic Conference on Geologic Remote Sensing. Environmental Research Institute of Michigan, pp. I-407.

Campbell, J.B., 2002. Introduction to remote sensing. CRC Press.

Clark, R.N., 1999. Spectroscopy of rocks and minerals, and principles of spectroscopy. Manual of remote sensing 3, 3-58.

Clark, R.N., Swayze, G.A., Wise, R., Livo, K.E., Hoefen, T.M., Kokaly, R.F., Sutley, S.J., 2007. USGS digital spectral library splib06a. US Geological Survey Reston, VA.

Crósta, A.P., De Souza Filho, C.R., Azevedo, F., Brodie, C., 2003. Targeting key alteration minerals in epithermal deposits in Patagonia, Argentina, using ASTER imagery and principal component analysis. International Journal of Remote Sensing 24, 4233-4240.

Donovan, T.J., 1974. Petroleum microseepage at Cement, Oklahoma: evidence and mechanism. AAPG Bulletin 58, 429-446.

Donovan, T.J., Forgey, R.L., Roberts, A.A., 1979a. Aeromagnetic Detection of Diagenetic Magnetite over Oil Fields. AAPG Bulletin 63, 245-248.

Donovan, T.J., Termain, P.A., Henry, M.E., 1979b. Late diagenetic indicators of buried oil and gas: II, Direct detection experiment at Cement and Garza oil fields, Oklahoma and Texas, using enhanced Landsat I and II images. US Geological Survey.

Etiope, G., Klusman, R.W., 2010. Microseepage in drylands: Flux and implications in the global atmospheric source/sink budget of methane. Global and Planetary Change 72, 265-274.

Gao, J., 2008. Digital analysis of remotely sensed imagery. McGraw-Hill Professional.

Gay, S.P., 1992. Epigenetic versus syngenetic magnetite as a cause of magnetic anomalies. Geophysics 57, 60-68.

Green, A.A., Berman, M., Switzer, P., Craig, M.D., 1988. A transformation for ordering multispectral data in terms of image quality with implications for noise removal. Geoscience and Remote Sensing, IEEE Transactions on 26, 65-74.

Hefferan, K., O'Brien, J., 2010. Earth materials. John Wiley & Sons.

Herold, M., Roberts, D.A., Gardner, M.E., Dennison, P.E., 2004. Spectrometry for urban area remote sensing—Development and analysis of a spectral library from 350 to 2400 nm. Remote Sensing of Environment 91, 304-319.

Herrmann, L.A., 1961. Structural geology of Cement-Chickasha area, Caddo and Grady Counties, Oklahoma. AAPG Bulletin 45, 1971-1993.

Hui, S., Jianyu, W., Yongqi, X., 1998. Key technology of pushbroom hyperspectral imager (PHI). Journal of Remote Sensing 2, 251-254.

Hunt, G.R., 1977. Spectral signatures of particulate minerals in the visible and near infrared. Geophysics 42, 501-513.

Irish, R., 2000. Landsat 7 science data users handbook. National Aeronautics and Space Administration, Report, 430-415.

Jones, V., Drozd, R., 1983. Predictions of oil or gas potential by near-surface geochemistry. AAPG Bulletin 67, 932-952.

Khan, S.D., Jacobson, S., 2008. Remote sensing and geochemistry for detecting hydrocarbon microseepages. Geological Society of America Bulletin 120, 96-105.

Klusman, R.W., 2011. Comparison of surface and near-surface geochemical methods for detection of gas microseepage from carbon dioxide sequestration. International Journal of Greenhouse Gas Control 5, 1369-1392.

Kruse, F.A., Lefkoff, A.B., Boardman, J.W., Heidebrecht, K.B., Shapiro, A.T., Barloon, P.J., Goetz, A.F.H., 1993. The spectral image processing system (SIPS)—interactive visualization and analysis of imaging spectrometer data. Remote Sensing of Environment 44, 145-163.

Lillesand, T.M., Kiefer, R.W., Chipman, J.W., 2004. Remote sensing and image interpretation. John Wiley & Sons Ltd.

Murphy, R.J., Schneider, S., Monteiro, S.T., 2014. Consistency of Measurements of Wavelength Position From Hyperspectral Imagery: Use of the Ferric Iron Crystal Field Absorption at 900 nm as an Indicator of Mineralogy. Geoscience and Remote Sensing, IEEE Transactions on 52, 2843-2857.

Ninomiya, Y., 2003. A stabilized vegetation index and several mineralogic indices defined for ASTER VNIR and SWIR data, Geoscience and Remote Sensing Symposium, 2003. IGARSS'03. Proceedings. 2003 IEEE International. IEEE, pp. 1552-1554.

Northcutt, R., Campbell, J., 1995. Geologic provinces of Oklahoma. AAPG Bulletin 79.

Peddle, D.R., Peter White, H., Soffer, R.J., Miller, J.R., LeDrew, E.F., 2001. Reflectance processing of remote sensing spectroradiometer data. Computers & Geosciences 27, 203-213.

Petrovic, A., Khan, S.D., Chafetz, H.S., 2008. Remote detection and geochemical studies for finding hydrocarbon-induced alterations in Lisbon Valley, Utah. Marine and Petroleum Geology 25, 696-705.

Petrovic, A., Khan, S.D., Thurmond, A.K., 2012. Integrated hyperspectral remote sensing, geochemical and isotopic studies for understanding hydrocarbon-induced rock alterations. Marine and Petroleum Geology 35, 292-308.

Philp, R., Crisp, P., 1982. Surface geochemical methods used for oil and gas prospecting—a review. Journal of Geochemical Exploration 17, 1-34.

Price, L.C., 1986. A critical overview and proposed working model of surface geochemical exploration, Unconventional methods in exploration for petroleum and natural gas, Symposium IV. Southern Methodist University Press, Dallas, pp. 245-304.

Reeves, F., 1921. Geology of the Cement oil field, Caddo County, Oklahoma: Chapter B in Contributions to economic geology, 1921, Part II.--Mineral fuels. US Government Printing Office.

Reynolds, R., Fishman, N.S., Hudson, M.R., 1991. Sources of aeromagnetic anomalies over Cement oil field (Oklahoma), Simpson oil field (Alaska), and the Wyoming-Idaho-Utah thrust belt. Geophysics 56, 606-617.

Reynolds, R.L., Fishman, N.S., Wanty, R.B., Goldhaber, M.B., 1990. Iron sulfide minerals at Cement oil field, Oklahoma: Implications for magnetic detection of oil fields. Geological Society of America Bulletin 102, 368-380.

Richards, J.A., 1999. Remote sensing digital image analysis, 3. Springer.

Roy, D.P., Wulder, M.A., Loveland, T.R., C.E, W., Allen, R.G., Anderson, M.C., Helder, D., Irons, J.R., Johnson, D.M., Kennedy, R., Scambos, T.A., Schaaf, C.B., Schott, J.R., Sheng, Y., Vermote, E.F., Belward, A.S., Bindschadler, R., Cohen, W.B., Gao, F., Hipple, J.D., Hostert, P., Huntington, J., Justice, C.O., Kilic, A., Kovalskyy, V., Lee, Z.P., Lymburner, L., Masek, J.G., McCorkel, J., Shuai, Y., Trezza, R., Vogelmann, J., Wynne, R.H., Zhu, Z., 2014. Landsat-8: Science and product vision for terrestrial global change research. Remote Sensing of Environment 145, 154-172.

Saunders, D.F., Burson, K.R., Thompson, C.K., 1999. Model for hydrocarbon microseepage and related near-surface alterations. AAPG bulletin 83, 170-185.

Schumacher, D., 1996. Hydrocarbon-induced alteration of soils and sediments.

Simon, K., 2006. Hyperion Level 1G(L1GST) Product Output Files Data Format Control Book (DFCB). Department of the Interior, US Geological Survey.

Stanley, T., Miller, G., 2005. Geologic Map of the Lawton 30′ × 60′ Quadrangle. Caddo, Comanche, Grady, Kiowa, Stephens and Tillman Counties, Oklahoma (1: 100,000): Oklahoma Geological Survey.

Sultan, M., Arvidson, R.E., Sturchio, N.C., Guinness, E.A., 1987. Lithologic mapping in arid regions with Landsat thematic mapper data: Meatiq dome, Egypt. Geological Society of America Bulletin 99, 748-762.

Van der Meer, F., Van Dijk, P., Van Der Werff, H., Yang, H., 2002. Remote sensing and petroleum seepage: a review and case study. Terra Nova 14, 1-17.

Vermillion, S.C., Sader, S.A., 1999. Use of the Minimum Noise Fraction (MNF) Transform to Analyze Airborne Visible/Infrared Imaging Spectrometer (AVIRIS) Data of Northern Forest Types, JPL Workshop, JPL Publication.

Vermote, E.F., El Saleous, N.Z., Justice, C.O., 2002. Atmospheric correction of MODIS data in the visible to middle infrared: first results. Remote Sensing of Environment 83, 97-111.

Yang, Zhang, Van Der, M., Kroonenberg, 1998. Geochemistry and field spectrometry for detecting hydrocarbon microseepage. Terra Nova 10, 231-235.

ASTER Instrument Characteristics (http://asterweb.jpl.nasa.gov/characteristics.asp). Accessed on May 2014.

Datasheet for Spectral Camera HS (http://www.specim.fi/files/pdf/core/datasheets/HS_Spectral_Camera-v3-11.pdf). Accessed on May 2014.

Datasheet for Spectral Camera SWIR (http://www.specim.fi/files/pdf/core/datasheets/SWIR_SpeCam_ver1-14.pdf). Accessed on May 2014.

EOS and Terra (http://asterweb.jpl.nasa.gov/eos.asp). Accessed on May 2014.

Frequently Asked Questions about the Landsat Missions (http://landsat.usgs.gov/band_designations_landsat_satellites.php). Accessed on May 2014.

How to Calculate Reflectance and Temperature Using ASTER Data (http://www.gis.slu.edu/RS/ASTER_Reflectance_Temperature_Calculation.php). Accessed on May 2014.

Landsat 8 (LDCM) History (http://landsat.usgs.gov/about_ldcm.php). Accessed on May 2014.

Using the USGS Landsat 8 Product (http://landsat.usgs.gov/Landsat8_Using_Product.php). Accessed on May 2014.